UC Irvine
UC Irvine Electronic Theses and Dissertations

Title
Developing Practical Nanofabrication Techniques for Plasmonic Structures

Permalink
https://escholarship.org/uc/item/5c77k5qn

Author
Sharac, Nicholas

Publication Date
2015

Peer reviewed|Thesis/dissertation

eScholarship.org Powered by the California Digital Library
University of California

UNIVERSITY OF CALIFORNIA,
IRVINE

Developing practical Nanofabrication Techniques for Plasmonic Structures

DISSERTATION

submitted in partial satisfaction of the requirements
for the degree of

DOCTOR OF PHILOSOPHY

in Chemistry and Material Physics

by

Nicholas Warren Sharac

Dissertation Committee:
Associate Professor Regina Ragan, Chair
Chancellor's Professor Reginald Penner
Professor John Hemminger

2015

© 2015 Nicholas Warren Sharac

TABLE OF CONTENTS

	Page
LIST OF FIGURES	iv
LIST OF TABLES	v
ACKNOWLEDGMENTS	vi
CURRICULUM VITAE	vii
ABSTRACT OF THE DISSERTATION	viii
CHAPTER 1- General Introduction	1
1.1 Confining light beyond conventional light scales	2
1.2 Surface plasmon polaritons and localized surface resonance	5
1.3 Localized surface plasmon resonance for sensing	10
1.4 Surface enhanced Raman spectroscopy	10
1.5 Metamaterials	12
1.6 Nanofabrication	14
1.7 Thesis organization	16
CHAPTER 2-Exploration of cluster assemblies	17
2.2 Cluster assemblies using chemical templating	19
2.3 Plasmonic hot spots in nanoparticle dimers	20
2.4 Fabrication	23
2.4.1 Analysis	27
2.5 SERS	31
2.5.1 Calculations	36

2.5.2 Exploring the gap 38

2.5.3 Norepinephrine concentration studies 40

2.6 Summary 41

CHAPTER 3- Scalable arrays 41

3.1 Scalable structures using a polyolefin film 43

3.2 nanosphere lithography 44

3.3 tunable nanopillars 45

3.3.1 Experimental 47

3.3.2 Results 48

3.3.3 Conclusion 53

3.3.4 SiC nanopillars 54

3.3.5 Experimental 56

3.3.6 Results 57

3.3.7 Conclusion 58

3.4 Bow Tie Arrays 60

3.4.1 Experimental 63

3.4.2 Results 65

3.4.3 Conclusion 66

3.5 Advanced structures using polyolefin film 69

3.5.1 Metamaterial structure 81

3.5.2 Experimental 81

3.5.3 Results 84

3.6 Summary 84

CHAPTER 4- Future Experiments 85

4.1 Point of care diagnostics 86

4.2 Tuning the gap 88

4.3 Integrating waveguides to excite nanocluster assembly 91

4.4 Controllable Bow Tie Arrays for SERS 92

4.5 Reduction of wrinkling of substrate for higher surface reduction 92

4.6 Combining EBL with the polyolefin film 93

REFERENCES 95

LIST OF FIGURES

Page

Figure 1.1 Computer Generated Image of an Airy Disk 2
Figure 1.2 Dispersion Curve for Light and SPP 4
Figure 1.3 Dispersion Curve for an Au Wire with and Without Loss 6
Figure 1.4 Depiction of Bulk, Surface, and Localized Plasmons 8
Figure 1.5 Refraction index comparison for conventional and metamaterials 13
Figure 2.1 Depiction of a nanoparticle dimer on PS-b-PMMA thin film 19
Figure 2.2 Plasmon Hybridization Model 21
Figure 2.3 Calculated Electric Field Enhancements for different cluster types 23
Figure 2.4 Schematic of Nanocluster Chemical Attachment 24
Figure 2.5 Schematic of Nanocluster Assembly Process 27
Figure 2.6 SEM Images of Cluster Assemblies with and Without Heat 28
Figure 2.7 SEM Comparisons between EPD, Diffusion, and Lam and B40 templates 30
Figure 2.8 SERS Spectra of BZT 32
Figure 2.9 SERS EF Comparisons at 633 nm Excitation 35
Figure 2.10 SERS EF Comparisons at 785 nm Excitation 35
Figure 2.11 Simulation of Plasmon Resonance for Dimer Geomtry 36
Figure 2.12 TEM Images of Dimers from EPD and Diffusion 38
Figure 2.13 SERS Intensity VS Laser Power 39
Figure 2.14 Concentration Studies for Norepinephrine 41
Figure 3.1 Attainable Nanostructures Using Nanosphere Lithography 44
Figure 3.2 Fabrication Schematic for Tunable Nanopillars 45
Figure 3.3 SEM Images of Pillar Arrays Etched at Different Times 48
Figure 3.4 AFM Images of Pillar Arrays at Different Etch Times and Heat Exposures 49
Figure 3.5 Spacing, width, and heights for PS bead arrays as a function of etch time and shrink temperatures 53
Figure3.6 Micro Raman and FTIR Reflection Spectra of 300 um 6H−SiC substrate and real and imaginary permittivity of substrate 55

Figure 3.7 FTIR Reflectance Spectra of 6H-SiC nanopillar arrays 58
Figure 3.8 Calculated electromagnetic intensity profiles, log (I/I0), for transverse dipolar and monopolar modes. 60
Figure 3.9 FTIR reflection spectra of 800 nm tall, 6H−SiC nanopillars as a function of pillar diameter 62
Figure 3.10 Micro-Raman and FTIR reflection spectra from a periodic array of 6H−SiC nanopillars 63
Figure 3.11 Electric field enhancement calculations for a single silver bowtie 65
Figure 3.12 Schematic of nanotriangle fabrication 66
Figure 3.13 SEM Images of Bow Tie Arrays on PO Film at different Temperatures 69
Figure 3.14 Large View SEM Image of 77% Shrunk Bow Tie Array 72

Figure 3.15 Reflectance Spectra of Bow Tie Arrays, Calculated and Experimental 74
Figure 3.16 SERS Spectra of Different Reduced Arrays 77
Figure 3.17 Calculated Fields of CNC Structure 83
Figure 3.18 SEM of Au CNC on Top of PO Film 85
Figure 4.1 EELS Spectra of Nanoparticle Dimer for Different Gaps 90
Figure 4.2 Nanocluster Assembly on Silicon Nitride Waveguides 91
Figure 4.3 Gold Bow Tie Arrays made from 250 nm PS Spheres 93

LIST OF TABLES

Page

Table 2.1 Number of Particles in Cluster Type Per micron for Heat and no Heat 29

Table 3.1 Gap spacing, height, and width dimensions of PS bead arrays for different etch times and shrink temperatures 52
Table 3.2 Triangle length, area, tip to tip spacing, and macroscopic area reduction are given for four different processing temperatures 71
Table 3.3 EF Comparisons for Different Arrays 80
Table 4.1 Cost Analysis for Nanocluster Assembly 87

ACKNOWLEDGMENTS

I would like to thank my chair and Principal Investigator, Professor Regina Ragan, for her continual support and advice; my committee members, Professor Reginald Penner and Professor John Hemminger for their patience; Professor Michelle Khine and Dr. Himanshu Sharma for their collaborative efforts regarding the thermoplastic based work mentioned in this manuscript; the National Science Foundation CHE-0748912 and CMMI-1101074 for funding; Dr. Joshua Caldwell at the Naval Research Laboratory for allowing me to partake in the Silicon Carbide work for my summer internship and for funding and Dr. Jeff Owrutsky for use of their reflectance spectrophotometer; Dr. Kumar Wrickmansinghe and Dr. Ananth Tamma for access to their lab; a special thanks to Dr. Dima Fishman for his help and donation of parts for building a Raman setup; Dr. Filippo Capolino, Dr. Salvatore Campione, and Mehdi Veysi for their computational contributions; Sarah Adams for her mentoring and for initiating the cluster assembly work. Lastly, I must thank the one person who endured almost all of my graduate hardships with me, in addition to hers, my love, Mona Merling-without her, I most certainly would never have finished.

I also thank the Royal Society of Chemistry, The American Chemical Society, Nature publishing Group, and SPIE for Permission to include copyrighted figures as part of my thesis dissertation.

CURRICULUM VITAE

Nicholas Warren Sharac

2009	B.A. in Chemistry, Bard College
2008	Teaching Assistant, Chemistry, Bard College
2009 -2010	Teaching Assistant, Chemistry, University of California, Irvine
2010-2015	Research Assistant, Nanolitography for photonic applications, University of California, Irvine
2012	Summer Intern at Naval Research Lab
2013	Summer Intern at Naval Research Lab
2013	Teaching Assistant, Chemistry, University of California, Irvine
2014	Teaching Assistant, Chemistry, University of California, Irvine
2014	M.A. in Chemical and Material Physics, University of California, Irvine
2015	Ph.D. in Chemical and Material Physics, University of California, Irvine

ABSTRACT OF THE DISSERTATION

Belief Revision and Machine Discovery

By

Nicholas Warren Sharac

Doctor of Philosophy in Chemistry and Material Physics

University of California, Irvine, 2015

Professor Regina Ragan, Chair

Periodic metal nanoparticle arrays possess electromagnetic properties useful for metamaterials, light trapping, and molecular sensing, such as surface enhanced Raman spectroscopy (SERS). The localized surface plasmon resonance (LSPR) of these arrays depends on the material, periodicity, size, and spacing of nanoparticles, all features typically best controlled by traditional top down nanofabrication techniques, such as electron beam lithography. However, such fabrication methods are not realizable commercially. Bottom-up methods are increasingly being explored for alternative nanofabrication techniques in order to achieve high throughput and inexpensive fabrication. I present here multiple unique techniques for facile, inexpensive fabrication of nanostructures for biosensing. In the first technique, I fabricate 20 nm Au nanoparticle nanocluster assemblies onto a chemically functionalized diblock copolymer film, through electrophoresis and convective assembly, attaining interparticle spacings of < 1 nm. Norepinephrine is detected at 200 parts per billion using SERS, due to the high enhancement fields of the cluster. This is a cheap, high through put, and commercially accessible process. The second technique uses thermally responsive, pre stressed polyolefin (PO) film to reduce bow tie arrays by 50% in triangle area and up to 77% in tip to tip spacing, by heating in a convection oven. Reduction of the arrays shows tunability (100 nm

blue shift) of the plasmon resonance, as well as potential for facile generation of hot spots for SERS. I also present work on tunable nanopillars using the polyolefin film, and on SiC nanopillar arrays, for the excitation of localized surface phonon polariton modes (SPhP), as potential low loss alternatives to plasmonics. FTIR reflectance spectroscopy measurements show the nanopillar arrays to confine infrared light with the emergence of localized SPhP modes, which exhibit dependence on pillar diameter and inter pillar spacing. Extreme light confinements and low losses are attained, with Q factors higher than the best plasmonic systems. Finally, I present work using electron beam lithography in tandem with the polyolefin film to achieve advanced plasmonic structures.

1. General introduction

Light has always been an essential tool for understanding the physical world. Human vision depends entirely on light, which refracts as it enters the lens of the eyes to create images, a concept that has been applied in various forms in microscopy and spectroscopy, with uses ranging from probing stars to understanding the intricacies of a cell. Light is also used as a means of communication, from optoelectronic microchips to transmission lines, and is harvested in solar cells for energy [1-3].

Manipulating light is an integral part of modern research, with a large focus being on light confinement to smaller and smaller scales. Increased computational power and telecommunication bandwidth can both be achieved using photonic circuitry and optical fibers. As with traditional electronic components, scaling down optical components can produce more power per area [4-6]. Solar cell components stand from this same line of reasoning. Higher light concentration will enable higher light capturing efficiency, allowing not only for more energy, but also for a reduction in material costs. As size is reduced, efficiency is increased, and costs go down. This same general rule applies to biological sensing, another popular field of study, which encompasses a wide range of diagnostic techniques, from metal enhanced fluorescence (MEF) to surface enhanced Raman spectroscopy (SERS) to localized surface plasmon resonance (LSPR)[7-9]. In all cases, light is used to identify biological molecules using either specific bonding sites or “fingerprint” regions which are unique to each molecule, allowing for a vast array of different components to be differentiated from each other, and to be detected even at the trace level [10]. Stronger signals from stronger light concentration mean better detection limits and accuracy of the sensor. Smaller and or

more compact sensors mean better cost efficiency, general availability and potential for point of care diagnostics,

Light matter interaction is also an intense area of research on a fundamental level. Starting at the nanoscale, defined as 100 nm or less[11], the behavior of single molecules and even atoms, as well quantum behavior of electrons, can begin to be studied[12,13]. Metamaterials, primarily the study of negative refractive index materials, have shown potential a wide range of fascinating properties, from cloaking to superlensing [14]. Much of the current experimental data have been for large structures interacting in the microwave and radio wave range. Smaller structures, particularly in the nanoscale, which includes plasmonic metamaterials, will allow for metamaterial phenomena to be explored in the near IR and visible light range [15].

1.1 Confining light beyond conventional light scales

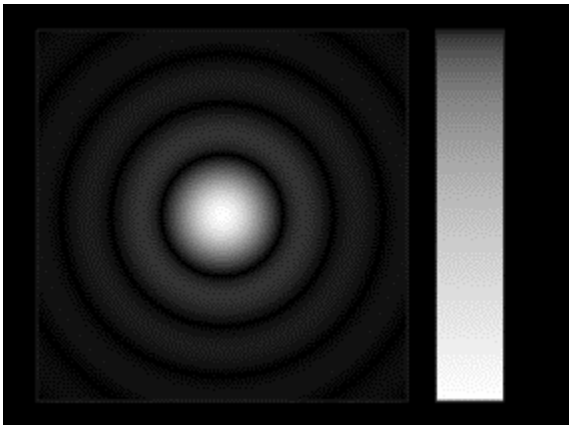

Figure 1.1. Airy disk (computer generated image).

Even the best optical imaging systems are limited by a fundamental diffraction limit, caused by the diffracted light on the edges of the numerical aperture stop, which results in an airy disk instead of a fine point, as shown in figure 1.1. For the case of imaging subwavelength structures, the abbe diffraction limit can be defined as

$$d = \frac{\lambda}{2\mathrm{n}\sin\theta}$$

The spot radius, d, becomes smaller with smaller wavelengths, λ, and larger numerical aperture, NA, where NA= n sinθ, where n is the refractive index of the medium and θ the angle with which the light converges to. Even using lower wavelength light, for example 500 nm, still gives a diffraction limit of approximately 250 nm. Since the numerical aperture is a fixed parameter, the only tunable parameter to achieve higher resolution is through λ, and to be able to image the electronic/vibrational properties of the sample, the frequency of the light must not be changed. Since,

$$\lambda = (2\,\pi\,c)/\omega$$

Changing c, the speed of light, can change the wavelength while not altering the frequency. Classically this has been achieved by using immersion oil for microscopes, but this only improves resolution to the extent of increasing the refractive index. Evanescent waves are near field waves which travel along the surface of the metal and decay exponentially away from the surface. These waves, which are a slow form of light, can couple with the collective electron oscillation of a metal surface, to excite what is known as the surface plasmon polariton (SPP) [16]. Figure 1.2 shows the

dispersion curve for SPP and light [17]. Whereas the wavenumber, k (momentum) shows a linearly relationship the frequency (energy) of light, the wavenumber of the SPP gently curves away as the frequency approaches the plasmon frequency, resulting in a slower, short wavelength. While normal light and SPP will never cross, this is not the case for evanescent light, which travels along the metal of the SPP, and therefore can excite the SPP at a specific frequency, allowing resonant excitation of the SPP. Smolyaninov et al demonstrated this principle by exciting a periodic nanohole array on a gold film in a glycerin droplet [18]. By exciting the surface with a 502 nm argon ion laser, they were able to produce SPPs of ~ 70 nm, resulting in resolution enhancement of ~7. This is depicted in the figure. In effect, they had created a 2D plasmonic microscope. Near field light can be detected in the far field by various methods such as periodic corrugation [19], resulting ultimately in bypassing the classical diffraction limit.

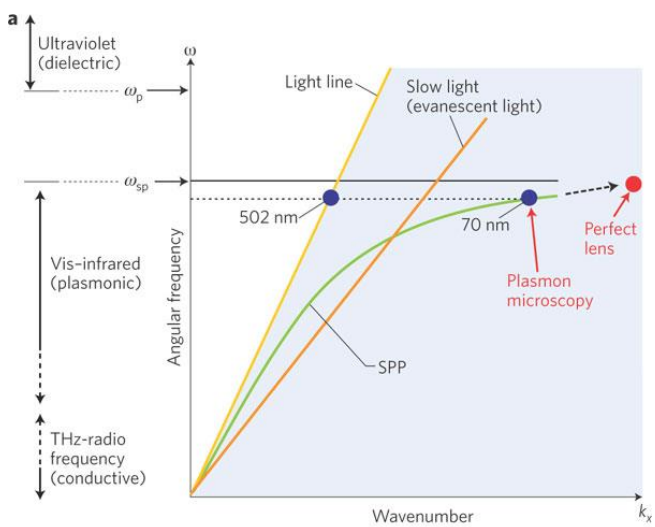

Figure 1.2. Dispersion curves for light and SPP. For an excitation of of 502 nm on a gold surface, the SPP has a wavelength of ~ 70 nm. Reprinted by permission from Macmillan Publishers Ltd: [Nature Photonics] (17), copyright (2009)

1.2 Surface plasmon Polaritons and Localized surf plasmon resonance

Surface plasmon polaritons are eignmodes for a metal dielectric interface, as they are solutions to Maxwell's equations and do not require the presence of an incident field. They are transverse magnetic (TM or E mode) planewaves that propagate along the interface of a dielectric and metal. The dispersion relation relates the wave vector of an SPP, k_x to the frequency, ω, by

$$k_x = k_0\sqrt{\frac{\varepsilon 1 \varepsilon 2}{\varepsilon 1 + \varepsilon 2}}$$

Where ε1,ε2 are the permittivities of the metal and dielectric, respectively, and $k_0=\omega/c$ is the wave vector in free space. If we neglect loss, then the function for the permittivity of a metal, ε1, using the Drude model for a free electron gas, is

$$\varepsilon 1 = 1 - \frac{\omega_p^2}{\omega}$$

Where ω_p is the bulk plasma frequency. Looking at the dispersion relation again, in figure 2, we see that for small k, the SPP behaves like a photon. Once k_x becomes larger than k_0, the SPP wave vector begins to curve to the right of the light line, resulting in a shorter wavelength and light confinement as described previously, and eventually reaches an asymptotic limit, as shown figure 2, known as the surface plasma frequency, which describes the frequency at which the surface electrons oscillate. From the dispersion curve, surface plasma frequency is related to the bulk plasma frequency by

$$\omega_{sp} = \frac{\omega_p}{\sqrt{1+\varepsilon 2}}$$

Physically speaking, light below the plasma frequency is reflected, as the electrons in the metal screen the electric field. Above the frequency, the electrons are no longer fast enough to screen the photon, and the frequency is transmitted. Below the plasma frequency, for k_x to exceed k_0, and thus for the SPP to lie to the right of light line, ε1, the permittivity of the metal, must be negative, or specifically,

$$\varepsilon 1 < -\varepsilon 2$$

This condition is satisfied by metals at short wavelengths, however. At higher frequencies, incident light passing through the metal will experience damping due to ohmic losses and also electron-core interactions. The damping can be accounted for by

$$K_x = k_x' + ik_x''$$

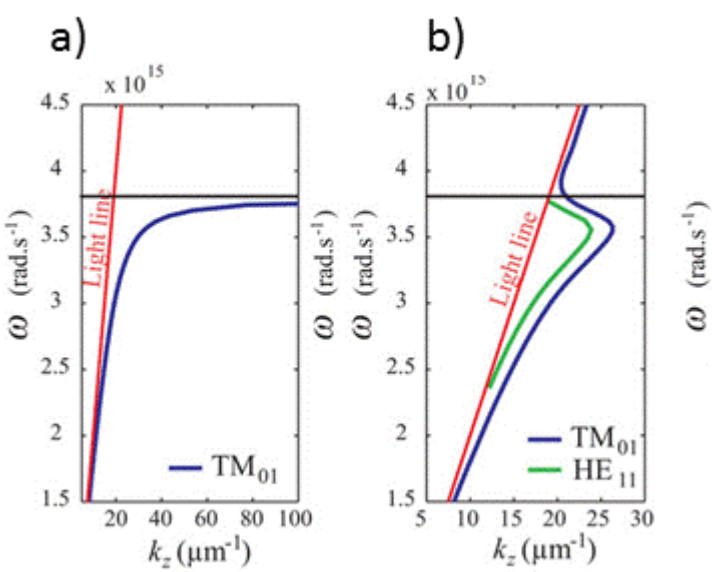

Figure 1.3. Dispersion curve for a gold wire of 100 nm radius in absence (a) and presence(b) of losses. Permission from Nature Publishing Group. Link to permission here https://s100.copyright.com/AppDispatchServlet#formTop [20] Scientific Reports. 2013.

Figure 1.3 a) [20] shows the dispersion relation for a 100 nm thick gold nanowire. Adding an imaginary component to the wave vector, to describe the extent of the loss along the direction of propagation, results in rapid increase in loss as the surface plasmon frequency is reached. This is depicted as an s shaped curve in figure 1.3 b). Ideal candidates for metals then have low absorption in the visible and near IR, resulting in less damping, but high negative permittivities, resulting in more pronounced SPPs. Au and Au are the best candidates, although since Ag is more prone to oxidation, Au is often more practical.

As observed in figure 1.2 and figure 1.3, incident frequency cannot directly couple with the SPP frequency. Figure 1.2 b) shows the Kretschmann-Raether configuration. A prism is used to phase match the incident light with the SPP, as the wave vector in a prism is larger than in air [21]. The phase matched light is tunneled through a thin metal gold film to the SPP. Wave vector matching is not required for metals that are much smaller than the incident wavelength, where the electron oscillations are then in phase with incident light, allowing direct coupling. Fig 1.4 [22] shows a comparison between bulk plasmons, surface plasmon polaritons, and localized surface plasmons, the latter being the prime focus of this thesis.

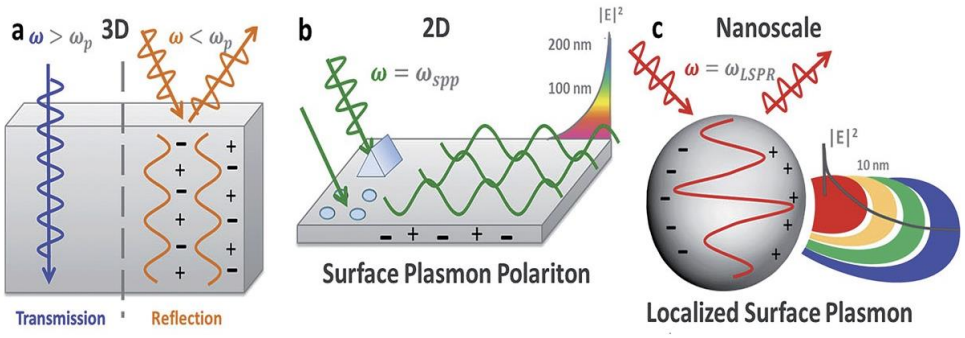

Figure 1.4. Depiction of bulk plasmon a), surface plasmon polariton b) and localized surface plasmon polariton c). Reproduced from [Ref 22] with permission of The Royal Society of Chemistry. http://dx.doi.org/10.1039/C4AN01079E

As shown in fig 1.4 C, in the case of a nanoparticle with diameter d, where (d<<λ), the incident field will be constant, resulting in a uniform displacement of electron density and a restoring force from the positive ionic core. This leads to an oscillation frequency similar to a simple harmonic oscillator, which can be excited directly by the incident field due to the additional momentum provided by the nanoparticle geometry itself. The extinction cross section, which encompasses both scattering and absorption, can be expressed, using Mie theory [23], as

$$\sigma_{ext} = 9\frac{\omega}{c}\varepsilon_{diel}^{3/2}V\frac{\varepsilon''_{metal}}{(\varepsilon'_{metal} + 2\varepsilon_{diel})^2 + \varepsilon''_{metal}{}^2}$$

For negative values of the real part of the dielectric function, the denominator will become small, resulting in a strong extinction cross section. The resonance condition for localized surface plasmon resonance, or LSPR, is known as

$$\omega_{lspr} = \frac{\omega_p}{\sqrt{1 + 2\varepsilon_{diel}}}$$

where, LSPR is largely dependent on the dielectric environment [24, 25]. Due to the coherence of the electron oscillations, the volume, V, of the extinction cross section is orders of magnitude larger than the size of the nanoparticle with radius, r, where $V=4/3\ \pi\ r^3$. In comparison to SPR, LSPR has an intense local EM field due to the confinement of the electron oscillations, where the field can be several orders of magnitude larger than the incident field. LSPR is sensitive to particle shape and dielectric environment [26]. Sharp edges further confine the electric field, in what is known as the "lightning rod" effect, leading to further enhancements [27-30].Larger nanoparticles experience a red shift, as the repulsive forces of the electrons gets weaker due to increased size of the nanoparticle[31,32]. Nanoparticles with diameters below 15 nm have strong electron-electron scattering, resulting in rapid conversion to heat, and therefore much of the incident energy is absorbed. In particles with diameters larger than 15 nm, and therefore less electron-electron scattering, the LSPR energy will be reradiated, leading to enhanced scattering. In either case, LSPR has short lifetimes (and therefore broader peaks than SPR) due to the electron-electron scattering and reradiative damping. As shown in figure 1.4 h) and j), the extinction cross section is greatly enhanced at a specific frequency, ω_{LSPR} where the extent of scattering/absorption depends primarily on the nanoparticle size. Of significant note is the ability for LSPR-LSPR coupling, which will be much of the subject in chapter 2.

1.3 LSPR as sensors

LSPR has been utilized in at least three broad types of sensors-plasmonic sensors, metal enhanced fluorescence (MEF), and surface enhanced Raman spectroscopy (SERS). Plasmonic sensors operate by shifting the spectral properties either of LSPR or SPR once the analyte binds to the metal of the surface or nanoparticle. This is due to the sensitivity of the LSPR and SPR to changes of the dielectric environment. Plasmonic sensors can be achieved on a chip using a patterned metal film or in a colloidal solution of metal nanoparticles [33, 34]. In the latter case, attached analytes bring nanoparticles into proximity, which results in coupled EM fields and change of solution color. Colorimetry has proved an effective method to measure this change and allows for direct measurement of analyte concentration, although currently the sensitivity is still low compared to other techniques like MEF and SERS. In metal enhanced fluorescence, a plasmon within 1-10 nm of a fluorophore can have energy transfer due primarily to dipole-dipole interactions. Both distance and spectral overlap between the fluorophore and plasmon affect whether the excitation or emission is enhanced in the fluorophore. Overlap with fluorophore absorption results in enhanced excitation, whereas overlap with fluorophore emission results in enhanced emission. When designing plasmonic structures for MEF, spectral overlap, gap between plasmon and fluorophore, and the EM enhancement of the plasmonic structure are all factors that must be considered. The highest attainable EF reported thus far has been 1340[35], with reports of limit detection limits being four times as high as when using plasmonic sensors. MEF has been used to image bacteria and tissues, but is limited in some cases due to its requiring of a labeling agent.

1.4 Surface Enhanced Raman Spectroscopy

Surface enhanced Raman spectroscopy has increasingly gained attention as a rising biosensor due to several key advantages in comparison to other alternatives, listed below.

1. Ease of use: Unlike fluorescence, SERS does not require a labeling marker, nor any other type of sample preparation. SERS, fundamentally, is uncomplicated, as it does not involve the matching of both absorption and emission, as in fluorescence, and Raman spectroscopy is easy to operate. No purging of gases is necessary, as in IR spectroscopy.
2. Powerful diagnostic capability: Raman spectroscopy, like IR spectroscopy, measures the vibrational and rotational modes of a molecule, and therefore is able to differentiate even similar analytes due to their unique spectral signatures. Unlike IR spectroscopy, or surface enhanced IR (SERIA), SERS is largely unaffected by water, giving it a prime advantage. SERS also is able to differentiate multiple molecules at once, due to its high sensitivity and ability to differentiate unique spectral signatures. SERS has been used to detect a wide range of analytes, from graphene, to DNA, to dangerous biomolecules, and therefore touches multiple industries.[36-39]
3. Point of care diagnostics: Commercially available portable Raman spectroscopes are now in existence, including even palm sized Raman readers. Combined with its ease of use and the low requirements to achieve SERS (e.g., no fluorescence marker is required) SERS being commonly used for portable sensors is becoming a very potential reality.
4. Single molecule detection: Multiple reports have shown SERS detection of a single or several molecules. This has been verified by using an isotope study, where an extremely low concentration of two different isotopes are introduced to the SERS surface, and only one isotope is detected at a time [40]. Single molecular detection is important on both a technical and fundamental level. In terms of diagnostics, it offers the most powerful sensing abilities needed, and can be used to detect even trace amounts of molecules. This is useful in a range of fields, such as forensics or medical diagnostics. For instance, a breathalyzer which can detect the onset of a dangerous disease, like cystic fibrosis, can be built around a good SERS sensor with high detection capabilities. Single

molecule detection has always been of huge academic interest, for its potential to characterize single molecular behavior.

Raman spectroscopy measures the inelastic scattering of a molecule. When the vibrational and or rotational states of a of a polarizable molecule are excited, there is an energy difference between the incoming and out coming photon, where in the Stokes shift, the energy difference of the scattered photon is negative, or lower, and in anti-Stoke shifts, the energy difference is positive, or higher. This difference, also known as Raman shift, is typically measured in wavenumbers (cm^{-1}) and can be used to fingerprint many different types of molecules. However, since inelastic scattering only occurs in every one in ten million scattered photons, the signal is generally low if not nonexistent for trace materials.

Surface enhanced Raman spectroscopy (SERS) has allowed for the detection of trace elements through both an electromagnetic (EM) enhancement and a chemical enhancement (CE). CE, which is a result of charge transfer between the adsorbed analyte and the metallic structure, typically gives enhancements between 10-100, whereas EM enhancements are anywhere between 10^4 and 10^8[41-45]. The regular enhancement of the localized field $|E_{loc}|^{2,}$ of the plasmon resonance of a nanoparticle, applies to both excitation and emission of the Raman scattering, as the difference in the frequencies is small, yielding a total field enhancement of $|E_{loc}|^4$. Since the local field can be orders of magnitude higher than the field of the incident light, making SERS detectable even in the far field.

1.5 Metamaterials

Electromagnetic metamaterials affect incident electromagnetic waves in manners not found in nature by using structures smaller than the frequency of the incident wavelength. Primarily, metamaterials refers to negative refractive index materials. In nature, virtually all materials have a positive permittivity and permeability, the exception being metals such and gold and silver, which exhibit negative permit ivies at short wavelengths. Metamaterials are unique in their ability to become negative in both permeability and permittivity, resulting in a negative refractive index, as depicted below in fig 1.5.

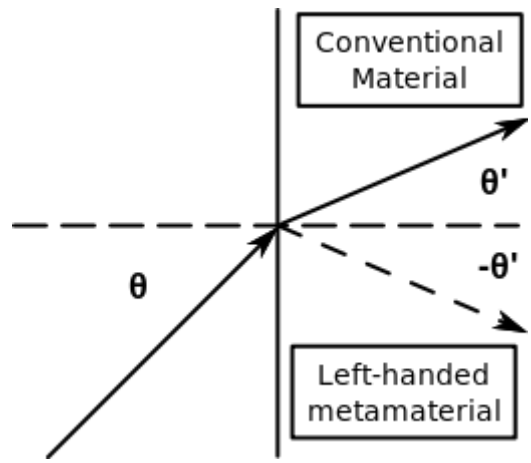

Figure 1.5. Refractive for conventional and left handed metamaterial. In the case for the metamaterial, the refractive index, n, is reversed.

We can see the requirement for a negative permeability, μ, and permittivity, ε manifested in the following equation, where

$$n = \pm\sqrt{\varepsilon u}$$

Conventionally the positive sign is taken. However, this is reversed in cases where the phase velocity is reversed. The phase velocity of light is opposite to the direction of power flow whenever the below inequality holds

$$\left[+\sqrt{\varepsilon_r'^{\,2} + \varepsilon_r''^{\,2}} - \varepsilon_r'\right]\left[+\sqrt{\varepsilon_r'^{\,2} + \varepsilon_r''^{\,2}} - u_r'\right] > \varepsilon_r'' u_r''$$

This equality becomes true whenever both the real permittivity and permeability are negative. Simultaneous negative permittivity and permeability have been experimentally attained, although often at larger scale. This is due to the often complicated structural designs, which are more difficult to produce in the nano regime [46, 47]. As a result, much of the negative refractive index

properties have been verified experimentally only in the microwave range. Photonic metamaterials, operate at visible lengths and are largely appealing for potentials in cloaking, superlensing, communications, and solar enhancements [48, 49, 50], among many other exciting potential properties. However, they have only shown mild promise thus far, due to difficulty in fabrication.

1.6 Nanofabrication- Top down vs Bottom up lithography

Critical to all of the aforementioned applications is the ability to fabricate pertinent structures both for a) experimentation) and b) practical use. Nanostructure shape, periodicity, size, and materials, are all factors which determine the ability of the application, which is important for experimentation, whereas qualities like through put, cost effectiveness, and robustness, are primarily important for implementing plasmonics into practical use. Applications like SERS, which has attained many strides in the last few decades, is at the point of benefitting from processes which can create SERS structures cheaply and effectively, whereas younger fields such as photonic and plasmonic metamaterials, can benefit from processes that can offer more precision in control of shape, size, and material of the desired structure. In all cases, the idea of scaling is desirable, either in the size reduction of nanostructures to attain higher light confinement, or to reach negative refractive indexes in the optical range, or, in the case of SERS, to produce a large but dense array of plasmonic hot spots to allow for portable, accessible sensors. Often, these two desires are juxtaposed. To better understand this dynamic, a comparison between top down and bottom up lithography is needed.

"Top down" fabrication methods, which include electron beam lithography[51], photolithography, and focused ion beam milling, work by starting with a bulk material, for example photoresist, and reducing it down to the desired pattern. For instance, in EBL, a wafer of silicon may be spun coat with a polymer such as polystyrene, then when exposed to a controlled scanning

electron beam, cross links. In developer solution, this cross linked material is removed, leaving a polystyrene mask with which to deposit metal, and, after removal of the mask, the resulting pattern is left. With EBL, features sizes can reproducibly be made down to 10 nm, at best, though state of the art cases using an aberration corrected STEM have reported sizes down to 2 nm [52]. However, consistent pitch and feature spacing are more difficult to attain due to secondary electron scattering, thermal noise, and vibrations. The biggest drawbacks of e-beam are its high cost and low throughput. Direct writing machines cost several million dollars-the conversion of an SEM to an e-beam lithography system still requires around $100,000 in addition to the cost of the SEM. Throughput is currently low, due to the linear nature of the e-beam process and is currently on the scale of hours per wafer. Nano imprint lithography, (NIL) seeks to improve traditional EBL by using it to create a mold, which then, either through hot embossing or UV- based, can be transferred to multiply substrates at a fast rate. However, the size of the stamp and also the resolution of the features are still limited to the throughput of traditional EBL [53].

Bottom up lithography, in contrast, creates a pattern from smaller building blocks. Molecular self-assembly is perhaps the most common bottom up method, and is found in nature, for instance in helical bonding in the DNA. Molecular units organize into ordered structures through molecular interactions. Self- assembly occurs for larger particles as well, such as in nanosphere lithography (NSL), which utilizes the close packing of polystyrene and silica microspheres [54]. Bottom up methods offer faster, cheaper solutions, with higher coverage, but often at the cost of tunability and variability in structures. Nanosphere lithography (NSL) for instance, is a robust, high through put, and very inexpensive bottom up fabrication technique, and while versatile in comparison to some bottom up techniques, can still only achieve a limited number of different structures, in comparison to EBL, which can directly writ a wide variety of patterns drawn by the user, with respect to the

resolution limits. DNA origami [55] has recently shown much promise as a bottom up technique capable of achieving high versatility at small scales, but is still not commercially viable due to the high cost of DNA.

With the advent of optical metamaterials, the relatively new focus on quantum dynamics in plasmon coupling [56], which generally occurs in plasmonic gaps smaller than 2 nm, and the desire to implement plasmonic nanostructures for commercial and medical uses, such as for point of care diagnostics, nanofabrication, which is required to achieve these goals, is limited largely in its ability to be scaled both down and up. On scaling down, smaller gap spacings for higher localized EM fields and smaller structures for optical metamaterials can be attained. On scaling up, dense arrays and assemblies of plasmonic nanostructures can be made in a large area cheaply, and effectively. In this thesis I explore new nanofabrication routes that address both these issues.

1.7 Thesis organization

The work in this thesis predominantly explores bottom up lithography techniques, designed for applicability on both a commercial and experimental level. In chapter 2, I discuss my work on a bottom up nanofabrication technique to achieve a large area of nanocluster assemblies with sub nanometer gap spacings, of varying geometries, using chemical templating and electrophoretic deposition combined with heat, and explore its potential applications to be applied commercially, either as a medical or industrial device. I will discuss the potential applications of nanoclusters assemblies, followed by a discussion on SERS hot spots and plasmonic coupling in dimers. This will lead into my work on nanocluster assemblies- an SEM analysis of the arrays attainable, followed by SERS measurements, TEM analysis, and norepinephrine concentration studies.

In chapter 3, I discuss the foundations for a new nanofabrication process. This is a scaling technique which can be used on either top down or bottom up techniques, and is cheap, fast, and easy to use. First, the concept of scaling is discussed, followed by a brief look at past scaling attempts made both in nano and micro fabrication. Following this I describe three tunable nanostructures. The first two- nanopillar and bowtie arrays- are attained strictly from bottom up lithography. The third, using EBL, combines top down lithography with the thermoplastic film to achieve tunable metasurfaces.

In chapter 4, I revisit the projects from Chapter 3 and chapter 4 to discuss potential future experiments. This entails assessing their potential as future fabrication techniques, the experiments that can and should be done in order to further their usefulness in the field of plasmonics, and how these technologies might feasibly be applied in the future.

1. -Exploration of cluster assemblies

Noble metal particles have garnered interest for over a century [57, 58] due to their unique optical responses from LSPR, where the optical response depends on shape, size, material and dielectric environment. In particular, gold and silver nanoparticles of diameters > 20 nm (due to increased scattering) have been used in imaging, sensing, and spectroscopy. Due to several chemical synthesis, such as the Stober method, metal nanoparticles have become easily available with low polydispersity (5-10% deviations). Nanoparticles can be used for optical labels in bio imaging. When in clusters, defined here as nanoparticles within one diameter or less of one another, the localized fields on the individual nanoparticles can couple, resulting in an enhanced electromagnetic field that red shifts with decreasing interparticle spacing up to the quantum plasmonic coupling regime [59]. Raman scattering, fluorescence emission and infrared absorption can all be amplified by the enhanced field of nanoparticle clusters, which has been used in sensing techniques like

surface enhanced Raman spectroscopy (SERS), Metal enhanced fluorescence (MEF), and surface enhanced Infrared spectroscopy (SEIRA) [60]. Clusters have been also shown to enhance other nonlinear processes such as four wave mixing [61].

Metal nanoparticles can be easily deposited from colloidal to form large random or fractal aggregates, with clusters of random geometries and undefined spacings. While this method has been shown to generate hot spots –confined areas with significantly enhanced electromagnetic fields-, mass density and hot spot density, have been shown to decrease with fractal size. It has also been shown that the strength of the field is higher in individual clusters than in a hexagonal array of nanoparticles, therefore making large aggregates less desirable [62]. Moreover, in aggregates, the exact spectral position of LSPR, as well as the intensities are difficult to control. Especially in applications, like Raman spectroscopy, that involve averaging signals over a large area, some sort of homogeneity of the fields is desirable. The ideal cluster arrangement for applications like SERS, MEF, and SEIRA, require sensors with high field enhancements and low chip to chip variability. For a good sensor, two specific aspects of fabrication need to be considered. 1) Close, and precise, interparticle spacing for the strongest electromagnetic field enhancements possible. 2) Controlled morphology and density of nanostructures. While E-beam lithography is able to achieve the latter, spacings of 10 nm or smaller are very difficult to achieve except on the best state of the art systems. Some bottom up methods[63] have used to DNA to create defined nanoparticle clusters, however, the DNA environment between the spacing has shown to cause quenching from quantum effects even at 2 nm. Additionally, DNA functionalization is high cost. Another technique combines e-beam lithography and traditional nanoparticle attachments [64] to create nanoparticle cluster assemblies with separations below 5 nm. However, for a practical commercial sensor, a third requirement needs to be added in addition to the first two. 3) Low cost, high throughput, and the

ability to be applied on a large scale. Described in the following sections is our method to create nanoparticle cluster assemblies with defined geometry and spacings on the order of 1 nm, in a low cost, robust process that can applied to roll to roll printing.

2.1 Cluster assemblies using chemical templating

Adams et al developed a bottom up nanocluster assembly process, using chemical templating [65]. In short, a polystyrene-b-poly(methyl methacrylate) (PS-B-PMMA) diblock copolymer template was spun coat onto a silicon wafer and annealed at different temperatures to create specific templates with PMMA domains on the length scale of 20 -40 nm. The PMMA domains, when functionalized with an amine group, are able to covalently bond to the carboxylic acid group of functionalized gold nanoparticles, using EDC crossing linking chemistry, allowing for selective chemical attachment of nanoparticles. The confined area of the functionalized PMMA domain allows for nanoparticles to attach within proximity of one another, as shown in fig 2.1, specifically with a distance of 2-7 nm, which falls into the hot spot regime, described next. Nanoparticles were found to cluster into various geometries, specifically, dimers, trimers, and quadrumers. SERS enhancement factors as high as 10^7 were measured. This process was further improved by using electrophoretic deposition to get the nanoparticles to drive to

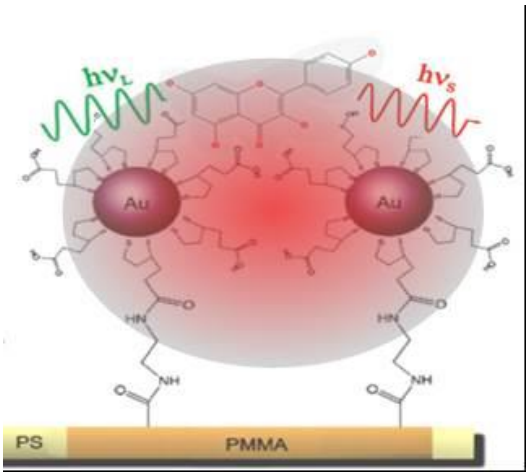

Figure 2.1. Schematic of a nanoparticle dimer ontop of a PS-b-PMMA film. A 20 nm Au nanoparticle, functionalized with thiotic acid, is covalently attached to a functionalized PMMA domain using edc chemistry. The EM field between the two Au nanoparticles is enhanced due to plasmon coupling.

the functionalized surface of the substrate, in opposition to diffusing toward the surface [66]. The result was improved number of clusters, in addition to increased surface spacing, with estimated gaps reaching ~1 nm. However SEM images were unable to image these gaps with better precision and thus determine the exact gap spacing, and the impact of decreasing gap spacing from 2-7 nm to 1 nm was never explored. In this work, nanoparticle cluster assemblies with sub nanometer interparticle distances are fabricated with a slightly improved method. SERS measurements are taken for nanocluster assemblies fabricated from both diffusion and the improved electrophoretic deposition method and compared, with highest EF reaching mid 10^8. The effects of two different chemical templates, with lamellar and cylindrical PMMA domains, on cluster geometry are also analyzed, the former showing a significant increase in clusters per micron. Norepinephrine experiments are also conducted, showing a detection limit of at least 200 parts per billion. The potential effect of the subnanometre spacings due to quantum effects is also discussed. This is significant from a fundamental and practical level as next discussed.

2.2 Plasmonic hot spots in nanoparticle dimers

Plasmonic hot spots are highly localized field regions, found either in sharp metal edges, which is attributed to the so called "lightning rod" effect, or in nanoscale metal junctions, with reported SERS enhancement factors as high as 10^9[67].It is believed that most of the SERS signal is usually due to hot spots. For example, it has been shown that in a dimer of two 25 nm silver nanoparticles spaced 2 nm apart, that the 1 molecule in the hot spot produces 285 times as much signal as the average molecule on the nanoparticle surface. In many cases the dimer is considered the simplest

model for plasmon hot spots, and is also the basis for tip enhanced Raman spectroscopy (TERS), which utilizes the hot spot generated between a metal tip and sample at close gaps [68].

Hot spots, when generated from multiple plasmonic structures, is a result of plasmon coupling, where the strength of the coupling is predicted to increase with decreasing distance between the nanostructures. Using the dimer as a basic model, plasmon coupling can be thought of as a hybridization of the dipolar resonant mode from each individual particle. Analogous to molecular orbital theory, Prodan et al have developed a hybridization model for plasmons modes between two closely spaced structures, which describes symmetric and antisymmetric coupling of plasmon modes (bonding and antibonding), the former being lower in energy[69]. In the case of a dimer, the mixing of two dipolar modes leads to stronger hybridized bonding modes existing within the junction of the two nanoparticles, the lowest energy mode which is shown to red shift and increase in intensity as the spacing decreases. Classically, this occurs until the particles begin to merge, creating a conductive bridge between the two of them, resulting in charge transfer plasmon mode (CTP), that, as the two particles continue to merge, begin to resemble the plasmon mode for an oblong single nanoparticle.

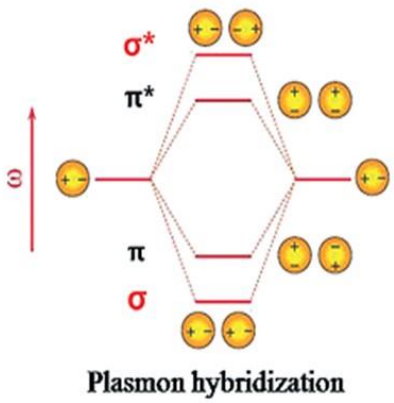

Figure 2.2. Plasmon hybridization model, analogous to molecular orbital theory. The dipolar mode of two particles are coupled symmetrically and asymmetrically, leading to lower and higher energy modes, respectively. Reproduced from [Ref 70] with permission of The Royal Society of Chemistry. http://dx.doi.org/10.1039/C4TC01142B

Fig 2.2 shows the linear combination of two dipolar modes from two nanoparticles, in analogy to molecular orbital theory [70]. As shown, the dipolar modes can combine in and out of phase with one another, leading to a lower energy bonding mode (σ) and a higher energy antibonding mode (σ*), where σ exists in the gap of the dimer, and results in higher enhancement of the field and a redshift, and σ* results in localized electric fields at the ends of the dimer, and a blue shift. It should be noted that for the case of a dimer with spherical particles, the out of phase case does not exist, as the dipoles opposite one another cancel each other out. This is the case for an incident wave traveling along the longitudinal axis of the particle. For the transverse axis, the in phase and out of phase arrangements reverse, although the overall enhancement is weaker.

Classically, the enhanced field within the junction of a dimer is predicted to enhance as the spacing of the junction decreases. Fig 2.3 shows simulated field enhancements, using a high frequency structure simulator, for dimer, trimer, and linear quadrumer nanoparticles with a diameter of 20 nm and a varying gap from 4 to 1 nm. As predicted, the field increases for decreasing spacing. Also, there is a redshift with decrease in spacing. Of significant note is the huge increase in enhancement, in all three cases, when changing the spacing from 2 to 1 nm. These simulations were ran based on our substrates, and therefore were using the appropriate dimensions and permittivities. Based on these enhancements, and using $|E_c/E_0|^4$, one would expect enhancement factors on the range of ~10^9 to10^{10}, for clusters of like geometries with nm spacings. Considering that the gap spacings using the diffusion method were in the range of 2-7nm, the previous reported enhancement factors of ~10^7 make sense based on these simulations. Considering the enhancement from 2 nm to 1nm increase by 100 fold, it is obvious that small gap spacing are desirable. Also of note is the difference in enhancements in geometry, where the linear quadrumers have a field enhancement of almost 25% higher than that the dimers. Therefore, clusters of higher particle

number, especially linear chains, and spacings down to 1 nm, are highly desirable for the strongest fields possible.

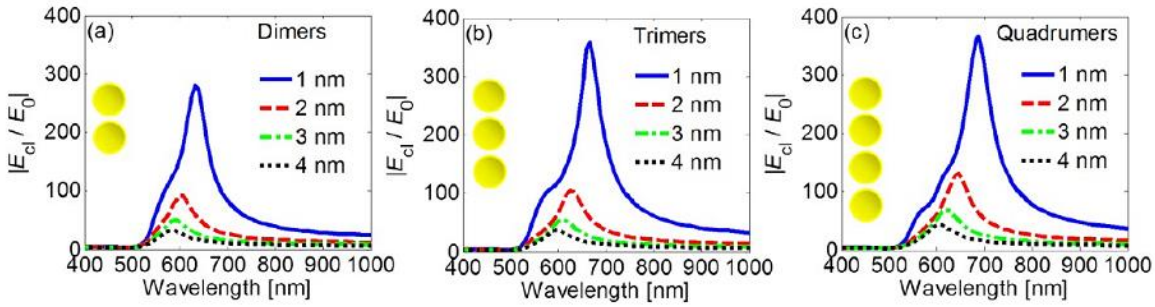

Figure 2.3. Calculated electric field enhancements for 20 nm Au nanoparticles in a_ dimers, b linear) trimers,) and c) linear quadrumer geometries. Four gap spacings are calculated for each case using a plane wave orthogonal to the surface, with an electric field polarized along the axis the cluster. Full wave simulations employing the finite element method are used. Reprinted) with permission from (66. S. M. Adams, S. Campione, F. Capolino, and R. Ragan, "Directing Cluster Formation of Au Nanoparticles from Colloidal Solution," Langmuir, vol. 29, no. 13, pp. 4242–4251, Apr. 2013). Copyright (2013) American Chemical Society

2.3 Fabrication

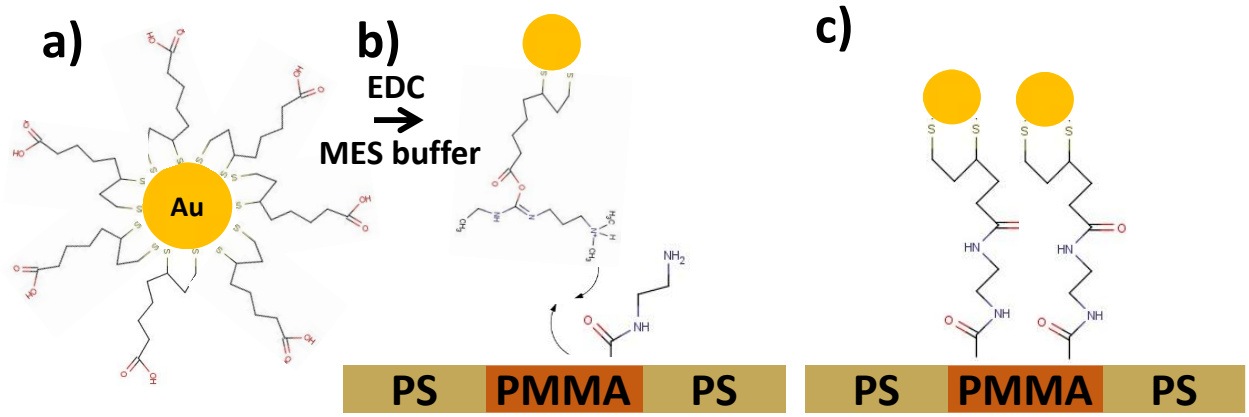

Figure 2.4. Schematic of the EDC chemical attachment used for nanocluster assembly. In A, a citrate stabilized 20 nm Au nanoparticle is functionalized with thiotic acid. In b), the functionalized nanoparticle covalently bonds to a PMMA domain functionalized with amine surface end groups, using a chemical cross linker of EDC/S-NHS. C) Shows two nanoparticles attached to the PMMA domain, resulting in a dimeric structure.

Materials: Random copolymer Poly(styrene-co-methyl methacrylate)-α-Hydroxyl-ω-tempo moiety (PS-r-PMMA) (Mn = 7,400, 59.6% PS), and diblock copolymer poly(styrene-b-methyl methacrylate) (PS-b-PMMA) (Mn = 260-b-63.5 kg mol-1, for cylindrical template and diblock copolymer PS-b-PMMA with Mn = 170-b-144 kg mol-1 for lamellar template) were purchased from Polymer Source, Inc. (Dorval, Canada). For the diffusion deposition, boron-doped silicon wafers with resistivity of 1-10 ohm-cm were purchased from University Wafer (South Boston, MA). For electrophoretic deposition (EPF), Si wafers with resistivity of 0.001-0.004 ohm-cm were purchased from Virginia Semiconductor (Fredericksburg, VA). Sodium citrate, sodium hydroxide (NaOH), and hydrofluoric acid (HF) were purchased from Fisher Scientific (Pittsburgh, PA). 2-(N-morpholino) ethanesulfonic acid (MES) 0.1M buffer, 1-ethyl-3-[3-dimethylaminopropyl]

carbodiimide hydrochloride (EDC), and N-hydroxy sulfosuccinimide (S-NHS) were purchased from Pierce (Rockford, IL). Gold(III)chloridetrihydrate (HAuCl4•3H2O), DL-6,8-thioctic acid (C8H14O2S2) (TA), dimethyl sulfoxide (DMSO), ethylenediamine (ED), toluene, ethanol, isopropanol (IPA), and 52-mesh Pt gauze foil were all purchased from Sigma Aldrich (St. Louis, MO). Nanopure deionized water (DI) (18.2 MΩ cm-1) was obtained from a Milli-Q Millipore System. AFM TIPS

Diblock Copolymer Templates: Si wafers were cleaned with7:1 DI:HF. A solution of 1 wt% (PS-r-PMMA) random copolymer, in toluene, was deposited onto a clean Si wafer by spin coating at 3000 rpm for 45 s. After spin coating, a PS-r-PMMA brush layer was annealed for 72 hours in low vacuum at 170° C. PS-r-PMMA/Si was then cleaned by rinsing with toluene while spin coating at 3000 rpm in order to remove unbound polymer. A solution of 1 wt% PS-b-PMMA (PS/PMMA =260 kg mol^{-1} / 63.5 kg mol^{-1}) or 1 wt% PS-b-PMMA (PS/PMMA =175kg mol^{-1} / 145 kg mol^{-1}) in[RR1] toluene, for the cylindrical and lamellar domain types, respectively, was applied onto r-PMMA coated wafer at 5000 rpm for 45s; afterward the sample was annealed for 48 hours at 170° C. The PMMA regions of the template were functionalized with amine surface end groups by immersing the whole sample in ED in DMSO (2% v/v) for 5 minutes. Additional details can be found in (insert Nanotech and Small ref.).

Au Nanoparticle Functionalization: 20 nm diameter Au nanoparticles were synthesized from a 0.01 wt% $HAuCl_4$•$3H_2O$ in aqueous sodium citrate solution, from the Turkevich method. A 1wt % aqueous colloidal solution of sodium citrate stabilized, 20 nm Au nanoparticles, was centrifuged and washed once, followed by replacement with NaOH solution with 11.67 PH, to avoid aggregation of nanoparticles. The solution was then functionalized with DL-6,8 thiotic acid in a (.5 mM) TA solution, in ethanol, for 18 hours at room temperature with constant stirring. Afterward,

excess TA was removed by centrifugation and the solution was resuspended in DI at twice the initial nanoparticle concentration, with a PH of 8.0. For chemical attachment of Au nanoparticles to PMMA regions on PS-b-PMMA, a chemical cross linker EDC/S-NHS was added to the aqueous TA functionalized colloidal solution. The concentrations of EDC and S-NHS in a 0.1 M MES buffer, were 38 µM and 95 µM, respectively. Addition of cross linker happened immediately before exposure to PS-b-PMMA surfaces in order to minimize nanoparticle aggregation.

Chemical crosslinking attachment: The 20 nm TA functionalized Au nanoparticles were selectively attached to the functionalized PMMA domains via electrophoretic deposition (EPD) and diffusion, which served as the control. In the latter method, the ED treated PS-b-PMMA film on Si was immersed in the Au colloidal solution with cross linker, face down at 40°C for 120 min. After the first hour, the colloidal solution was replaced with a fresh batch, to avoid aggregation. In the EPD method, the ED-treated PS-*b*-PMMA thin film on Si was suspended vertically and parallel to a Pt mesh electrode in a 10 mL beaker, and served as the anode. The beaker was then filled with 4 mL of the TA functionalized Au np solution with cross linker. A BK Precision 1621a DC Regulated Power Supply was used to apply a voltage of 1.2 V, for two ten minute rounds, each with fresh solution. Both EPD and control samples were rinsed with IPA and dried under nitrogen. Additionally, the EPD method was further investigated by the addition of a hotplate, heated at 90 C. To avoid aggregation due to heat, the substrate was given a fresh solution of gold nanoparticles every ~4 minutes. This was done four times.

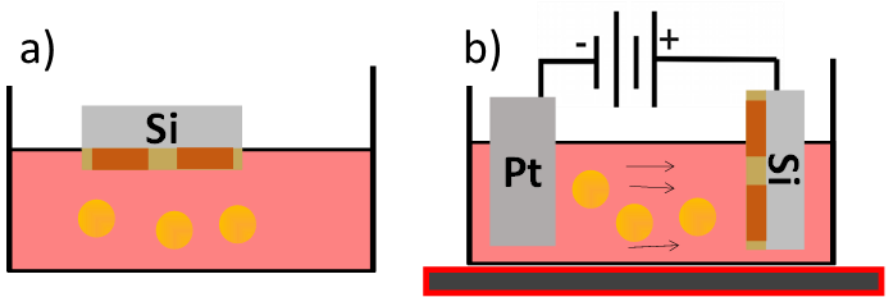

Figure 2.5. A) A silicon wafer with a PS-b-PMMA template is immersed into a solution of gold nanoparticles and edc/SNHS solution for two hours. Nanoparticles diffuse toward the surface of the template. B) A silicon wafer with a PS-b-PMMA template placed directly across from a PT electrode. A voltage is applied to the PT and Si substrates using a DC voltage supplier and alligator clips. The electrophoretic force drives particles across the surface toward the Silicon substrate.

2.31 Analysis:

The effects of the deposition method and copolymer morphology on the cluster geometry attributes were analyzed in SEM images, over approximately 10 different regions with area sizes ranging from 2.6 μm × 2.6 μm to 6.0 μm × 6.0 μm. Cluster percentages were counted according to number of particles in a particular cluster, i.e. dimer, trimer, quadrumer, and then divided by the total area (in micron) to get the average percentage of particles in a given cluster per micron. Specifically, the cluster type density was determined as:

$$x = \frac{\sum \text{Area size} * (\text{ \# of particles in a cluster/ area })}{total\ area}$$

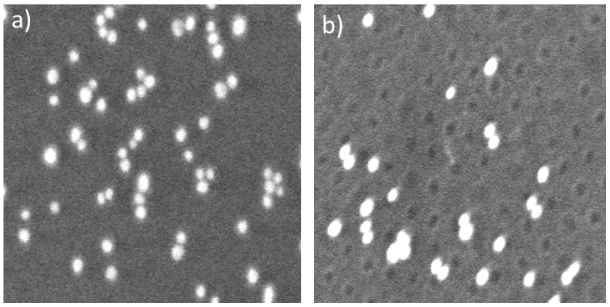

Figure2.6. SEM images of two nanoparticle assemplies formed from EPD on the cylindrical template. In A), the EPD was conducted on a hot plate at 90 °C. in B), EPD was conducted at room temperature.

Heat vs no heat: As shown in figure 2.6, the effects of heating the solution at 90°C resulted in an increased cluster coverage. Table 2.1 shows the number of single particles, particles in dimers, trimers, and linear quadrumers, and particles in aggregates for cluster assemblies fabricated using EPD with and without a hot plate. The numbers reported are as the total number of particles counted over the total area used, resulting in number of clusters per micron. For the purposes of this chapter, aggregate can be defined as particle groups of 5 nanoparticles are larger. On average, the heated substrate had~30% more clusters than the unheated substrate. The number of single particles were close to the same, although aggregation also increased by about 7%. It is important to note that this finding largely occurred near the water, air interface on the substrate. This is likely to the added capillary force from the increased rate of evaporation, and also to the convective force from the heated solution. Also, specific regions of the substrate had large aggregates on the substrate, with as many as 200 np. These aggregates were visible on a microscope as gold streaks and were taken into account when performing SERS experiments. The rest of the experiments were conducted using EPD samples with the added addition of heat, due to the areas with an enhanced number of clusters.

Epd vs diffusion: Shown in figure 2.7 are SEM images of nanocluster assemblies on a) b40 , using diffusion, hereafter called the control, b) b40 using EPD, hereafter called cylindrical and c) lamellar using EPD, hereafter called lamellar. Images d), e), and f), show up close SEM images of the control, cylindrical and lamellar clusters respectively. From the SEM images, it is estimated that the cluster gaps in the control are between 2-4 nm, whereas the gap between clusters formed using EPD is on the order of one nm. Fig 12 (bottom right) shows the average number of particles per cluster type taken over a range of areas. The formula used here is slightly different from above, where each spot is averaged individually, and therefore the total number is reported with standard deviation. The total number of single nanoparticles per micron for samples shown in Figure 12 (a)-(c) were calculated as 217±74, 79±15, and 67±3 respectively. The number of dimers per micron was determined to be 49 ±18 (control), 64±10 (EPD cylindrical), and 74±5 (EPD lamellar) for Figure 12 (a), (b), and (c), respectively. The number of trimers per area for Figure 2 (a)-(c), were 20 ±14 (control), 41±20 (EPD cylindrical) and 52±22 (EPD lamellar), respectively. Significantly the number of aggregates, which is defined as clusters with more than four nanoparticles (n>4), in Figure 12 (a), (b), and (c), were calculated as 7±10 (control), 69±18 (EPD cylindrical), and 32±12 (EPD lamellar), respectively. Both EPD samples had significantly higher aggregation than the diffusion sample. This is in part from the addition of heat to the solution when using EPD, which was shown to produce slightly more aggregates. Additionally, the voltage results

#cluster	90°C	R.T
single	77	75
Cluster	109	79
Aggregate	67	62

Table 2.1. Number of particles in cluster type per micron for EPD samples made from 90°C and R.T (25°C).

in a greater number of particles approaching the surface, which in turn leads to a greater a number of aggregates on the surface. The diffusion sample also had a significantly greater number of single nanoparticles, which may be a result of the two hour exposure in solution as opposed to twenty minutes of the heated diffusion. In the cases of dimers, trimers, and linear chains, both EPD samples had significantly higher coverage than the control. This is in agreement with previous results, where the particles are expected to be driven in close proximity due to the applied voltage. For purposes of SERS enhancements, the lamellar sample shows to be the most promising template on almost all accounts. Its dimer, trimer, and linear chain count are all higher than the cylindrical by ~20 percent, with significantly less variation. It also showed on average half as many aggregates as the cylindrical sample. It should be noted that the coverage on the EPD substrates were not uniform when analyzed over the entire substrate. Most particles were driven near the water air interface, which is where the majority of SEM regions were taken. This comprised about of roughly a 4x6 mm area, where the entire

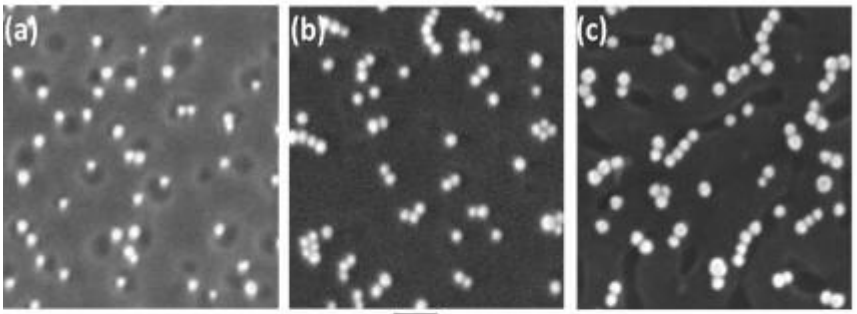

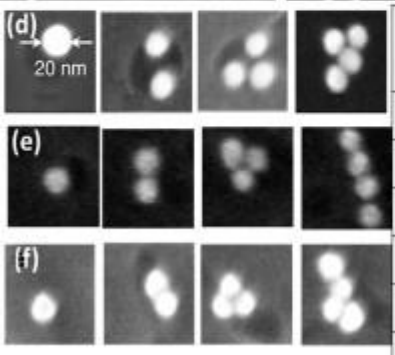

 # Particles per micron

Cluster type	B40	LAM.	DIFF.
1	79±15	67±3	217±74
2	64±10	74±5	49±18
3	41±20	52±22	20±14
4	21±6	21±5	2±3
5	69±18	32±12	7±10
linear	28±8	36±5	9±9

Figure 6.7. A) SEM of nanocluster assembly deposited on a cylindrical template using diffusion method (control). B,) C), SEM images of nanocluster assemblies assembled on cylindrical and lamellar templates, respectively, using the EPD method. D) e) f) show close up SEM images of single nanoparticle, dimer, trimer, and quadrumer geometries, respectively. The table (bottom right) shows the number of particles per cluster type per micron for the cylindrical (b40) lamellar, and diffusion cases. Aggregates are defines as clusters with a nanoparticle count >4.

substrate of the diffusion method has similar coverage. Optimizing this process to achieve similar coverage from the heated EPD over the entire substrate will be the focus in further investigations.

2.4 SERS

Surface enhanced Raman scattering (SERS) measurements with a benzenethiol analyte were conducted using a Renishaw Micro Raman system and custom built micro-Raman system with laser excitation wavelengths of 785 nm, and 633 nm, respectively. Samples were immersed in a $4x10^{-3}$M solution of benzenethiol (BZT) in EtOH for 2 hrs. followed by a 60s MetOH and EtOH rinse, to remove excess material and leave a molecular monolayer of benzenethiol on the surface. For the 633 nm setup, a 100x .90 NA objective was used. Powers ranging from .1mW to 1mW were used, with integration times ranging from 1 to 60s. For the 785 nm excitation, integration times were varied from 3 to 30 s using a laser power of ~2.5 mW. The illumination spot size was 2 um in diameter, and the objective used for collection was 50X and having a 0.75 NA. A solution of neat benzenethiol was also collected at same conditions for to provide a standard for enhancement calculations, where EF = $(I_{SERS}/N_{SERS})/(I_{neat}/N_{neat})$. I_{SERS}, I_{neat}, N_{SERS}, N_{neat} are the SERS and neat Raman intensities, and the number of molecules for each measurement, respectively. The SERS intensity is normalized using power P and integration time *t*, where $I_{SERS}=I_{raw}/(P.t)$. The neat Raman intensity, I_{neat} is normalized in the same way. The number of molecules measured for N_{SERS} was found by normalizing the area excited in the laser spot size by the gold coverage of the surface, where $N_{SERS}= \rho_{surf} N_A/(f_{Au} A_{spot})$. The surface coverage of benzenethiol, ρ_{surf} is reported to be .54 nmol/cm^2 , which when multiplied by Avogadro's number, N_A, and divided the spot size, A_{spot} gives the number of molecules participating in the measurement. This is then normalized by f_{Au}, the gold nanoparticle fractional coverage. To determine the number of molecules measured from the

solution, $N_{neat}=\rho_{neat} V$, where ρ_{neat} is the density of benzenethiol, 9.739 mmol/cm^3 and V is the scattering volume, which can be calculated by multiplying the spot size of the laser by the collection depth, both values measured for the 785 nm setup. For the 633 nm Raman setup, a different technique for the standard was used. A 5 ul drop of neat benzenethiol was drop coated on a gold covered glass slide and allowed to dry into a ~.5mm spot. Over 80 Raman spectra were taken and averaged across the diameter of the spot. The number of mols Nsers was then taken as the spot size multiplied by the number of mols in 5 uL of pure benzenethiol, divided by the area of the spot. This was done to rule out potential errors in measurement of the spot size or focal volume, as the setup was limited to a mechanical stage, constraining the ability to properly measure these quantities.

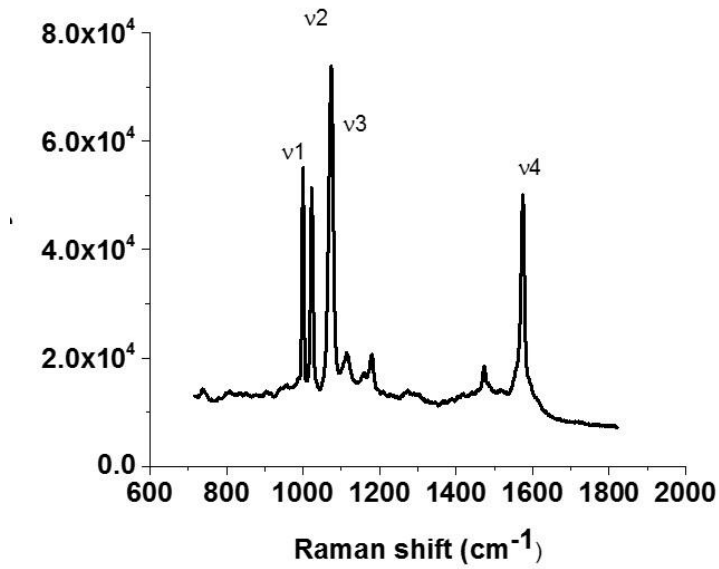

Figure 2.8. SERS spectra of BZT from a 785 nm excitation at 2.5 mW and 5s integration time

Shown in fig 2.8 is a SERS spectrum of an EPD lamellar sample taken at 785nm excitation, with the four peaks, 998cm^{-1}, 1021cm^{-1}, 1071cm^{-1}, and 1573 cm^{-1} labeled. To calculate the enhancement factor, EF, both the 998cm^{-1} and 1573cm^{-1} peaks are used. For the 633 nm excitation, a polarized HeNe laser was used. To properly measure the SERS effect of our substrates, a wave plate was

rotated every ten degrees to a total of 180 degrees. As expected, there was variation in our SERS signal as a function of a polarization, where the difference in maximum to minimum intensity sometimes reached as high as a third. SEM images showed that about 50% of linear chains either lie on the x or y axis, and therefore the maximum SERS intensity was multiplied by two to achieve the final intensity used for SERS. This was not the case for the 785 nm setup, where polarization was not an issue. It was found on the 633 nm excitation that powers above ~1mW resulted in a decrease in SERS signal after a period of time ranging from 10 to 60s. This is potentially due to the field enhancement of the laser either damaging the substrate or, more likely, the monolayer of analyte. Integration times as low as 1s with powers as low as .05 mW still showed signal for the EPD samples, making the substrate potentially useful for diagnostic studies requiring fast analysis and low power to avoid damaging certain analytes. Also note that high intensities were found over the entire 4x6 mm area, analyzed above in SEM, for both EPD samples. For the 785 nm excitation, powers as high as 5 mW were used without damaging the substrate. This may be a result of the field not being in resonance there, and thus the local area experiences a less powerful field. In fact, intensities were only measured near regions which appeared gold under the microscope, and the SERS effect for the 785 nm excitation may be indeed from large aggregate regions, which can be easily created using the heated EPD method, by extending the time of nanoparticle immersion. It should also be noted that all SERS substrates were reusable. Reimmersing the substrates in more benzenethiol solution every few days yielded the same SERS results.

Figure 2.9 a, b shows calculated enhancement factors for the 998 $cm^{-1}$and 1573 cm^{-1} peaks, respectively, at the 633 nm excitation for the control (diffusion using a lamellar substrate), cylindrical, and lamellar substrates. As shown, the highest measured EF (998cm^{-1}) for the control

was on the order of ~$1x10^7$, whereas the cylindrical sample went as high as ~$7x10^7$ and the lamellar as high ~$4x10^8$. The 1573 cm^{-1} peak shows similar enhancements. Based on the number of clusters per micron, as discussed previously, the trends in enhancements make sense. Both EPD samples have higher number of clusters than the control, and the lamellar has a higher number of clusters and linear chains than the cylindrical, leading to enhancements almost a factor of ten higher than the cylindrical. This is an example of the importance of template design, and the significance of cluster geometry on impacting high field enhancements. Ideally, new template designs can lead to optimized geometries for optimal enhancement signal. For the fairest comparison between the EPD and diffusion samples, the lamellar only should be compared. Here, we see about a 50 fold enhancement, which would be expected not only based on the higher number of clusters, but due to the closer gap spacing in the EPD sample. This line of discussion will be the point of focus in the next two sections. Figure 2.10 am) shows enhancement factors for the 998 cm^{-1} and 1573 cm^{-1} peaks, respectively, for diffusion and b40 samples using a 785 nm excitation. Surprisingly, the EPD sample shows highest EF at about $2x10^7$. The diffusion sample showed EFs on the order of only 10^5, suggesting that the enhancements for the EPD on the 785 nm excitation are from the aggregated regions.

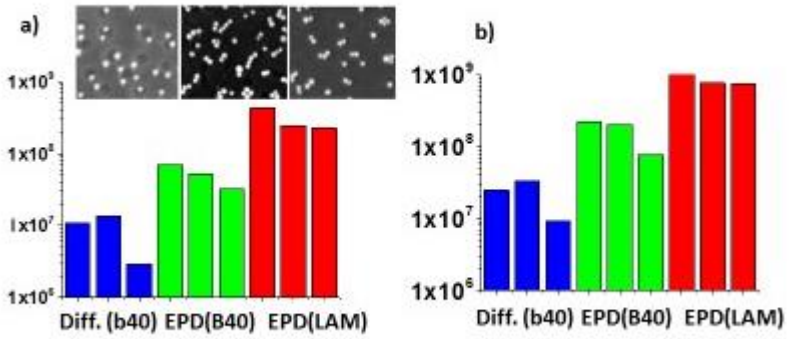

Figure 2.9. SERS enhancement factors at three different locations for the diffusion, B40, and lamellar samples using a 633nm excitation. A) Shows EFs based on the intensity of the 998 cm^{-1} BZT peak. B) Shows EFs based on the intensity of 1573 cm^{-1} BZT peak.

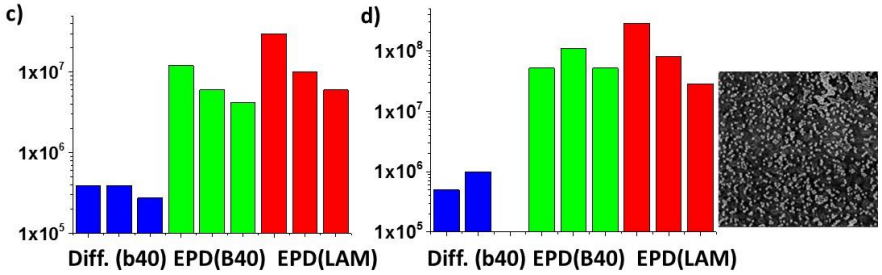

Figure 2.10. SERS enhancement factors at three different locations for the diffusion, B40, and lamellar samples using a 785 nm excitation. A) Shows EFs based on the intensity of the 998 cm^{-1} BZT peak. B) Shows EFs based on the intensity of 1573 cm^{-1} BZT peak.

2.4.1 Determining the plasmon resonance

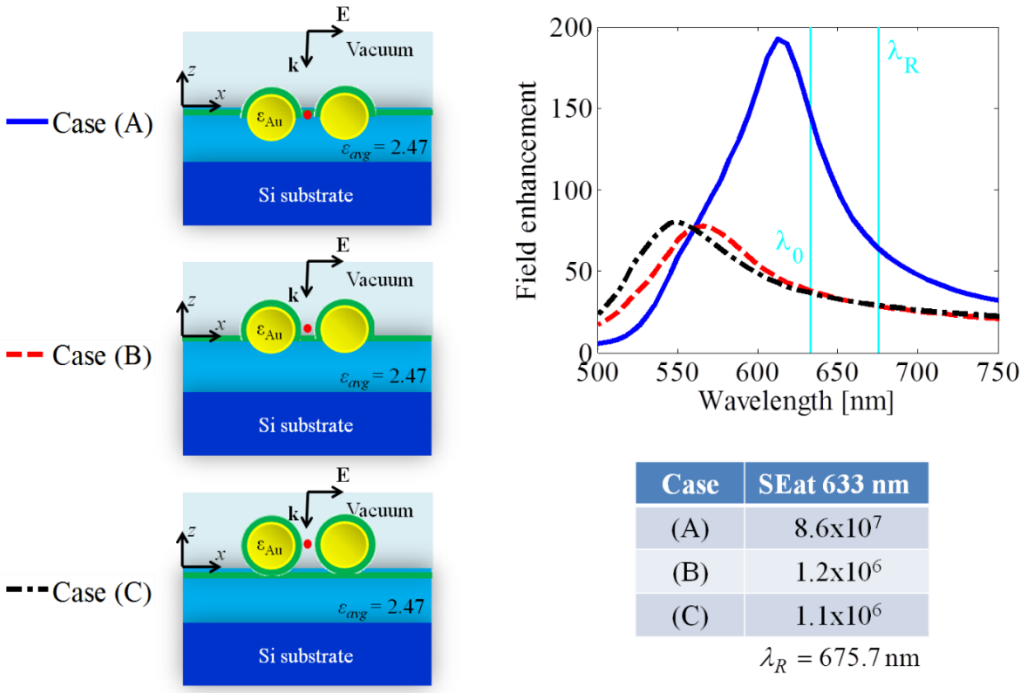

Case	SEat 633 nm
(A)	8.6×10^7
(B)	1.2×10^6
(C)	1.1×10^6

Figure 2.11. (Left) Three depictions of two 20 nm gold nanoparticle dimers with a gap of 1 nm. All three cases show the particles in vacuum, on top of a PMMA film and coated with a monolayer of benzenethiol. The average permittivity used is 2.4. Case A has the particles half embedded in the permittivity, case B, partially embedded, and Case C, not embedded at all. (Right) Full wave simulations, showing the plasmon resonance, for case A, B, and C, where the field enhancement is measured in the center of the gaps. Calculated enhancement factors, based on simulations, are given for all three cases for a 633 nm excitation.

In order to evaluate the plasmon resonance of our structures, full-wave simulations employing the finite element method (high frequency structure simulator, HFSS, by Ansys Inc.) were performed for our structures. Figure 2.11 shows calculated electric field enhancements from dimer nanopartcles with 1 nm spacing. We modeled three different scenarios for 23 nm Au nanoparticle dimer clusters on the PS-PMMA substrate, referred to as Case A Case B, and Case C on the left part of Figure 17 when calculating SERS EF using full wave simulations. In Case A, the particles

are partially embedded in a layer of PMMA and BZT, where the permittivity, E_{avg} is an average of both permittivities. This is to account for the fact that the particles may be slightly embedded in the PMMA domain, which has a thickness of 2-3 nm, and for the benzenethiol monolayer in the particles. AFM topography images indicate that PMMA domains on PS-b-PMMA diblock copolymer templates can become slightly recessed after exposure to ethylenediamene. At larger spacing, the BZT would likely have little effect, however, since our particle spacing is estimated to be sub nanometer, the dielectric of the BZT could have influence in this particular case. In Case B, the particles reside mainly on the surface, and in Case C, entirely on the surface. In all cases, simulations illuminate the dimer with a plane wave with normal incidence to the surface.

The electric field enhancement is calculated as E_{cl}/E_o, where E_{cl} is the calculated electric field occurring between Au nanoparticle dimers with inter-particle spacing of 1 nm, to reflect spacings observed in SEM images of EPD E_o is the plane wave field without clusters in benzenethiol solution, with permittivity of 4.21 [reference here]. This mimics the experimental conditions of using a neat solution of benzenethiol to calculate the SERS EF in equation 2. The electric field is polarized along the axis of the linear cluster, with excitation wavelengths varied between 400 and 1000 nm.

Case A shows a plasmon resonance at approximately 630 nm, and this shifts down to about 550 nm case B and 530 nm Case C. The calculated SERS enhancement factors were calculated as $|E_{cl}/E_o|^2$ simulated at the excitation wavelength and multiplied by $|E_{cl}/E_o|^2$ simulated at the Raman shifted wavelength. For 633 nm excitation, SERS EF for Cases A , B, and C are 8.6×10^7, $1.2\text{x}10^6$, and 1.1×10^6, respectively. It should be noted that no SERS signal was found for the 532 nm excitation, and was thus no calculated EFs for 532 nm excitations were reported here. The

SERS data suggests that our data fits closer to Case A, and if so, we expect the resonance to be near 633. Note that the highest enhancement factor reported for our clusters was mid 10^8, almost an order of magnitude higher than that predicted by the simulation. This can be easily accounted for due to chemical enhancements, which can add one to two orders of magnitude in enhancement, and is not accounted for in the simulation. Additionally, other geometries were not simulated, but from previous simulations, higher fields are expected in those cases, and therefore our assemblies should have a measured EF at least as high as that predicted for the dimer case.

2.4.2 Exploring the gap

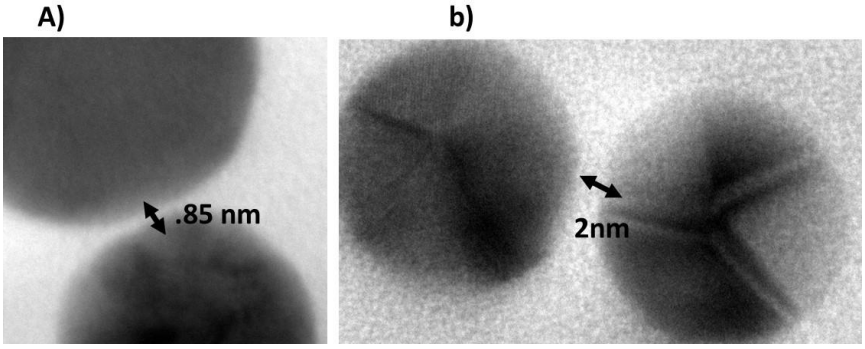

Figure 2.12. TEM images of gold nanoparticle dimers fabricated onto a Cu TEM grid using a) EPD method and b) diffusion.

As reported in previous experiments, the electrophoretic deposition has led to narrower gaps in the clusters, with gap spacings smaller than 1 nm. Hitherto, a more precise distance was not known, due to the limitations of SEM resolution. To further analyze our samples, the EPD samples were made on copper TEM grid, as described above with silicon, although lower concentration of nanoparticles was used to achieve lower concentration. Figure 2.12 shows TEM images for the EPD and diffusion samples. As predicted, the gap spacing for the diffusion is about 2-3 nm, whereas the gap for the EPD dimers is ~.85 nm, which falls close to the regime for quantum interference, either from screening of tunneling or surrounding electrons. The EPD and

diffusion samples were next measured for SERS intensity as a function of power. Diffusion and EPD samples were illuminated with a 633 nm HeNe laser at integration times of ten seconds, from a range of .1mW to .8mW. Fig 19 shows plots for both EPD and diffusion, in addition to the same power test for a drop coated spot of neat BZT on a gold coated glass slide. It should be noted that laser powers beyond 1 mW likely began to burn the BZT molecules, as a decline in signal after several minutes was observed. Also, SERS intensities were collected as a function of decreasing power, rather than increasing power. As shown in Fig 2.13, the intensities for the EPD are all greater than the neat BZT, whereas the diffusion is lower. Also significant is the change in slope as the intensity approaches .8 mW. For the control sample, the slope actually increases, which matches well with the slope from the pure BZT. Conversely, the slopes for the lamellar cases decrease. It is hypothesized that this is potentially due to increased electron screening, which yields a lower enhancement factor, and is indicative of nonlinear effects [71]. Further experiments involving electron energy loss spectroscopy (EELS) are planned for the future. To maximize SERS enhancement factors, the gap spacing may need to be optimized.

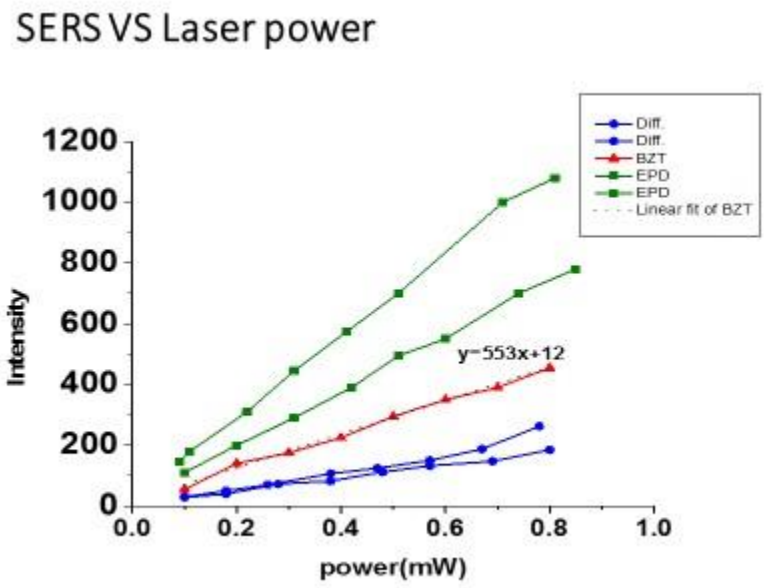

Figure 2.13. SERS measurements for nanocluster assemblies fabricated from EPD (lamellar) and diffusion (lamellar) as a function of power. A 633 nm excitation was used. For reference, neat BZT was deposited on a gold slide to form a crystalline spot. The neat BZT was also measured as a function of power and plotted here.

2.4.3 Norepinephrine Concentration Studies

Our SERS substrates ideally will be used as a diagnostic tool. As proof of concept, norepinephrine studies vs concentration were conducted for EPD samples using the 785 nm excitations, from concentrations ranging from 40ng/mL or 40 ppb, to 1 mg/mL or 1 ppm. This was achieved by placing a droplet of norepinephrine in DI with 5% dextrose, over the EPD sample. The droplet was than probed with 5 mW power for 15 s. Figure 2.14shows the SERS vs concentration for 785 nm excitation. Interestingly, even with the 785 nm excitation, norepinephrine was detectable, with a detection limit of 200 ppb, which is higher than similar experiments [72].

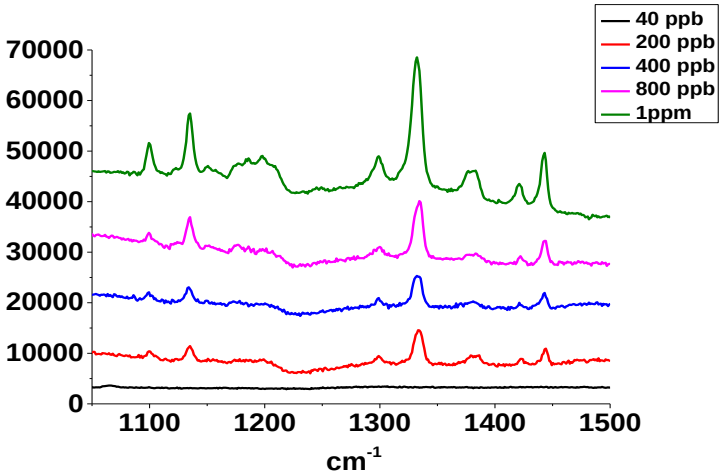

Figure .14. SERS spectra for norepinephrine solutions of varying concentrations using an EPD b40 sample and a 785 excitation. Measurements were taken by bringing a 50 X .75 NA objective within working distance of the sample. A mm sized droplet of the norepinephrine solution was placed between the objective and sample. 5 mW and 15 s integration time was used.

2.4.4 Summary

Plasmonic nanoclusters of particles with 20 nm have been fabricated using a low cost, high through put method. By adding heat to the electrophoretic assembly, cluster count was increased by 30%. The lamellar template showed the most optimal cluster assembly for SERS, both in SEM analysis and from SERS intensity. Tem analysis showed the gap to be in the sub-micron range. This is potentially detrimental, as plasmonic gaps starting at ~ .5 nm begin to experience quenching of the field due to quantum effects. The gap therefore should be optimized. Norepinephrine concentration studies showed a detection limit of beneath 200 ppb.

3. Scalable arrays

Three main objectives to improving nanoscale lithography are to 1) produce patterns with smaller feature sizes 2) produce them with higher precision and 3) do so quickly and at higher through put. A scalable (reducible) element can achieve all three simultaneously, by taking an initial pattern and reducing it in a controlled, continuous matter down to the desired new size. Scaling promises to benefit lithography in general, from both a practical and experimental standpoint. Expensive, time consuming methods utilizing EBL are often impractical on a commercial level. A facile scalable method can be used to improve feature sizes of more inexpensive fabrication methods, such as NSL. Experimentally, size dependent studies currently rely on multiple fabrications. A continuous scaling method, which can precisely define the new special features, as well as create them from the original pattern, can eradicate the source of error found from inherent size variations when fabricating multiple patterns, as well as allow for facile generation of more data points. Both of these advantages are particularly important for experiments exploring plasmon coupling, which depend on gaps changing by nanometer and even sub nanometer differences, the latter exceeding the resolution attained by EBL. Few attempts have been made at producing large area, nanoscale arrays that can easily be reduced to a desired smaller scale. Lee et Al developed a PDMS based technique to create new master templates from a single master [73]. A thermoplastic pre-stressed polystyrene film was used to reduce the initial pattern spacings by 50%, and reduce critical feature sizes by 45 %, with lowest spacings reaching 200 nm. Nguyen et al. developed a related technique using a polyolefin pre-stressed film, which reduces surface area by 95% [74]. Using a proof of concept ink jet printer, they were able to reduce mm sizes lines by 77% in length. However, neither of these techniques as of yet have been introduced to the nanoscale, defined as 100 nm or less. As a

result, tuning the plasmon resonance, perhaps the most interesting aspect of scaling in addition to increasing feature density, was not shown in either of these experiments.

3.1 Scalable structures using a Polyolefin film

Thermoplastic substrates are initially prestressed plastic films, which reduce back to their original dimensions when heated. These films have been exploited in the last few years to produce wrinkled metallic nanostructures for MEF, in work by Sharma et al. [75]. This was accomplished by coating the thermoplastic with a metal layer, which buckles as the surface area of the substrate is reduced. In similar work by Zhang et al [76], a polystyrene film (PS) was used to generate wrinkled nanoporous Au/Ag films, generating hot spots with SERS enhancements factors over 10^9, high enough for single molecule detection. However, the frequency and location of hot spots generated from the metal wrinkles are not controllable. Furthermore, the wrinkled nature of the metal wrinkle film limits the number of applications that can be used. Ideally, the film can be used to generate small spacings in a controlled manner, by combining the heat shrink film's properties with traditional lithography. This opens up the film's potential for a wide ranger range of applications, including controlled biosensing, AR reflective properties, and even potentially plasmonic metamaterial substrates. Nguyen et al. has shown proof of concept of this possibility, using an ink jet printer, that the polyolefin film can be used to reduce patterns by 95% in surface area and 77% in length [74], while maintaining the X and Y dimensions. However, this experiment was limited to the macro scale. I show here that the polyolefin pattern reduction capability can be utilized even at the nanoscale. I have shown the film can be used to both optimize bottom up techniques, and also to attain difficult, complicated structures that require spacings smaller than that attainable by EBL.

3.2 Nanosphere lithography

In the first case, we have shown the polyolefin heat shrink film as an employable substrate for bottom up nanolithography by using nanosphere lithography. In nanosphere lithography (NSL), spheres of diameters of 500 nm to several µm are deposited onto a surface in a colloidal suspension. Evaporation of the solvent causes the spheres to hexagonally close pack to preserve energy. Beads can also pack in layers, in either ABA stacking, or ABCA stacking. Close packing is controlled by concentration of the solution, sphere size, surface energy of the substrate, and rate of evaporation of the solution. Spheres are typically silica or polystyrene. The forces that pack the spheres are convective and capillary, depending on the method of deposition (dip coating, spin coating, doctor blading, etc.).The beads are then used as a mask, as in traditional photolithography, where the exposed regions of the substrate underneath it are either coated with metal, or etched. The beads can then be removed via sonication in water or ethanol. NSL has been used to generate various patterns, ,among them, using RIE and plasma etching, nanopillars, and, using metal vapor deposition, nano triangles, also known as the bow tie structure. The main limiting factors of NSL lie in the mask itself. 1) Periodicity and nanostructure size cannot be independently tuned. 2) Bead diameters below ~200

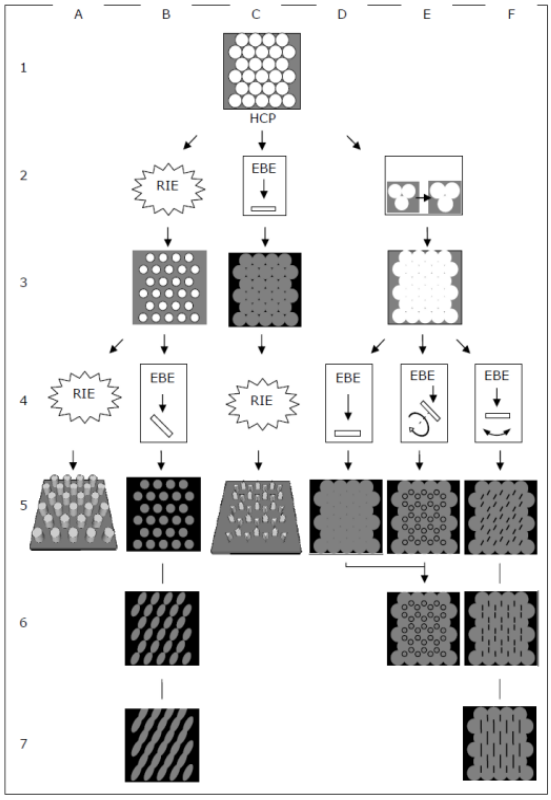

Figure 3.1. Attainable nanostructures using nanolithography. Reprinted with permission from A. Kosiorek ,† W. Kandulski ,† P. Chudzinski ,‡ K. Kempa ,§ and M. Giersig *† "Shadow Nanosphere Lithography," ,Nano Lett. vol. 4, no. 7, pp. 1359-1363,2004. American Chemical Society.

nm are difficult to pack in the HCP structure, due to increased Brownian motion and decreased monodispersity. This severely limits the smallest feature sizes attainable. By applying nanosphere lithography to a plastic PO substrate, we have developed a low cost, robust, high throughput and versatile technique to fabricate arrays of at least two types of nanostructures. This capability of the PO film was first demonstrated by reducing nanopillar arrays by 35%. This capability has thus far been improved by producing nano bowtie arrays, which can be reduced in periodicity by up to 77% and in size by over 33%.

3.3 Tunable nanopillar arrays

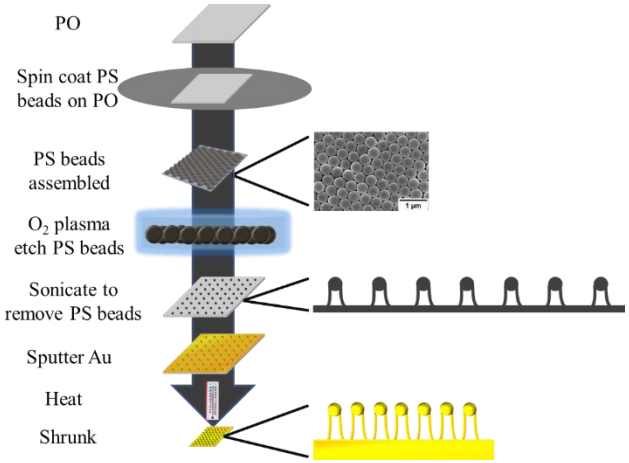

Figure 7. Schematic process flow for fabrication of nano bead pillars.

Reprinted with permission from N. Sharac, H. Sharma, M. Khine, and R. Ragan. "Tunable nano bead arrays on film for controlling propogation of light*," SPIE proceedings*, vol. 8809, 2013.

Nanopillar arrays have shown potential use in solar, anti-reflective coatings, and SERS enhancements. For instance, Caldwell et all, has used e-beam lithography to generate gold nanopillar arrays, with diameters ranging from 320 nm to 120 nm and distances from 270 nm to 60 nm, for a tunable plasmon resonance, with uniform SERS enhancement factors as high as ~1.2x10^8 [77]. Ji et al. has used NSL to generate nanopillars in close resemblance to the cones in a moth's eye, on both sides of glass using NSL, resulting in a 99% transparency in the visible region. By tuning the height and pillar shape, they were able to tune the frequency region in which the AR properties occurred. The AR properties arise from periodic structures smaller than the wavelength of light, which results in a smooth gradient in the refractive index and an effective absence of an air lens interface [78].However, the spacing between pillars, which plays a direct role in the refractive index gradient, remained fixed, due to the inherent inability of NSL to alter periodicity independently of structure height and size. SiC nanopillar arrays, discussed in section 3.6, are a novel type of structure based on exciting localized surface phonon polaritons (SPhP). These modes are as of yet largely unexplored, and therefore a facile way to create tunable pillars would be useful.

In this work, I have produced nanopillar arrays similar to the work done by Park and Caldwell, but with the significant difference of facile tunability. The nanopillars discussed next do not require EBL to alter periodicity, and can be tuned in under an hour. This is useful for experiments that are pitch dependent, such as the moth eye structure. By using nanosphere lithography in conjunction with the PO film, these bead-pillars are reducible in periodicity. Additionally, plasma etching supplies another independent parameter to vary the size of PS and the height of nano bead-pillars. The process is shown in Fig. 3.2. NSL provides a hexagonal closed packed mask of latex beads of

500 nm diameter [79]. Introducing the beads and PO substrate to oxygen plasma allows for tuning of the beads diameter and spacing, in addition to creation of pillar structures from the etched PO. The substrate, consisting of a polyolefin blend, is pre-stressed, and therefore reduces in surface area when exposed to temperatures above 100 °C. This is used to modify the geometry of our pillar array. Overall the spacing, feature size and height of these nano pillars can be tuned independently by thermal processing and plasma etching. Finally, gold can be added to our pillars via physical vapor deposition (PVD).

3.31 Experimental

Polyolefin (PO) films (955-D, Sealed Air Corporation) ,with thickness of approximately 1 millimeter that are laminated on a 3 millimeter polyester backing ,are cleaned in isopropyl alcohol and then dried with pressurized air. The clean PO film is then oxygen plasma treated for 30 s at a power of 60 W to increase the hydrophilicity of PO surfaces. A solution of 500 nm polystyrene (PS) beads (Bangs lab) was diluted to a 3:1 ratio with triton X-100 and methanol (1:400 by volume). Approximately 12 µL of this solution was then spin coated onto the PO film for 5 minutes at 1000 RPM and allowed to dry for two hours. After spin coating, the substrate is plasma etched at a power of 60 W in an Oxygen plasma asher for different times, from 540s to 810 s. Immediately following the plasma etch step, samples are sonicated in ethanol for one

minute and subsequently sonicated in deionized (DI) water for thirty seconds to remove residual etchant material. The samples are then mounted on a glass slide with double sided tape and heated in a convection oven from room temperature to different degrees of temperature ranging from 90 °C to 120 °C. The differences in the length from the original PO size were measured with a digital caliper

during the heating process. The percentages shrunk in length were calculated by taking the ratio of the final width of substrate relative to the initial width. Finally, samples were coated with a 5 nm titanium adhesion layer followed by 50 nm Au, using chemical vapor deposition. Temperatures did not exceed 115° C during this process to avoid further shrinking. An atomic force microscope (AFM) (Asylum Research MFP-3D AFM) with silicon cantilevers (Olympus) was used to characterize the resulting topography of our substrate, and a scanning electron microscope (SEM) (FEI- Magellan 400 XHR), at ~ 2 kv, was used to image the periodicity of features over a large area.

3.32 Results

The oxygen plasma etch time was varied to determine the etch rate of PS beads and the underlying PO. SEM images, after etching, are shown in Figure 3.3 a-d etched for time periods of (a) 540 s, (b) 630 s, (c) 720 s, (d) 810 s, respectively, since plasma etching the PS beads was found to be most effective in this time range. Etching times less than 540 s resulted in minimal etching of PS beads, and beyond 810 s, the pillars were found to be damaged

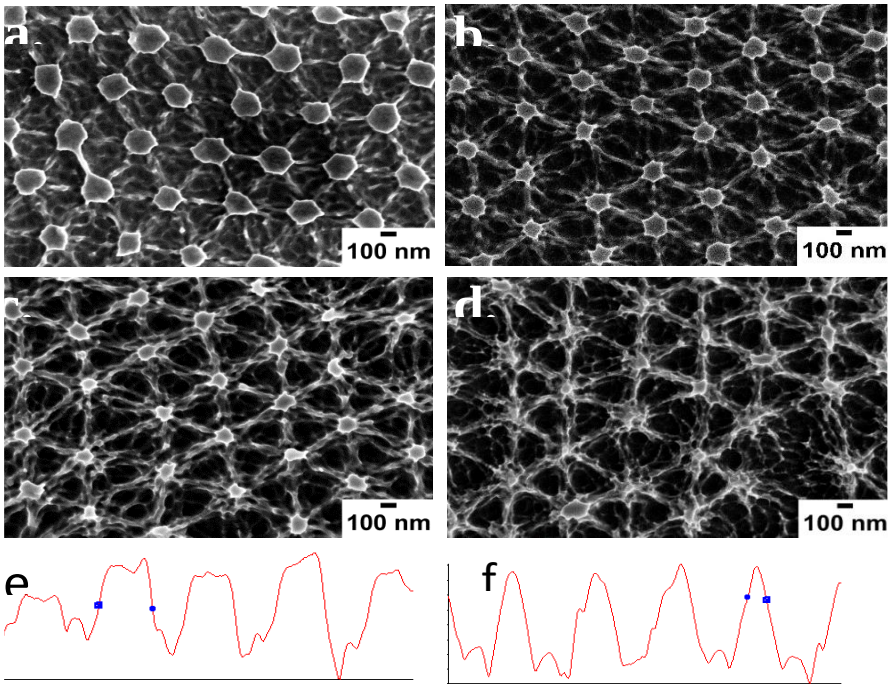

Figure 3.3. SEM images of gold coated 500 nm PS bead arrays that were reduced in size using various plasma etch times: a) 540 s, b) 630 s, c) 730 s, d) 810 s. Scale bar is 100 nm. 2 µm AFM height profiles for samples etched for e) 540 s, and f. 810 s provide the shape of the resulting nanopillar beads.
Reprinted with permission from N. Sharac, H. Sharma, M. Khine, and R. Ragan. "Tunable nano bead arrays on film for controlling propogation of light," *SPIE proceedings*, vol. 8809, 2013.

in SEM images, data not shown. Etching for time periods of 540-810 s led to a deformation of PS beads, as observed in Fig. 3.3 Etch times longer than 810 s led to significant etching of PS beads to the point of obliteration. Fig. 3.3 d, shows the PS beads to be significantly smaller and distorted when compared to Fig. 3.3 a, 2b, and 4c. As expected, as the diameter of nano pillars is reduced due to increasing the etch time, the inter-spacing between the pillars is increased as observed in Figure 23 a-d. As the measured pillar width decreased from approximately 240 nm to 100 nm, when the etch time increased from 540 to 810 s, the edge to edge spacing increased from approximately 250 nm to 400 nm. AFM topography line profiles are shown in Fig. 3.3 e and f, corresponding to etch times of 540s and 810 s, respectively. The height profiles illustrate that with longer etch times, the top point of the pillars becomes sharper relative to the smooth tops observed on pillars after an etch time of 540 s, observed in both in Fig. 3.3 e and f.

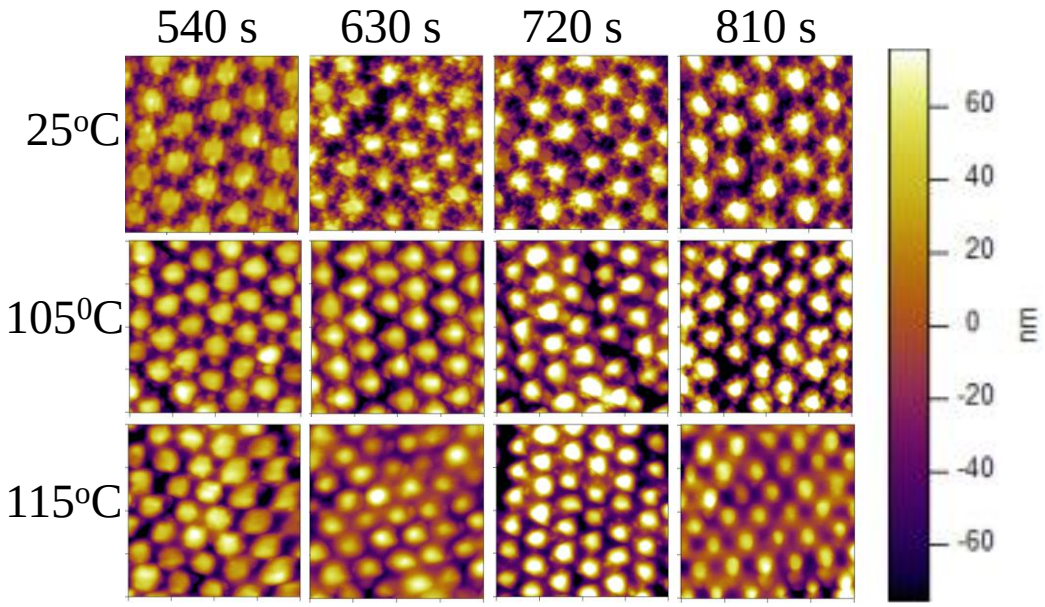

Figure 8. AFM topography images of gold coated PS bead arrays on PO, etched for different time intervals and then shrunk in size from 0% to 20% to 33% by heating them from 25°C to 105°C to 115°C, respectively.

Reprinted with permission from N. Sharac, H. Sharma, M. Khine, and R. Ragan. "Tunable nano bead arrays on film for controlling propogation of light*," SPIE proceedings*, vol. 8809, 2013.

AFM topography images of the etched beads are shown in the first row of Figure 3.4, with a common height scale legend on the right show that heights range from approximately 60 nm for pillars etched for 540 s and up to 160 nm for a plasma etch time of 810 s and that the height increase is monotonic with etch time. Due to the diminished beads after 810s of plasma etching, while the etched PO film was still intact, further deepening of the pillar features on the surface was not possible due to the obliteration of the PS NSL mask. If a higher aspect ratio is needed, RIE can be used, due to the difference in dry etch rates between PO and PS [80, 81]. This is especially important for plasmonic applications where high aspect ratio structures are correlated with strong local electric fields [82] or for anti-reflection applications such as "moth eye" structures, where height has been shown to

play a major role in AR, due to suppression of light reflection. Traditionally, NSL has been performed on Si substrates to generate pillars with heights up to 400 nm by using selective etching methods, such as RIE, with fluorination or chemical etchants. On such a hard surface, the beads do not adhere to the surface and are removed after sonication in a solvent. Using a soft PO film, the PS beads remain bound to the PO film surface. Also, the beads appeared to have a strong adhesion to the PO surface. Sonicating the PS coated PO films in organic solvents such as hexanes and dichloromethane did not lead to release of PS beads. If combined with selective etching, tall, high aspect pillars can be attained with easily shapeable caps.

We also investigated how a combination of etching and thermal processing leads to independent control of feature size and periodicity not obtained in conventional NSL. Fig. 3.4 shows AFM topography images for PS bead arrays on PO, etched for different durations and heated from room temperature to 105° C and 115ºC. Visually, it can be observed in the AFM images that as the substrate is heated, the spacing between nanopillars decreases, with this decrease correlated with the

percentage of decrease in dimensions of the PO substrate. Furthermore, thermal processing also increases the heights of the nano bead pillars by approximately 30 nm when heated to 115°C. Based on the conservation of mass law, since film contracts in the X and Y direction, the film must increase in the Z direction. Approximately 30 nm increase in the height was observed when shrinking to approximately 35% in length for all the etch times. Although the PO film has the ability to contract by up to77% in length by heating to 155ºC, the substrates were only shrunk to approximately 35% in length at T = 115 °C. The limit in thermal processing and achievable reduction in feature size, as has been previously demonstrated, is due to stiffening of the PO surface during etching. With the addition of the thin oxide layer attained during plasma etching and metal deposition, shrinking the PO film past 35% in length forced wrinkles to form. This was clearly evident in the SEM and AFM images where the bead pillar arrays became masked by the wrinkles or the features were not all in one plane. A summary of the differences in the widths, heights, and distances measured for the substrates is presented in Table 3.1. For a more quantitative analysis, the same values are also plotted as a function of etch time shown in Fig. 3.5. It is important to note that the spacings reported were measured from center to center, and therefore no decrease in distance as a function of etch time is shown here.

tch time (s)	**Shrink Temp (^{o}C)**	**idth (nm)**	**Spacing in x (nm)**	**Spacing in y (nm)**	**Height (nm)**
540	25	237 ± 6	452 ± 11	448 ± 10	65 ± 4
540	105	224 ± 5	366 ± 10	384 10	79 ± 3
540	115	215 ± 14	314 ± 9	375 ± 15	85 ± 4
630	25	123 ± 7	451 ± 14	429 ± 19	100 ± 6
630	105	118 ± 7	381. ± 4	376 ± 5	120 ± 7

630	115	119 ± 9	314 ± 4	351 ± 6	125 ± 4
720	25	128 ± 8	438 ± 12	445 ± 10	97 ± 5
720	105	128 ± 4	381 ± 9	380 ± 10	105 ± 6
720	115	126 ± 2	343 ± 10	294 ± 9	113 ± 4
810	25	95 ± 7	439 ± 11	452 ± 9	124 ± 5
810	105	97 ± 5	386 ± 7	356 ± 6	132 ± 4
810	115	92 ± 7	320 ± 11	330 ± 8	143 ± 6

Table 3.1**.** Gap spacing, height, and width dimensions of PS bead arrays for different etch times and shrink temperatures.
Reprinted with permission from N. Sharac, H. Sharma, M. Khine, and R. Ragan. "Tunable nano bead arrays on film for controlling propogation of light*," SPIE proceedings*, vol. 8809, 2013.

As presented in Table 3.1 and illustrated in Fig. 3.5, the nanopillars do not vary much in width after heating. In theory, shrinking the substrates should result in smaller diameter of the pillars. This may be related to the PO being segmented into small areas when etched into pillars, preventing the normal shrinking expected. As shown in Fig. 3.5, only the largest measured pillars appear to shrink to a small extent with increase in temperature. This may be due to the segmented PO still being large enough to decrease in surface area to some small extent. As expected, the center to center spacings decreased as a function of heat, as shown in table 3.1 and Fig. 3.5, from approximately 450 to 300 nm, which is approximately a 35% reduction in distance. This reduction in spacing corresponds well to the measured reduction in the length of our plastic substrates. Fig. 3.5 also shows some variation exists in shrinking in the x and y directions of the substrate, which can be attributed to asymmetric stretching of the substrate. Achieving control over this asymmetry is possible by constraining the sample in one direction while heating. The constrained side can be alternated according to desired shrink percentage and desired level of asymmetry. Control of the

asymmetry will allow more tunability in nanostructure arrays in addition to keeping the periodicity consistent. An interesting observation to note is that the samples etched for 810 s showed a continual decrease in the variation of periodicity for the x and y directions as heat was increased.

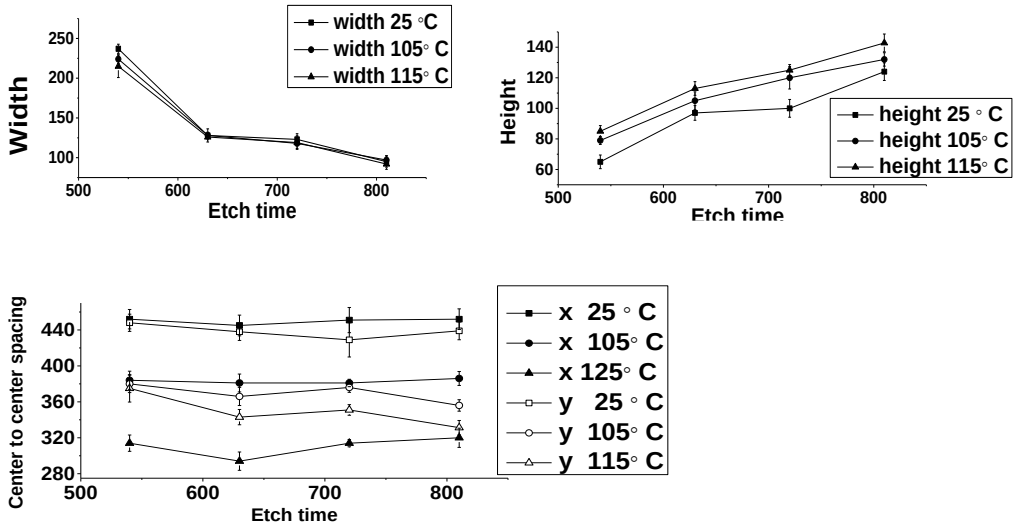

Figure 9. Spacing, width, and heights for PS bead arrays shown as a function of etch time and shrink temperatures.
Reprinted with permission from N. Sharac, H. Sharma, M. Khine, and R. Ragan. "Tunable nano bead arrays on film for controlling propogation of light*," SPIE proceedings*, vol. 8809, 2013.

3.33 Summary

In summary, I have developed a versatile method for quick, robust, and inexpensive fabrication of nanopillar structures. The thermoplastic PO substrate allows for facile tunability of inter particle spacing and height of the structures. Thermoplastics, combined with etching, provides a quick solution to achieve wide range of pillar widths and interpillar spacings. Most significantly, I have achieved independent parameterization of both pillar width and interpillar spacing. Currently, wrinkling prevents the substrates from shrinking past 35%, but this may be circumvented by first

removing the oxide layer or by using a different heat film. Other etch methods, such as RIE, will be used in the future to create a deeper etch, resulting in taller pillars more suitable to AR properties. High aspect ratios in conjunction with increased height from shrinking, change in shape, and controlled variability in spacing should allow for the extensive study of AR properties in moth wing structures. It is also possible that this technique can be combined on other materials, for instance a thin film of SiC deposited on PO, and that the tunability of this structure can be used to explore other phenomena, such as localized SphP modes, described in the next section.

3.34 Silicon carbide nanostructures

Surface phonons are analogous to surface plasmons in their ability to couple with light in the infrared, to create surface phonon polaritons (SPhPs), and also to become localized at the nanostructure [83, 84]. Localized optical phonons show some properties similar to localized plasmons, in that they can be observed as surface vibrations of a lattice at a specific frequency. Optical phonons occur between atoms of different mass and charge, such as silicon and carbon in silicon carbide, and are excited in the mid-infrared to gigahertz spectral region. Like plasmons, these lattice resonances can potentially be tuned to respond at different frequencies in the infrared, based on structure and material. Surface optical phonons have picoscale lifetimes, which are orders of magnitude higher than the scattering times for free carriers supporting plasmon modes in metals and doped semiconductors. Therefore, SPhP materials have a strong potential for low loss nanophotonic devices, in addition to sensing devices that work in the mid to far-IR range. This is significant, considering the high losses suffered in plasmonic metals, as mentioned in chapter 1. Typical SPhP materials include SiC, III-Ns, III-Vs, and SiO2 [85-88].

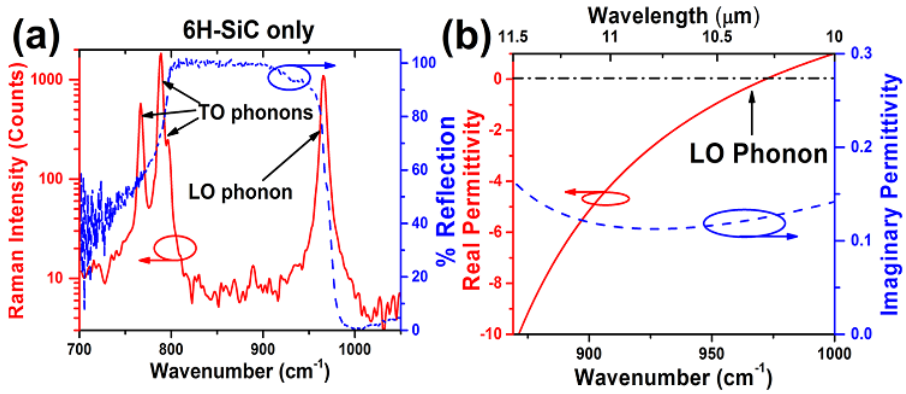

Figure 3.6. (a) Micro-Raman (red solid line) and FTIR reflection (blue dashed line) spectra of a 300 um 6H−SiC substrate, showing the LO and TO phonon modes within the reflective Restrahlen band. (b) The real and imaginary parts of the permittivity, determined from fitting of the reflection spectra of the 6H−SiC substrate, which was used for nanopillar fabrication. The spectral range provided coincides with that of the position of the LO phonon and the observed localized SPhP modes presented in this work. The horizontal dashed/dotted line shows where the real permittivity is equal to zero.

Reprinted with permission from J.D. Caldwell, O. J. Glembocki, Y. Francescato, N. Sharac, V. Giannini, F. J. Bezares, J. P. Long, J. C. Owrutsky, I. Vurgaftman, J. G. Tischler, Vi. D. Wheeler, N. D. Bassim, L. M. Shirey, R. Kasica, and S.A. Maier, "Low-Loss, Extreme Subdiffraction Photon Confinement via Silicon Carbide Localized Surface Phonon Polariton Resonators," Nano Letters, vol. 13,no.8,pp. 3690-369, 2013. American Chemical Society.

Between the transverse(TO) and longitudinal (LO) optical phonon modes, where the permittivity is negative, the coherent oscillations of the charged lattice can result in screening of incident light and a spectral region of high reflectance referred to as the Restrahlen band. Shown in Fig. 3.6 a) are the TO and LO phonon modes revealed by Raman scattering, in red, and the Restrahlen band, in blue, shown from IR reflectance, taken on a 6H-SiC substrate [89]. Fig. 3.6 b) shows the real and imaginary permittivity of SiC at the same frequencies, taken from fitting of the reflectance spectra of 6H-SiC. The real permittivity becomes negative at the LO phonon mode, and increases in negativity for decreasing energy until reaching a minimum at the TO mode. Within this region, the reflectance of 6H-SiC becomes increasingly close to 100%, demonstrating behavior of a metal. It is in this region that SiC and other dielectric nanostructures can support tunable, localized SPhP

modes. Significantly, the small imaginary part of the permittivity in Fig. 3.6 b) shows that losses are small in this region.

Previously, little work has been done to fabricate localized SPhP resonators- in the past, methods such as reactive ion etching (RIE) resulted in damping of the phonon mode response [90]. Here, we report localized SPhP resonators with defined resonate responses. To induce localized SPhP resonant modes, 800 nm tall SiC nanopillar arrays were fabricated with diameters ranging from 150 nm to 260 nm. We then measured FTIR reflectance of the substrates to determine SPhP modes and SphP mode changes as a function of pillar diameter and pitch, in addition to performing some micro Raman measurements on the substrates. These measurements help show the potential of SiC as a low loss alternative to traditional plasmonics.

3.3.5 Experimental

6H-Silicon carbide substrates about 350 um thick were used. An Al/Cr hard mask, defined by standard electron beam lithography, physical vapor deposition (PVD), and liftoff, was used as an etch mask. Nanopillars were fabricated using reactive ion etching (RIE) of equal parts pressure, SF6 and Ar, at 150 W power at room temperature for a duration of 38 minutes. The Al/Cr mask was then removed with wet chemical etchants, followed by a hydrogen atmosphere etch in the growth cell of an Aixtron VP508 growth reactor at 1400° C for 3 minutes, to remove any surface damage induced by the RIE process and to remove any fluorine contaminants. Micro Raman and FTIR spectroscopy were both used to characterize the SPhP resonances of the 6H-SiC nanopillar substrates, of varying diameters and interpillar gaps. Mid-IR reflectance spectra were measured using a Thermo Scientific, Nicolet FTIR continuum Microscope with a 15x, 0.58 NA objective,

which illuminates the sample at incident angles between 10-35° off normal, and has a weighted average of 25°, which enabled excitation of both transverse dipolar and monopolar modes of the nanopillars. All spectra were collected at 128 averaged scans and .5 cm^{-1} resolution, with a spatial area of 50x50 um, defined by the internal aperture. An initial background reflection spectrum from a gold film, averaged at 1024 scans, was collected at the same spectral resolution to improve signal to noise. Micro-Raman spectroscopy was performed using a Thermo Scientific DXR Raman Microscope with a 532 nm excitation at 10mW with a 100X .9 NA objective, in confocal mode. The integration time was 5s. 3D Electrodynamic calculations were also performed, using the RF module in the finite-element package of COMSOL. Ellipsometry and reflectance data from the 6H-SiC nanopillar samples were used to determine optical constants, and SEM images were used for geometric dimensions. An incident optical field at 25° was used in the simulations to match that of the FTIR microscope.

3.3.6 Results

Shown in Fig. 3.7 is the IR reflection spectrum for 6H-SiC (green), and 6H-SiC (red) periodic arrays of nanopillars with 250 nm diameter, 800 nm height, and 150 nanopillar gaps. Two SPhP modes are shown at around 910 and 930 cm^{-1}, which are similar to ones observed by Urzomohov et al. [91] from 3C-SiC transmission gratings, with 1-2 um diameter holes. There are an additional two peaks at 882 and 888 cm^{-1}, which are attributed to the splitting of a doubly degenerate bulk phonon. The blue line shows calculated reflectance spectrum using COMSOL Multiphysics software, which is in close agreement to the experimental.

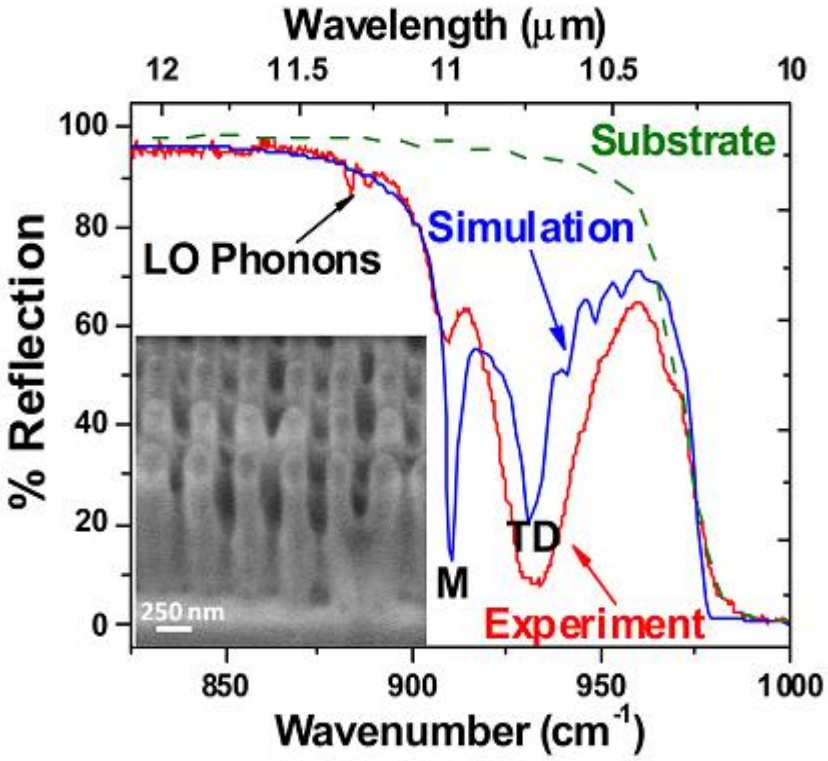

Figure 10. FTIR reflectance spectrum of a periodic array of 800 nm tall, 250 nm diameter, 6H−SiC nanopillars (red solid line) on a 400 nm pitch compared to a simulated (blue solid line) spectrum from COMSOL).“M” and “TD” denote the spectral positions of the monopole and transverse dipole resonances, respectively. The reflection spectrum of the surrounding 6H−SiC substrate (dashed green line) is provided for comparison. An SEM image collected at 45° is shown in the inset.

Reprinted with permission from J.D. Caldwell, O. J. Glembocki, Y. Francescato, N. Sharac, V. Giannini, F. J. Bezares, J. P. Long, J. C. Owrutsky, I. Vurgaftman, J. G. Tischler, Vi. D. Wheeler, N. D. Bassim, L. M. Shirey, R. Kasica, and S.A. Maier, “Low-Loss, Extreme Subdiffraction Photon Confinement via Silicon Carbide Localized Surface Phonon Polariton Resonators,” *Nano Letters*, vol. 13,no.8,pp. 3690-369, 2013. American Chemical Society.

The two modes in the blue line, “M”, and “TD,” are identified as monopolar and transverse dipolar modes, respectively. The IR-reflectance peak at about 930 cm^{-1} was shown to vary with change in pillar diameter, but was only weakly dependent on angle change and on change in inter pillar gap. The calculated cross sectional and top view electromagnetic field profiles for the 6H-SiC nanopillars coincide with this observation (Fig. 3.8 a,c), as most of the mode resides in the actual

pillar. This mode was shown to be a transverse dipolar mode. This is not the case for the lower energy resonance at around 920 in Fig. 3.7, depicted as "M," for monopolar, which showed a large dependence on pillar diameter and gap for the IR-reflectance spectra taken. The intensity also increased at larger incident angles. The interpillar gap dependence suggests interpillar coupling. From modeling, it was found that this mode could only be excited from off normal incidence, which suggests it is longitudinal. As shown in Fig. 3.8 b, the SPhP mode resides within the pillar gaps, around the base of the pillar, which would account for the large pillar gap dependence. In Fig. 3.8 d, the plan-view electromagnetic profile E_z/E_o calculated for a plane just below the surface suggests that this longitudinal mode is a lower order monopolar resonance. Although the monopolar resonance is not excitable in isolated pillar cases, charge neutrality in this case is achieved by an opposing field near the substrate surface between the nanopillars. Recently, monopolar resonances have been reported in plasmonic nanorods with metal ground planes.

The calculated spatial profiles for the transverse dipolar and monopolar SPhP modes indicate deep subwavelength field confinements, $(\lambda_{res}{}^{3} / V_{eff})^{1/3}$ of 115 and 199, respectively, within an array of 250 nm diameter nanopillars on a 400 nm pitch. λ_{res} is the resonant wavelength and V_{eff} is the modal volume. As shown in Fig.3.8 a,b) the logarithm plots reveal enhancements exceeding well over 5000x, with most of the enhanced field being limited to the surface of the nanostructure, and little of it being inside. The quality factor, Q, defined here as

$$Q = \frac{\omega_{\text{resonant}}}{\omega_{\text{resonant}}^{\text{fwhm}}}$$

or as the resonant frequency divided by the line width of the resonant frequency, was derived experimentally for both monopolar and transverse dipolar resonances, using reflectance spectra

from the 6H-SiC nanopillar substrates of varying diameters, and were found to vary from 40 to 50 for the transverse and from 70 to 135 for the monopolar resonances. These values well exceed those reported for single silver nanoparticles, which showed a theoretical maximum limit of ~40. The high Q factors reported here were expected considering the low losses predicted in Fig. 3.6 for 6H-SiC nanopillar arrays.

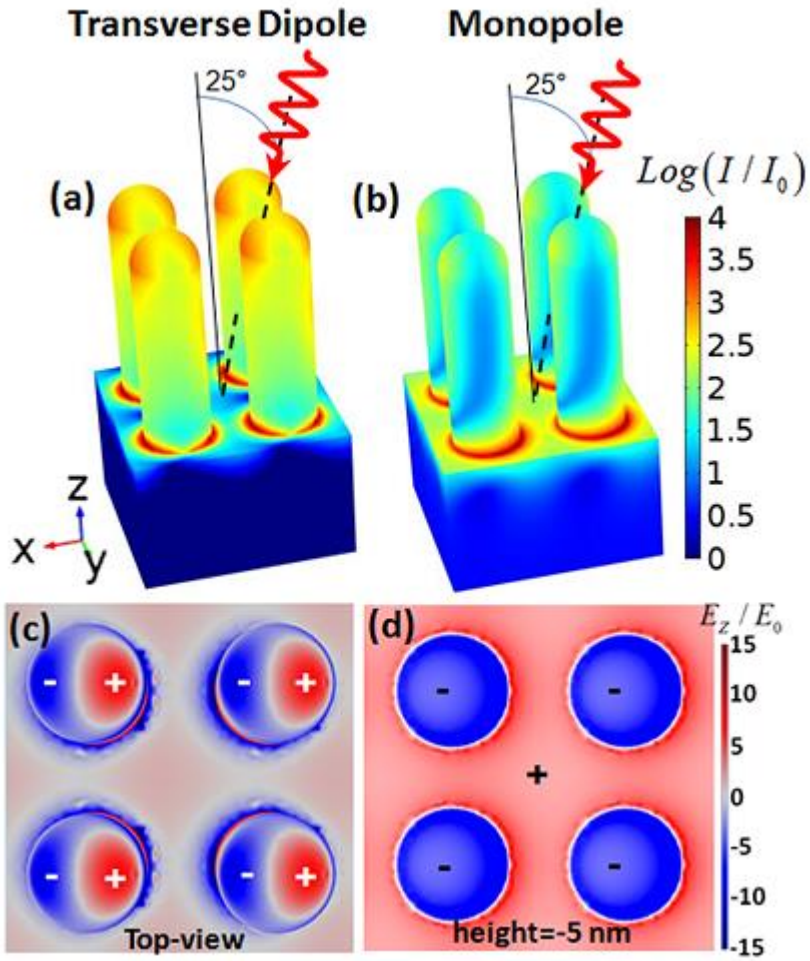

Figure 11. Calculated electromagnetic intensity profiles, log (I/I0), are shown for (a) transverse dipolar and (b) monopolar modes. The angle of incidence of the plane wave used for calculations is at 25°, as depicted. (c) shows the he respective top-view electromagnetic field profile (E_z/E_0), of the transverse dipolar mode and (d) shows the plan-view profile of the monopolar mode, at 5 nm below the substrate surface, which was used to avoid interface effects and to clearly depict the role of the substrate) .

Reprinted with permission from J.D. Caldwell, O. J. Glembocki, Y. Francescato, N. Sharac, V. Giannini, F. J. Bezares, J. P. Long, J. C. Owrutsky, I. Vurgaftman, J. G. Tischler, Vi. D. Wheeler, N. D. Bassim, L. M. Shirey, R. Kasica, and S.A. Maier, "Low-Loss, Extreme Subdiffraction Photon

Confinement via Silicon Carbide Localized Surface Phonon Polariton Resonators," *Nano Letters*, vol. 13,no.8,pp. 3690-369, 2013. American Chemical Society.

As with its localized plasmon analogue, modifying the diameter of the 6H-SiC nanopillars was shown to modify the resonance frequency, while keeping a near constant line width. There was about a 4% variation in line width for the TD mode for nanopillar arrays with diameters ranging from 150 nm to 260 nm with a constant nanopillar gap of 150 nm. The lack of variation in line width is most likely from low susceptibility to boundary scattering, due to the short mean free path of the optical phonons, as they have a low group velocity. This is contrary to plasmonic systems which show high susceptibility to boundary scattering losses. Fig. 3.9 a) shows the experimental FTIR reflectance shifts in localized SPhP resonances, with varying diameter. Fig.3.9 b) shows the experimental (closed) and calculated (open) spectral positions of the TD and M modes as a function of diameter. From both the calculated and experimental plots in b), it can be seen that as the nanopillar diameter decreases, the transverse dipolar mode increases in energy, whereas the monopolar mode decreases in energy, where a dramatic shift is seen starting at around a 200 nm diameter. Whereas the TD experimental and calculational curves match to a fairly high degree, there is some discrepancy between the calculational and experimental lines for the monopolar mode, starting at around 878 to 892 cm^{-1}, as shown in the cross hatched region in Fig. 3.9b). It is believed that once the monopolar mode is tuned to around this energy, it begins to interfere with the two split LO phonon lines referred to in Fig. 3.6, resulting in a broadening and asymmetry in the line shape of the monopolar mode, as experimentally observed in the FTIR and demonstrate in 15 a) by the purple arrow. This effect resembles a Fano resonance, where the monopolar mode serves as a broader mode (continuum of states) for the two discrete LO phonon modes.

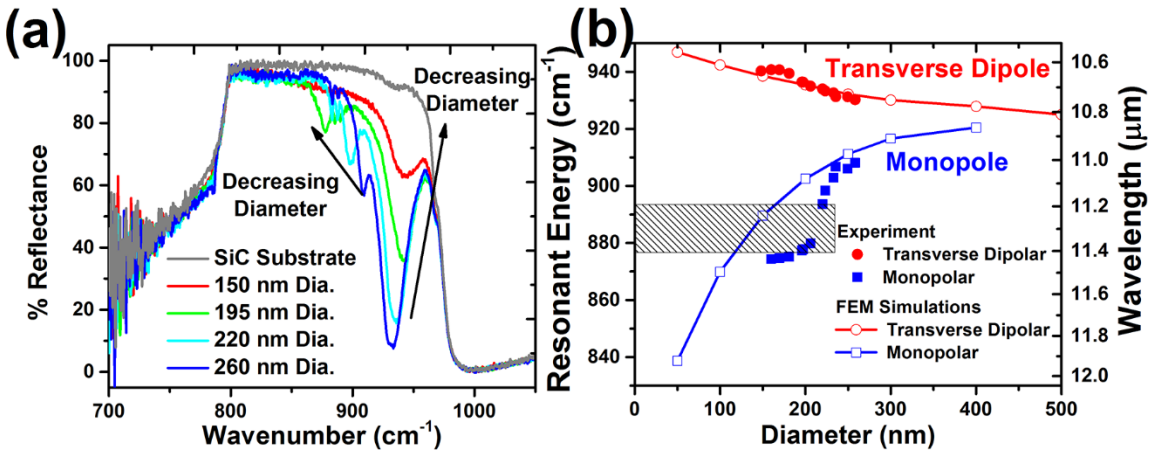

Figure 12. (a) FTIR reflection spectra of 800 nm tall, 6H−SiC nanopillars as a function of pillar diameter, in addition to the unpatterned substrate (grey). The arrows show peak shift directions for the two modes with decreasing diameter, in addition to the emerging fano resonance of the downshifting monopolar mode. (b) shows the peak positions for the two modes (red circles and blue squares) as a function of diameter, in addition to calculated values from COMSOL (open symbols, with lines as a guide to the eye). The cross-hatched area marks the spectral region where the monopolar resonance interferes with the LO bulk phonons.

Reprinted with permission from J.D. Caldwell, O. J. Glembocki, Y. Francescato, N. Sharac, V. Giannini, F. J. Bezares, J. P. Long, J. C. Owrutsky, I. Vurgaftman, J. G. Tischler, Vi. D. Wheeler, N. D. Bassim, L. M. Shirey, R. Kasica, and S.A. Maier, "Low-Loss, Extreme Subdiffraction Photon Confinement via Silicon Carbide Localized Surface Phonon Polariton Resonators," *Nano Letters*, vol. 13,no.8,pp. 3690-369, 2013. American Chemical Society.

Fig. 3.10shows Raman spectra from 6H-SiC nanopillar arrays, using a 532 nm excitation (red), in addition to the FTIR reflectance spectra (blue) for a 200 nm diameter nanopillar array with 800 nm height and 350 nm pitch. In many cases, both the monopolar and transverse dipolar modes were found to be Raman active, as the two Raman peaks correlate clearly with the observed FTIR reflectance counterparts. For all arrays measured, the Raman spectra showed a broad surface optical mode centered around 934 cm^{-1}. Both the TD and M localized modes were observed when they resided close to the aforementioned peak, and either decreased in intensity or became

unobservable as they shifted away, which suggests that the LSPhP modes are resonantly enhanced by the surface optical mode. Since in most cases the TD mode overlapped with the 934 cm^{-1}mode, it is unclear whether this optical mode is observable in the FTIR, however, Fig. 3.9 does show a slight dip in the FTIR reflectance spectrum for a 6H-SiC thin film at 934 cm^{-1}, which may be due to an optical surface mode at the SiC/air interface.

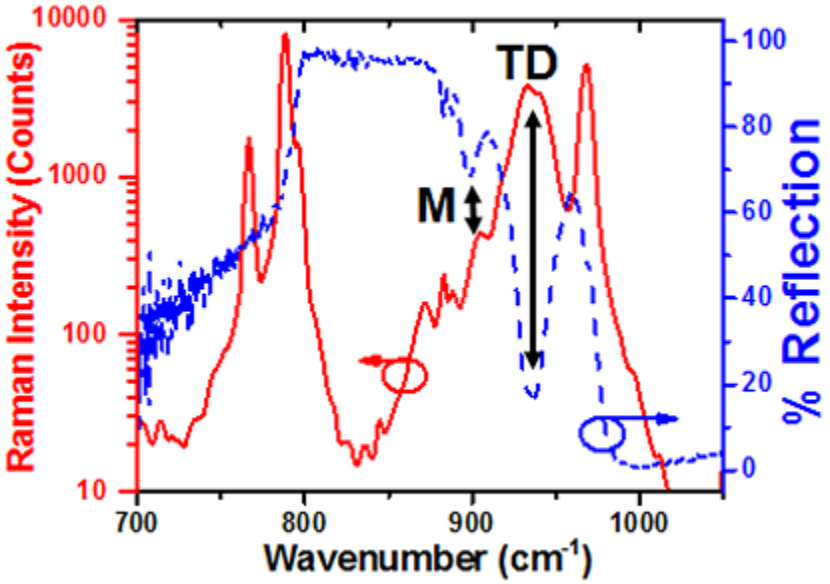

Figure 3.10 Micro-Raman (red solid line) and FTIR reflection (blue dashed line) spectra from a periodic array of 6H−SiC nanopillars of 200nm diameter, 800 nm height, with a 350 nm pitch. The double-headed arrows correspond to the positions of the two labeled SPhP resonances [46].

Reprinted with permission from J.D. Caldwell, O. J. Glembocki, Y. Francescato, N. Sharac, V. Giannini, F. J. Bezares, J. P. Long, J. C. Owrutsky, I. Vurgaftman, J. G. Tischler, Vi. D. Wheeler, N. D. Bassim, L. M. Shirey, R. Kasica, and S.A. Maier, "Low-Loss, Extreme Subdiffraction Photon Confinement via Silicon Carbide Localized Surface Phonon Polariton Resonators," *Nano Letters*, vol. 13,no.8,pp. 3690-369, 2013. American Chemical Society.

3.3.7 Summary

Using RIE and a Cr etch mask, 6H-SiC cylindrical nanopillar arrays, with 800 nm pillar height and diameters, ranging from 150 to 260 nm, were successfully fabricated. Despite earlier predicted high signal losses, strong SPhP responses in both FTIR reflectance and Raman spectroscopy were measured. Structuring the SiC surface into nanopillar arrays induced two localized SPhP modes, the transverse dipolar and the monopolar modes, the latter of which is believed to be a modified response of the longitudinal dipolar mode, due to the underlying SiC substrate. As expected from localized modes, which are analogous to localized surface plasmon modes, tuning the pillar diameter, and in some cases interpillar gap of the 6H-SiC nanopillar arrays, shifted the SPhP resonance of the TD and M modes. This shows that, as with plasmonics, SPhP modes can be potentially tuned based on shape, periodicity, and dielectric material of the nanostructures. These SPhP modes are low loss with narrow line widths, with Q factors ranging from 40 to 135. This, combined with localization of these modes, presents nanostructured polar dielectric materials as a potential low loss alternative to plasmonics for nanophotonic and metamaterial devices. The calculated enhancements exceeding 5000x, in addition to the wide spectral position of the Restrahlen band, allow for significant enhancements in molecular sensing in the IR range. Additionally, the interaction of these localized phonon modes with discrete surface SPhP modes can lead to Fano resonances, which have potential use in sensing [92]. The induced monopole and transverse dipolar modes were also found to be Raman active, allowing for complimentary approach to traditional SERS. The calculated light confinements for the localized SPhP modes varied from 50 to 200, indicating extreme sub diffraction light confinements. This is partially a result of the long wavelengths in the IR range, and indicate the potential for electromagnetic field coupling at larger spacings than for traditional plasmonics. Such spacings are likely attainable using the nanopillar methodology described in section 3.2.

3.4 Bow tie structure

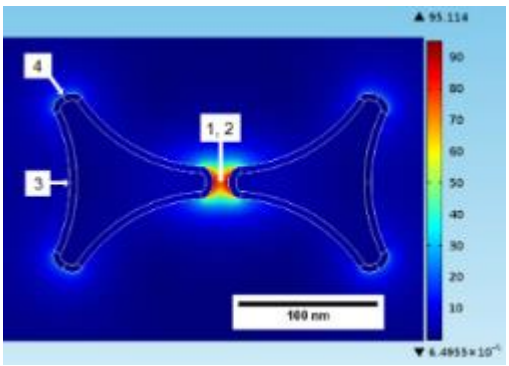

Figure 13. Elecric field enhancement calculations for a single silver bowtie structure with triangles with tip to edge length of 100 nm and tip to tip spacing of 12 nm. [96]

Nanotriangles, also known as bowtie structure, are a common bottom up assembly pattern achieved by nanosphere lithography, which are fabricated by depositing metal through the interstices of the polystyrene sphere mask on the substrate, followed by mask lift off. Previous work has shown hot spots to exist between the junction of two such Ag nanotriangles, with reported SERS enhancement factors over 10^7 [93-95] for Ag triangles, with 200 nm base length and 55 nm thickness. In this case, he used a tunable laser to match the incident and Raman scattered photons with the LSPR mode. The hot spots were reportedly from the triangle tips, due to the so called "lightning rod effect," and plasmonic coupling, as shown in the simulation above in fig 3.11[96]. Since the nanotriangles are a direct result of the metal deposited within the nanosphere spacings, the size of the triangles are directly dependent on the size of the latex spheres, where NSL is limited to HCP packing of 200 nm spheres at the smallest. This implies a limit on the size of the triangle, periodicity, and density, and as a result, the strength of the confined field. A thermoplastic substrate can bypass this limit. Here, I have reproduced similar nanotriangle arrays, using gold, with the added benefit of the polyolefin thermoplastic substrate. Unlike the aforementioned nanopillars, the nanotriangle design requires minimal oxygen plasma etching, minimizing the oxide layer and

allowing for further size reduction of our polymer without wrinkles. The PO substrate enables the reduction of the tip to tip spacing by 77%, which enables the future possibility of plasmon coupling, as tip to tip spacings are shown in some cases as small as 1 nm. Furthermore, the reduction of the bowtie array size has been shown to blue shift the plasmon resonance, which is useful for fluorophore selectivity in metal enhanced fluorescence. The PO substrate allows for tunability of the periodicity, in addition to the size of the triangles. I use reflectance spectrometry and surface enhanced Raman spectroscopy to show controllability of the plasmon resonance with size reduction in our nanotriangle arrays, where heating our arrays gives up to a maximum of 77% reduction in periodicity [97]. Additionally, decreasing the tip-to-tip distance of the nanotriangles gives the potential bonus of increased enhancements within those hot spot regions.

3.41 Experimental

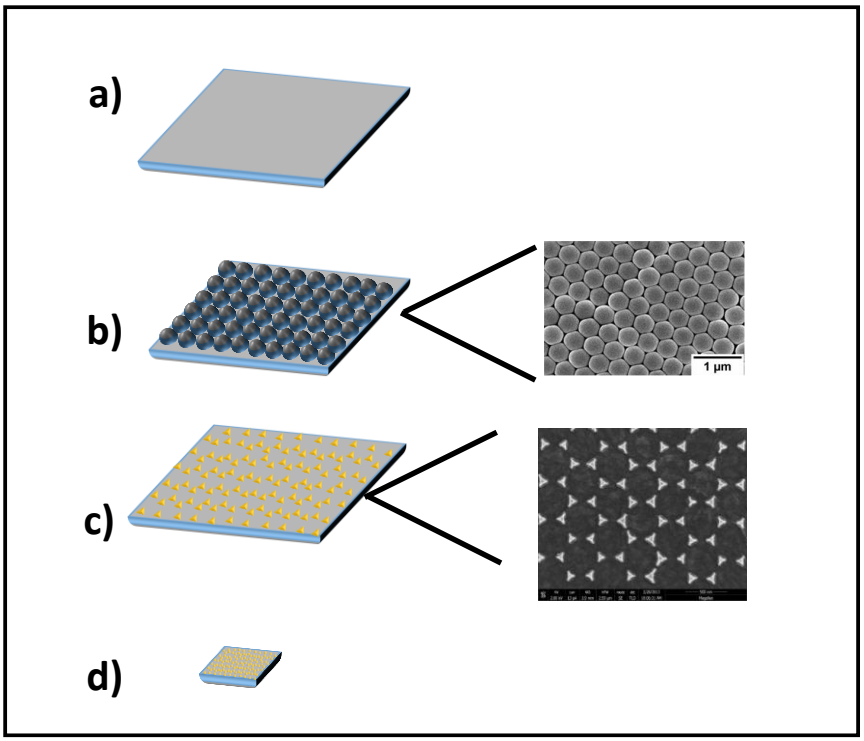

Figure 14. Schematic of nanotriangle fabrication. An oxygen plasma treated polyolefin (PO) film (a) is spun coated with a monolayer of hexagonal closed pack beads (b). The substrate is then

coated with a 40 nm layer of gold using chemical vapor deposition, followed by sonication release beads, yielding an array of nanotriangles (c). The substrate is then placed in a convection oven to reduce substrate and size of the nanotriangle array (d). [97]

A modified nanosphere lithography approach was used to fabricate arrays of gold nanotriangles. Polyolefin (PO) films (955-D, Sealed Air Corporation) ,with thickness of approximately 1 millimeter, were laminated onto a 3 millimeter polyester backing, cleaned in isopropyl alcohol, and then dried with pressurized air. The PO film was then oxygen plasma treated for a period of 30 s at a power of 60 W to increase the hydrophilicity of the surface. A 10.1% solid suspension of 500 nm polystyrene (PS) beads in deionized water (Bangs lab) was diluted to a 3:1 ratio with triton X-100 and methanol (1:400 by volume). Approximately 12 µL of this solution was then spin coated onto PO films for 5 minutes at a speed of 1000 RPM. Samples were then allowed to dry for two hours. Afterward, the samples were etched in an Oxygen plasma asher for 15 s at a power of 60 W. First 3 nm Cr adhesion layer and then a 40 nm Au layer were deposited on the samples using electron beam physical vapor deposition, in a Temescale CV-8 ebeam evaporator, to form triangular features in the interstices, as shown in Fig.3.12 Temperatures did not exceed 115° C during the deposition process to avoid premature shrinking of PO films .The samples were then sonicated in EtOH to release PS beads leaving a metal pattern consisting of triangular features in the regions between the beads. An ice bath was used to avoid deformation of the PO surface during sonication.

Samples were mounted onto glass slides with double sided tape and heated in a convection oven from room temperature to a maximum temperature ranging from 105°C to 135°C. The duration of heating varied at each temperature between 10 and 30 minutes, where the sample was considered to have reduced to its maximum % for that temperature after time periods exceeding 30 minutes. The

PO film was kept fastened to a glass slide, with the polyester backing face down, using double side tape during the heating process to ensure uniform heating and to prevent rapid shrinking. Using digital calipers, the size reduction of the length and width of the shrunken PO films were measured for all samples heated to different temperatures. The percentage reduction in size was calculated by taking the ratio of the final length and width of samples relative to the initial dimension for both dimensions, which was measured from the polyester backing, as it does not shrink in heat. Samples were shrunk from 0% up to 77% in length. In cases where the film shrank asymmetrically, the reduction percentages of both x and y sides were averaged.

Atomic force microscopy (AFM), using an Asylum Research MFP 3D AFM (Santa Barbara, CA) was performed to characterize the resulting topography of samples. 75 kHz resonance frequency probes with diamond-like carbon coating (Budget Sensors-ACST=50) were used for imaging, Scanning electron microscope (SEM) (FEI- Magellan 400 XHR), at ~3 kV, was used to determine the precise change in triangle feature size and periodicity and this measured change in size reduction was compared to the macroscopic size reduction measurements obtained using digital calipers. The nanotriangle arrays, made from nanosphere lithography on a PO film, as described above, were heated at 105°C, 115°C, and 135°C in a convection oven for a period of 10 to 30 minutes.

3. Results

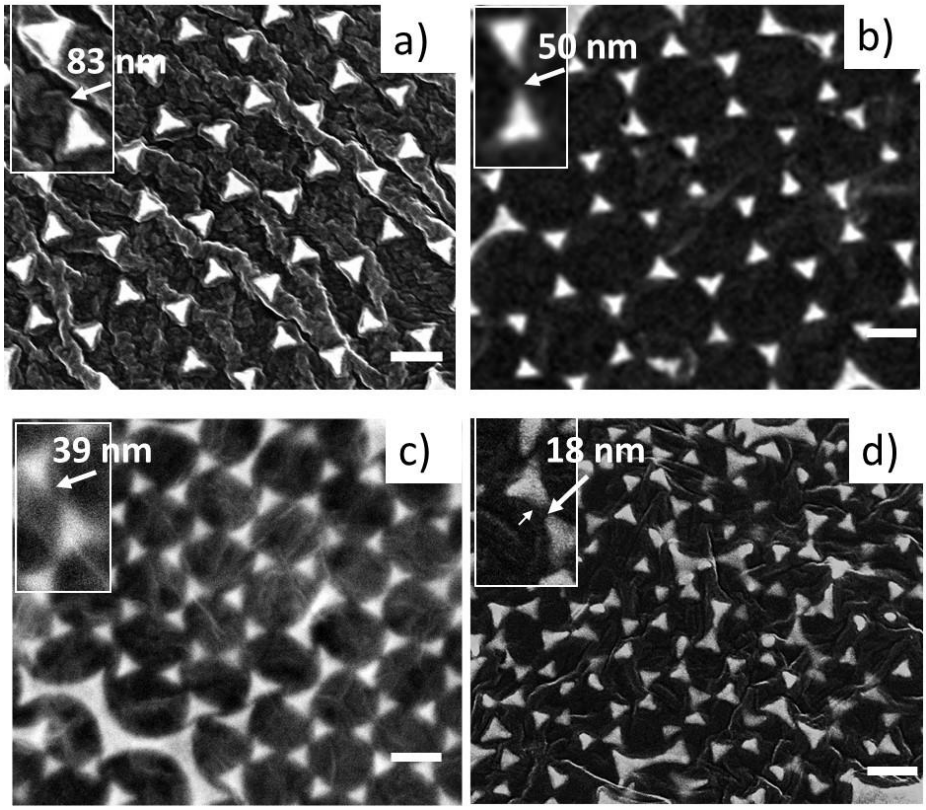

Figure 15. SEM images of nanotriangle arrays on polyolefin film, with average x and y lengths shrunk to 0%, 35%, 52%, and 77% of the original substrate. The percentages shown here are as measured from calipers. In red is the density of gold calculated for each SEM area. The percentages in red show the amount of gold coverage in the area. [97]

The average macroscopic reduction in x and y dimensions for the films heated at 105°C, 115°C, and 135°C, with respect to the unshrunk samples, were 35%, 52%, and 77%, respectively .

Fig.3.13 shows scanning electron microscopy (SEM) images of Au nanotriangle arrays on a) PO film that was not annealed, b) annealed at 105°C, c) annealed at 115°C, and d) annealed at 135°C. Etching the microspheres for 15 s is shown to produce triangles with 90 nm base lengths and 95 nm initial tip to tip distances, as shown in Fig 3.13a). The initial size and periodicity of the triangles can be varied by changing the etch time of the polystyrene nanosphere mask, where longer etch times result in triangles with smaller base to tip lengths and larger tip to tip distances, as shown in supplemental. The arrays of Fig. 3.13 exhibit defects in the periodicity of triangular features. Much of the defects arise from the processing conditions that can be optimized to decrease the number of defects. Defects both in HCP sphere arrangement, during spin coating, and metal lift off, during NSL mask removal, are the main sources of imperfections observed in the SEM images of Fig. 3.13. Due to slight localized variations in the plasma etch rate and metal deposition rate, the unshrunk tip to tip distances and triangle base lengths both vary by ± 14 nm, respectively.

Processing Temperature	Triangle Length	Triangle area (% Reduction)	Tip-to-Tip spacing (% Reduction)	Area Reduction of PO film
25 °C	90 ± 14 nm	3507 nm^2 (N/A)	85 ± 14 nm (N/A)	N/A
105 °C	85 ± 14 nm	3129 nm^2 (11%)	55 ± 17 nm (34%)	35%

115 °C	77 ± 16 nm	2567 nm^2 (27%)	37 ± 14 nm (56%)	52%
135 °C	60 ± 8 nm	1558 nm^2 (56%)	21 ± 10 nm (75%)	77%

Table 3.2 Triangle length, area, tip to tip spacing, and macroscopic area reduction are given for four different processing temperatures. [97]

From calculations using the SEM images of Figure 3.13 the density of Au triangles were found to increase with increased annealing temperature, while the average inter tip distance and triangle base length was found to decrease. When reducing in size from unshrunk to about 35% (Fig. 3.13b), the triangles reduce in average base length from 90 nm ± 14 to 85 nm ±14, while the average tip to tip distance reduces from 85 nm ±14to 55 ± 17 nm. From 35% to 52%, the average base length reduces to 77nm ± 16 while the intertip distance reduces to 37 ±16 nm. Finally, from 50% to 77%, the average base length reduces to 60 ±8 nm, while the average tip to tip distance reduces down to 21 nm± 10. This is summarized in table 3. Dividing the initial average tip to tip spacing by the final shows a ~75% decrease, which matches closely with the macroscopic 77% measurement. However, the decrease in actual triangle size based on base length, which was not initially predicted, shows about a 35% reduction after 77% reduction of the macroscopic film, which suggests the shrinking mechanisms of the actual triangles and the periodicity of the triangles are different. It's possible that metal coated PO areas are under tension that leads to differences in size reduction between periodicity and triangle size. It should be noted that the shrinking of the triangular structures does not change the shape of the structure. Once fully reduced, the PO film shows large areas of wrinkling, as shown in Fig.3.14, however, nanotriangle areas bigger than 10x10um remain intact for future analysis. This is in contrast to the nanopillars, which were only shrunk up to about 35%, due to excessive wrinkling, when reduced further. This is potentially due to the long oxygen plasma

etching used to make the nanopillars, which would result in a larger oxide layer on the film. It also is worth noting that once it reaches a 77% size reduction, the inter tip distances vary from region to region and no longer have the periodicity of the unannealed sample; some tip to tip distances reach about 1 nm. At extreme size reductions the PO film does not shrink uniformly, potentially yielding localized regions where the film shrinks more than the macroscopic measured amount. It is well known that such narrow gap spacings between metallic nanostructures lead to high localized electric fields that are useful for sensing.

Reflectance spectra were taken of each sample using a CRAIC micro spectrophotometer 20/20 PV with 100X objective. A background reflectance spectrum was taken using a gold coated PO film. Fig35 b shows reflectance spectra for the 0%, 35%, 52%, and 77% reduced arrays, as measured using a CRAIC reflectance spectrometer. Note that the data is normalized with a background subtraction from a spectrum obtained from a gold, non-patterned region on the PO substrate to eliminate spectral features resulting from bulk Au. The reflectance spectra shows broad peaks associated with the plasmon resonance of the Au nanostructures for the 52% and 77% reduced structures [98]. Increased variations of the size

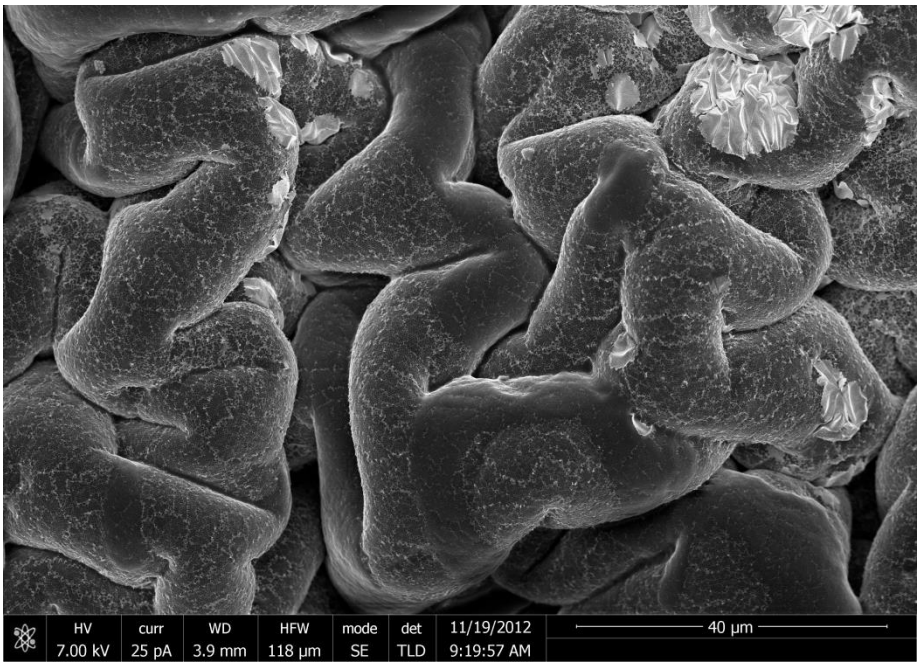

Figure 16. Large view SEM of 77% shrunk nanotriangle arrays.

and periodicity of the Au triangles lead to peak broadening. The peaks shift to lower wavelength with higher percentage of size reduction exhibiting a 100 nm blue shift between the unannealed sample and that annealed at 135° C, which is expected due to decreasing particle size [99].The peak maxima, λ_{max}, shifts from approximately 811 nm, to 777 nm, to 736 nm, to 712 nm, respectively, for the 0%, 35%, 52%, and 77% reduced arrays. To validate this shift, Comsol simulations were also conducted by modeling four cases of bowtie arrays based on the dimensions taken from SEM and shown in the chart above. As shown in figure 3.15 A, the simulations show 111.5 nm blue shift from Case A to Case B, which is very close to the blue shift viewed experimentally. It should be noted that the reflectance spectra from simulation are offset by about 100 nm. This disagreement may in part be potentially explained by the permittivity used for the PO film, which is a polyethylene blend, and does not have an exact literature permittivity. Instead, a permittivity based on polyolefin was used. Despite the offset in plasmon resonance, the closeness in magnitude of the in experimental and calculated blueshift is significant. It should also be noted that the simulation was based on a 45 degree angle tilt, as this model best fit out experimental data. The angle accounts for the potential offset from normal angle of incidence during the reflectance experiments, as the

PO is not entirely flat, and there may be a potential slant, although it should be noted that all simulated at different angles, including 0 degree, showed a similar extent of blue shift.

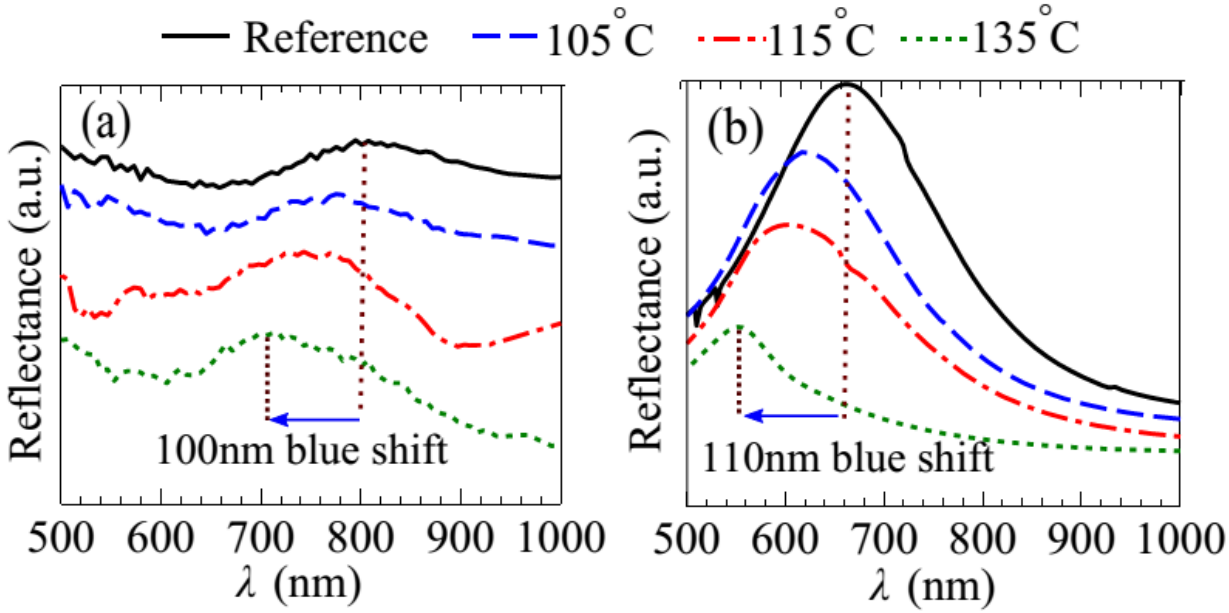

Figure 17. Calculated (left) and measured (right) reflectance spectra for nanotriangle arrays reduced in size by 0%, 35%, 52%, and 77%. Spectra are have been overlaid and are shown in arbitrary units. [97]

In order to evaluate how the resulting features and periodicity, due to annealing, affect electric field enhancements, useful for optical detection, and to validate the measured and simulated reflectance spectra, the samples were analyzed with surface enhanced Raman scattering (SERS) were conducted using a Renishaw Micro Raman system and custom built micro-Raman system with laser excitation wavelengths of 785 nm, and 633 nm, respectively. Samples were immersed in a $4x10^{-3}$M solution of benzenethiol in DI for 2 hrs., followed by a 60s MetOH and EtOH rinse, to remove excess material and leave a molecular monolayer of benzenethiol on the surface. For the 633 nm setup, a 100x .90 NA was used objective was used A laser power of .33mW was used, with integration times ranging from 1 to 60s. For the 785 nm excitation, integration time of 5 s was used, with a laser power of .5mW. Note that higher powers showed burning of the plastic substrate under

microscope, and thus were not used. The illumination spot size was 2 um in diameter, and the objective used for collection was 50X and having a 0.75 NA. A solution of neat benzenethiol was also collected at same conditions to provide a standard for enhancement calculations, where EF = $(I_{SERS}/N_{SERS})/(I_{neat}/N_{neat})$. I_{SERS}, I_{neat}, N_{SERS}, N_{neat} are the SERS and neat Raman intensities, and the number of molecules for each measurement, respectively. The SERS intensity is normalized using power P and integration time *t*, where $I_{SERS}=I_{raw}/(P.t)$. The neat Raman intensity, I_{neat} is normalized in the same way. The number of molecules measured for N_{SERS} was found by normalizing the area excited in the laser spot size by the gold coverage of the surface, where $N_{SERS}= \rho_{surf} N_A/(f_{Au} A_{spot})$. The surface coverage of benzenethiol, ρ_{surf} is reported to be .54 nmol/cm^2 , which when multiplied by Avogadro's number, N_A, and divided the spot size, A_{spot} gives the number of molecules participating in the measurement. This is then normalized by f_{Au}, the gold nanoparticle fractional coverage. To determine the number of molecules measured from the solution, $N_{neat}=\rho_{neat} V$, where ρ_{neat} is the density of benzenethiol, 9.739 mmol/cm^3 and V is the scattering volume, which can be calculated by multiplying the spot size of the laser by the collection depth, both values measured for the 785 nm setup. For the 633 nm Raman setup, a different technique for the standard was used. A 5 ul drop of neat benzenethiol was drop coated on a gold covered glass slide and allowed to dry. Over 80 Raman spectra were taken and averaged across the diameter of the spot. The number of mols Nsers was then taken as the spot size multiplied by the number of mols in 5 Ul of pure benzenethiol, divided by the area of the spot. This was done to rule out potential errors in measurement of the spot size or focal volume, as the setup was limited to a mechanical stage, constraining the ability to properly measure these quantities.

$$EF = (I_{SERS}/N_{SERS})/(I_{neat}/N_{neat})$$

I_{SERS} is the measured intensity of the 998 cm^{-1} benzenethiol peak from the samples with the Au triangles. I_{neat} is the measured Raman signal of a neat benzenethionl solution. The SERS intensity is normalized with laser power, P, and integration time, *t*, such that

$$I_{SERS} = I_{meas}/(P \times t)$$

The neat Raman intensity, I_{neat} is normalized similarly. The number of molecules measured during a Raman measurement, N_{SERS} was found by normalizing the area excited in the laser spot size by the gold coverage of the surface, calculated from SEM images, where

$$N_{SERS} = \rho_{surf}\, N_A/(f_{Au}\, A_{spot})$$

The surface coverage of benzenethiol, ρ_{surf} is the molecular packing density on the gold surface, which is reported to be .54 nmol/cm^2, which when multiplied by Avogadro's number, N_A, and divided the spot size, A_{spot} gives the total number of molecules participating in the measurement. This is then normalized by f_{Au}, the gold nanoparticle fractional coverage. To determine the number of molecules measured from the solution,

$$N_{neat} = \rho_{neat}\, V$$

where ρ_{neat} is the concentration per unit volume of benzenethiol, 9.739 mmol/cm^3 and V is the scattering volume, which can be calculated by multiplying the spot size of the laser by the collection depth, both values measured per instrument.

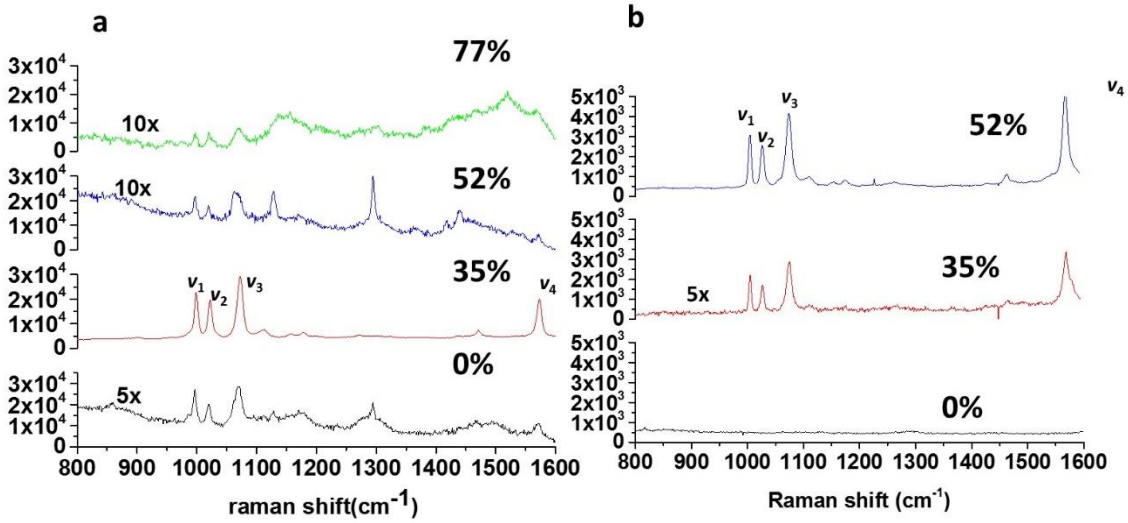

Figure 18. A) SERS spectra of a monolayer of benzenethiol on gold nanotriangle arrays reduced in size by 0%, 35%, 52%, and 77%, for excitation wavelengths of 785. B) SERS spectra at 633 excitation wavelengths for35% and 52% reduced triangle arrays. [97]

Fig. 3.16.shows SERS spectra at 785 nm and 633 nm laser excitation. As shown left in Fig.3.16, the intensity of the SERS benzenethiol peaks, at 785 nm excitation, first increases with sample size reduction of 35% by about a factor of ten when compared to the unannealed sample. The SERS intensity for samples with larger size reductions then decreases, with negligible SERS signal observed for the sample reduced by 77%. In the case of 633 nm excitation, negligible SERS signal was observed for the unannealed sample, even when integrating for 30s, while the 35% and 52% shrunk samples both showed measureable signal from 1 to 60s in Fig. 36. The SERS spectra, taken at a60 second integration time, of the 52% reduced array show an approximate tenfold increase in SERS signal when compared to 35 % reduced array. The 77% reduced array has not yet been measured was not measured on the 633 setup. Although focusing of the substrate was

achieved using the Renishaw setup, the objectives from the custom 633 nm setup was unable to focus on the sample, which may be due to the roughness of the wrinkled substrate.

In order to make quantitative comparisons, enhancement factors (EF) were calculated for all the SERS data, using the SERS intensity of the 998 cm^{-1} peak, which represents the C-H out of plane bending vibration mode. Table 3.3 lists the calculated EFs for the Au nanotriangle arrays as a function of size reduction and laser excitation. There is a red shift in the Stokes Raman signal as the molecular vibration absorbs energy during the inelastic scattering event. Thus from this value one can determine the wavelength of the scattered light, simply calculated from the following equation:

$$\Delta w = \frac{1}{l_{excitation}} - \frac{1}{l_{scattered}} \qquad (4)$$

The calculated scattered wavelengths from the 998 cm^{-1} vibrational mode are 852 nm and 676 nm for 785nm and 633 nm excitations, respectively. The table also lists the measured value of λ_{max} from the reflectance spectra of each sample as this is associated with the plasmon resonance of the Au nanotriangles. As shown in Table 3.3, at the 785 nm excitation, the EF increases for the sample heat treated at 105°C reaching a maximum of approximately 1.4×10^{7}, and then decreases for samples processed at higher temperature. The data in Table 2 shows the maximum SERS signal is measured when excited/scattered light is near the plasmon resonance as determined from reflectance data. It is also well known that SERS enhancement factors increase as tip to tip spacing of Au bowties decreases. Upon comparison of the SERS data for the sample heated to 105 °C and the reference sample, the calculated SERS enhancement at 785 nm excitation are 14.0×10^{7} and 2.2×10^{6},

respectively. The plasmon resonance for the sample processed at 105°C is approximately 770 nm and that of the reference sample is 820 nm. The scattered light from the 998 cm^{-1} vibration is 852 nm which puts the resonance of the reference sample in between excitation and scattering peaks. This suggests that the reference sample should have the highest EF, yet, as shown in table 2, the SERS EF for the sample processed at 105° C is almost an order of magnitude higher. This difference can be explained by considering the difference in tip to tip spacing between both samples. The sample heated to 105°C has considerably smaller tip to tip distances, resulting in a stronger local electric field in these regions, in addition to a higher density of bowtie structure. Plasmon resonance of the bowties treated at 105° C is still close enough to the scattering wavelength, especially considering the broadness of the peaks, and close to the excitation wavelength to see a significant SERS effect. At the 633 nm excitation, no EF was calculated for the reference sample due to low signal to noise. This is expected, as the Plasmon resonance is entirely out of range of the excitation wavelength of 633 nm and the predicted scattering wavelength of 670 nm. The samples processed at 105°C and 115°C showed EFs of 9.1×10^{6} and 8.3×10^{7}, respectively. The increase in EF fits with the measured reflectance data, considering the plasmon resonance shifts from 770 nm to 730nm when going from the 105°C to 115°C processed samples, where the ideal resonance for the 633 nm excitation would be between 630 nm and 670 nm. Although the maxima of the plasmon resonance peak for the bowties processed at 115°C still lie outside this excitation and expected scattering range, there is still some overlap as shown in figure 35.Since this sample is reduced macroscopically by 55%, there is further increase in bowtie density, plasmon interaction, and triangle size reduction, suggesting a stronger electric field. Thus, the similar EF between the sample processed at 115°C excited at 633 nm, and the sample processed at 105° C, excited at 785 nm, fits with expectations. The measured enhancement factors verify the shifted plasmon resonance

predicted by the reflectance spectra, and also show unambiguously the tunability of the nanotriangle arrays. Simply put, the same bowtie array can have its highest attainable, SERS EF, in the case here on the order of 10^7 from one laser excitation to another, which is modifiable by a quick, robust heating process. This shows the capability of the PO film to be used for tunability of the plasmon resonance. SERS enhancements factors are not reported for the sample processed at 135° C for the 633 nm excitation. This is due to the macroscopic roughness of this particularly sample, which has reduced 95% in surface area, and the inability of the objective available for that setup to focus on the sample. Both SEM and Reflectance measurements demonstrating intact areas within the actual sample, and therefore it is believed that the SERS enhancement, if measured at the 633 excitement, would show the strongest enhancement factors, due to the increased hot spot density, decreased bowtie spacing and size, and it being closer to the resonance.

ocessing mperature	mple Size duction (%)	PR(nm)	exc (nm)	,998 cm^{-1}	exc (nm)	,998 cm^{-1}
25 °C	0%	810	785	$2.2x10^6$	633	
105 °C	35%	770	785	$1.4Ex10^7$	633	$9.1x10^6$
115 °C	52%	720	785	$1.2x10^6$	633	$8.3x10^7$
135 °C	77%	710	785	$6.80x10^5$	633	

Table 3.3. Enhancement factors and plasmon resonances are shown for each of the four samples at 785 nm and 633 nm excitations. The calculated scattering wavelengths for the 785nm and 633 nm excitations at the 998 cm^{-1} were found to be 852 nm and 676 nm.[97]

3.43 Summary

Nanotriangles have been fabricated using self-assembly onto a polyolefin thermoplastic film. By heating the plastic PO substrate, the average tip to tip spacing of the gold nanotriangle array has reduced up to 77% and the average base length of the triangles has reduced up to about 33%. The exact extent of this reduction can be controlled by heat temperature. The reduction in geometry and periodicity has shown to blue shift the plasmon resonance, with a tunable window of around 100 nm. SERS spectra for each reduced sample has correlated with the reported plasmon resonances, where the highest calculated EF was ~$8x10^7$. Perhaps most interesting was the increase in maximum EF as a function of heat, suggesting stronger hot spots as a result of reducing the bowtie array size on the PO film. Furthermore, the fully shrunk sample showed localized regions with inter tip distances approaching 1 nm, which may be suitable for even stronger hot spots. By incorporating a thermo plastic substrate with self-assembly, structures can be easily modified in terms of structure and optical properties, in addition to potential enhancements in electronic field strength. While studies so far have focused on nanotriangle arrays on PO produced from 500 nm PS microspheres, we have also produced triangles from 250 nm PS microspheres, yielding arrays with much smaller inter tip spacing and triangle feature sizes. In addition to measuring the 633 nm excitation of our current 77% reduced triangle array, the next logical step is to repeat reflectance and SERS experiments for these smaller arrays, which are predicted to have stronger hot spots due to their closer tip to tip distances.

3.5 Advanced structures using polyolefin film

Using nanosphere lithography, the proof of concept of using thermos plastic films to reduce the size of nanostructure arrays has been demonstrated. The next step is to test the capabilities of the thermoplastic with more complex nanopatterns, such as from EBL. Combination between EBL and other top down lithography methods with a scalable substrate have at least two potential

implications. First, complex designs involving small, precise spacings and feature sizes may be better attained. One issue with current EBL systems is its limitation to resolve below ~30 nm, with the exception of only the state of the art systems. Also, EBL fabrication often proves inconsistent in what features are practically attainable. High dosages or poor development can lead to bleeding of the features. By adding a shrinkable element to the substrate, larger, easier patterns can be used. The second aspect of combining heat shrink polymer with EBL is the idea of size dependent studies, particularly with gap dependent studies. For example, an array of dimers with a specific start gap, could be continuously reduced via a slow heating, and probed optically. This would be significant compared to previous plasmon coupling experiments that use only a few samples of different spacings, and are hard to resolve via TEM and EELS. Here, we explore the first motive, although the ability to successfully combine EBL with heat shrinkable substrates would allow for potentially exploring the latter in the future.

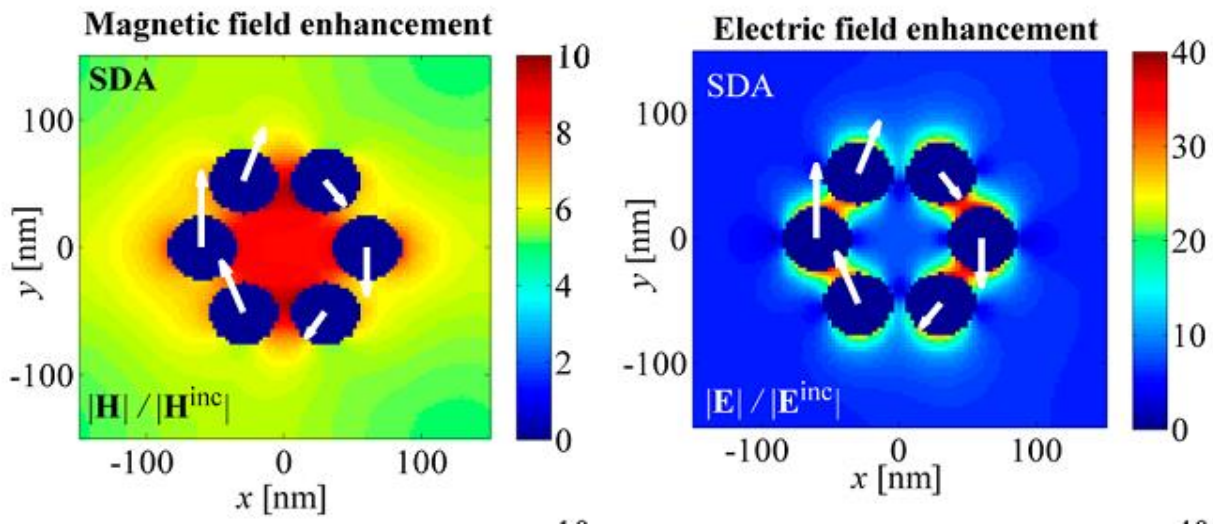

Figure 3.17. Calculated magnetic (left) and electric (right) field enhancements for CNC made of 50 nm silver spheres with 10 nm spacing on top of a SiO2 layer. White arrows denote the dipole moment direction. Reprinted with permission from (S. Campione, C. Guclu, R. Ragan, and F. Capolino, "Enhanced Magnetic and Electric Fields via Fano Resonances in Metasurfaces of Circular Clusters of Plasmonic Nanoparticles," ACS Photonics, vol. 1, no. 3, pp. 254–260, Feb. 2014). Copyright (2014) American Chemical Society

Fig 3.17 shows a magnetic loop structure, also known as a circular nanocluster (CNC) which is comprised of six plasmonic nanospheres, which are predicted to support magnetic fano resonances. Campione et al calculated both magnetic and electric field enhancements, particularly for the periodic array case (periodicity = 300 in both axes), also known as a metasurface. [100]. In this case, the magnetic field enhancement calculated is about 10 and the electric field enhancement, concentrated in the CNC gaps, is about 40. The sharp fano resonance shown in fig 38 b, and high electric field enhancement, make this structure a potential for SERS sensor. Calculations for this structure were based on the sphere area of 50 nm diameter in a loop, with each sphere 60 degrees to each other. It is predicted that different metal materials, such as gold, and different shapes, such as disks, should yield similar results. As of yet, these structures have not been measured experimentally. Here, we use the PO film to create arrays of these loops, by writing on patterns of

spheres with bigger initial size features than can then be reduced using the heating component of the film.

3.51 Electron beam lithography

50 nm Au and 4 nm Cr were deposited onto a clean polyolefin thermoplastic film, using e-beam evaporation. Ma-N 2401(Microchem) was then spun coat onto the substrate at 5000 rpm for 60s, to produce a 100 nm thick layer of negative EBL/photoresist on top the substrate, followed by a 60s prebake at 90 C, using a hot plate. The desired pattern was then written onto the photo resist using an FEI Magellan 400 XHR SEM and NPGS software, with a dosage of 356 uC/cm^2. The sample was then developed in MA-D 525 (Microchem) for 60s, followed by 3 minute rinsing in DI. The unmasked gold was etched using a gold etchant solution of 1:4:40 I2/KI/H2O for 20 seconds, followed by an IPA rinse. The 4nm of Cr was removed using Cr etchant solution for 8s, followed by an IPA rinse. Finally, the sample was sonicated in mr- Rem 660 remover (Microchem) for 30 minutes in an ice bath to remove resist.

3.52 Reduction of magnetic loop structures made from E-beam lithography

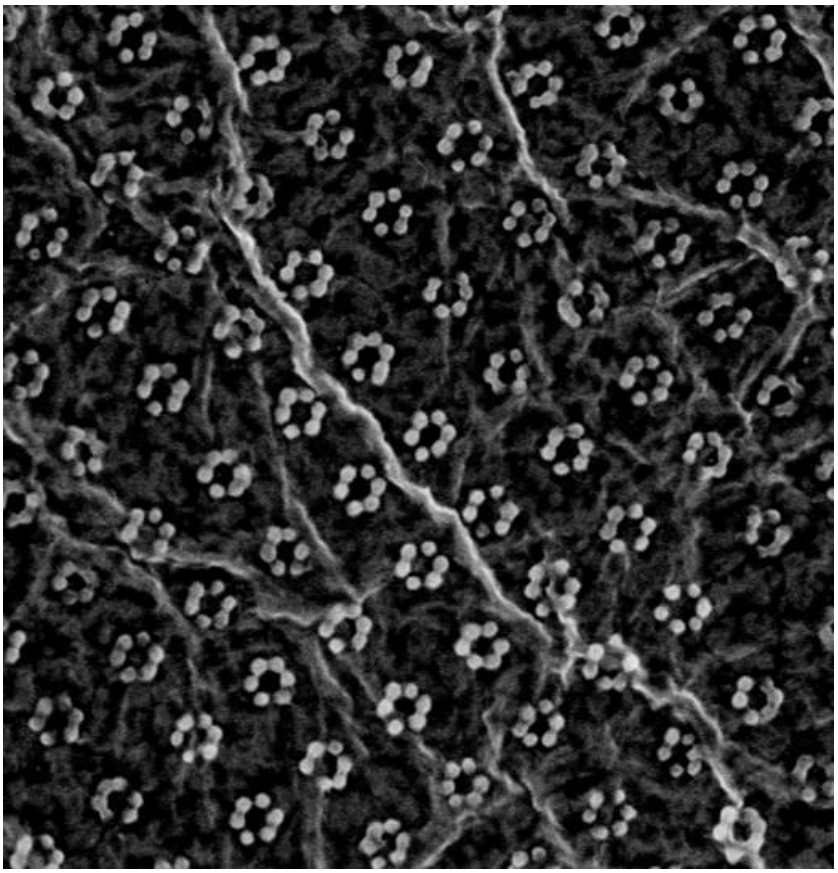

Figure 3.18. SEM of gold CNCN arrays on polyolefin shrink film.

Figure 3.18 shows SEM images of a Au CNC array on polyolefin shrink film. The film has a layer of 4 nm Cr, which was not removed for ease of imaging the substrate. As shown, the feature sizes attainable were approximately 50 nm with 30 nm spacing. When shrunk, the spacing will go down to about 10-15 nm, which is the desirable distance.

In summary, the polyolefin thermoplastic film is compatible with electron beam lithography, and therefore more advanced structure can be produced with finer feature sizes.

4. Future Experiments

This thesis discusses namely two different technologies applicable to enhance nanofabrication. In chapter 2, we looked at a bottom up fabrication assembly to cheaply and efficiently create an assembly of hotspots using gold nanoclusters with gap spacings on the sub nanometer scale. In chapter 3, we looked at a scaling technique to miniaturize nanopatterns made both from bottom up and top down fabrication. This has been shown to tune the plasmon resonance and lead to increased strength in the field. In this chapter, future experiments for both these techniques.

4.1 Point of care diagnostics

Commercial SERS sensors must have. 1) High enhancement factors. 2) High coverage and reproducibility of high enhancement factors over a large area) and 3) Low cost. Our current nanocluster arrays have a maximum SERS EF of ~$4x10^8$ at 633 nm excitation. SERS EF of ~10^8 were found consistently in an area of about 4x4mm, which was consistent with coverage analysis from SEM. Coverage can be increased by using an applied AC field[], and by varying the voltages of the DC field currently used in electrophoresis. The PS-b-PMMA template used can be applied to roll to roll processing, making our system applicable on large scale processing. This system avoids expensive lithographic processing, and, if solvent annealing is used, avoids high temperature processes. The cost analysis for a sensor, using a cheap substrate like glass, shown in table 4.1 , is estimated to be $29.00 for a 10cm x 10cm, where an average sensor is about 1cmx 1xm, which makes the cost of our potential sensor on the scale of $dollars. This is realistic for a potential disposable sensor.

Iaterial/ Method	ompany	/100 cm^2	/ cm^2 or $/g
S-b-PMMA	olymer source	40	360.00
g coated mylar	ielsen enterprises	1.00	0.21
olloidal Au anoparticles	igma Aldrich	55	255/ 100 mL
otal		**3.95**	

Table 4.1. Estimate of cost to fabricate sensors over 10 cm x 10 cm area.

A potential model for a point of care diagnostic tool was demonstrated by Wu et al., which integrated a SERS substrate into a flow cell[72]. This allowed fast identification, detection, and kinetic monitoring of drugs flowing through plastic tubing, meant to replicate an intravenous (IV) drug delivery system. It has been reported that 61% of all life threatening errors during hospitalization are associated with IV drug delivery, either due to incorrect dosage, type of drug, or incompatible codelivery multiple drugs. “Smart pumps” are used to calculate proper dose and delivery rates, but do not monitor the actual drug delivery that is in the transmission system, thus a SERS IV sensor would help add an extra layer of protection. IV transmission is an excellent sample of where SERS excels as a diagnostic technique. It is noninvasive, does not require labeling agents, and does not suffer from interference of large water absorption peaks, as water is used in IV systems for drug delivery. The SERS substrate used was a plasmonic nanodome array, consisting of an array of ~300 nm gold domes with 10 -20nm gaps. The measured SERS EF for a 785 nm laser excitation was found to be 8.51×10^7. Using the SERS substrate in a follow cell, and exciting the system with a 785 nm laser, they were able to successfully detect low concentrations of many analytes, in addition to determining more than one drug compound at once. Using dopamine

solutions of different concentrations ,which are delivered through an IV plastic tube and analyzed in a flow cell integrated with the SERS sensor, their detection limits are about 12 ug/mL, or 12 parts per million (PMM). This is achieved with a SERS EF of 8.51 x 10 7 and surface density of about 6.25 x 106 mm-2 hot spots. Our detection limits are currently at 200 ppb, almost a factor of 100 better, for norepinephrine, which is similar in structure. By improving our coverage and optimizing our gap spacing, shown in the next section, this detection limit can be lowered even further.

IV drug delivery sensors are just one potential example of the role that SERS can serve in point of care. Breathalyzers have been demonstrated to detect biomarkers, in real time, on the parts per billion (ppb) scale. These biomarkers can be used to detect the onset of diseases, such as tuberculosis. SERS point of care detectors have also been suggested for use in detecting explosives and pollutants at factory sites.

4.2 Exploring the gap

Quantum nonlocal effects have been observed even in metallic nanoparticles as large as 10 nm.[101]. Computational work by Ciraci [102], using a hydrodynamic model, calculated the extinction efficiency spectra for spherical, cone, and disk dimers (closely spaced particles) at 2, 1 and .5 nm gaps, using both local and non-local effects. In all cases, the LSPR was shown to exhibit larger blue-shifts when non-locality was included, consistent with experiment. This work also suggested that at the smallest gaps (<1 nm) that charge smearing across the disk surface should be observed, consistent with a tunneling based description. Additional computational efforts [103] have also suggested a saturation of the confined optical fields between sub nanometer nanoparticle gaps, with this also potentially derived from tunneling effects. As discussed in chapter 2, the mixing of two dipolar modes should lead to a stronger hybridized bonding mode within the gap of two nanoparticles, where the mode would red shift and increase in intensity as the gap decreases.

Classically, this description would only be expected to fail when the nanoparticles merged, creating a conductive bridge between the two and resulting in a charge transfer plasmon mode (CTP). Essentially, the plasmon mode of the two particles would begin to resemble that of an oblong single nanoparticle. Both DFT calculations, and EELS, show significantly different results from classical expectations, as demonstrated in figure 4.1. Figure 4.1 a) shows EELS is used in tandem with scanning TEM. The red lines at ~ 2.5 eV and 3.5 eV correspond to the lowest order and 2nd order bonding modes, respectively [104]. TEM images, taken after each measurement, show clearly the existence of the dimer gap after the disappearance of the bonding dipolar mode from EELS spectra, which is contrary to classical expectations. The CTP mode, which appears in merged metal dimers, where electrons can flow freely, has been reported to appear even at non-merged dimers [105], resulting in a smooth, as opposed to the predicted abrupt, and transition. Density functional calculations, shown in b) verify these observations. Quantum models have predicted the appearance of the CTP mode to occur through the tunneling of conductive electrons across the small air-gap (<.5nm) between the nanoparticles, effectively cutting short the hybridized dipolar mode and resulting in blue shifted, weaker, CTP modes.

As discussed in chapter 2, it is believed that our current interparticle spacings in our nanocluster assemblies, which are ~ .6 nm, are experiencing quenching of the field when being excited for SERS. While sub nanometer plasmonic coupling has been studied to some extent in dimers, little experimentation has been done on other metal particle geometries, such as trimers and linear chains. Clusters assemblies have already been fabricated onto TEM grids and analyzed via TEM. The next step is to use EELS spectroscopy as described above to explore potential quantum effects. In terms of optimizing hot spot signal for SERS, the optimum nanoparticle gap spacing must be found or our system. This can be done by using difficult thiotic acid ligands of varying chain lengths, to modify

the spacing of nanoparticles. A number of cluster assemblies onto TEM grids, with average gap spacings ranging from several nm down to half a nm, can be fabricated and measured using EELS and SERS to determine the optimum length. An additional avenue, using solvent annealing, would be to make the nanoparticle assembly onto a polyolefin film, and using the shrinking properties discussed in chapter 3 to tune the gap spacing. In this case, electrophoresis would not be needed, as a 2-4 nm gap could be brought close to the quantum regime. Reducing the cluster assemblies on polyolefin films and then measuring the enhancement factor would allow for quick optimization of our plasmonic nanocluster gaps.

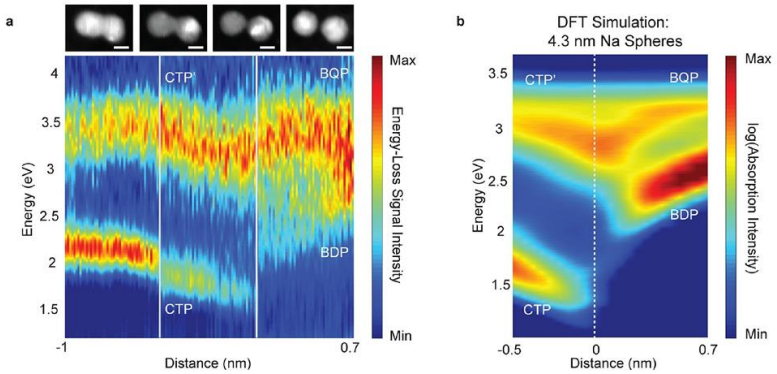

Figure 4.1. STEM and EELS spectra of silver dimer at decreasing gaps. DFT simulation of plasmonic response for Na spheres of decreasing gap. Negative gap values correspond to merged particles [104]. Reprinted with permission from (103. J. A. Scholl, A. García-Etxarri, A. L. Koh, and J. A. Dionne, "Observation of Quantum Tunneling between Two Plasmonic Nanoparticles," Nano Lett., vol. 13, no. 2, pp. 564–569, Feb. 2013.) Copyright (2013) American Chemical Society.

4.3 Integrating waveguides to Excite Nanocluster Assemblies

Shown in figure 4.2 is a silicon nitride waveguide made with PS-b-PMMA film and nanoparticle cluster assembly on top. Recent simulations predict a high enhancement of electric field compared to the waveguides modal field at the same location with the nanoparticle dimer antennas, making it a potential structure to be integrated into a SERS system, as an alternative to using a microscope setup. Since silicon nitride is not conductive, the diffusion method was used to deposit these nanoparticles, thus the predicted enhancements are not as high as would be with the EPD case, which produces gaps on the order of ~ 1 nm. In the future, finding ways to use electrophoresis on nonconductive substrates, such as using an AC voltage supply instead of DC voltage supply, will lead to creating more advanced structures with strong electromagnetic field enhancements.

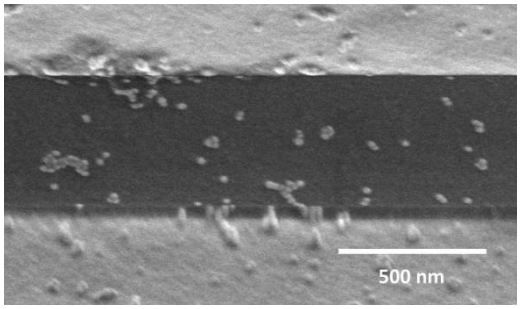

Figure 4.2. SEM of SiN waveguide with a PS-b-PMMA film on top of it and nanoparticle cluster assemblies with Au nanoparticles 20 nm in diamter.

4.4 Controllable bow tie arrays for SERS

The bow tie array structure discussed in Chapter 3 has been shown to increase in EF up to high 10^7. This is for the gold bowtie structure, after being reduced in size. In silver, it has been shown for bowties of similar starting size, that attainable EFs are as high as mid 10^7. The process described in chapter 3 can be easily modified for silver. Additionally, work on using smaller nanospheres as a deposition mask has already been explored/ Using 250 nm has shown to create triangles with base length~66% smaller than the ones described in ch 2, or ~30 nm, and tip to tip spacings about 50% smaller than those in ch2, or ~45 nm, as shown in figure 4.3. Note, that both spacing and triangle size can be altered based on the etch time of the latex mask, where there is an inherent tradeoff between the two. Both decrease in triangle size and distance should lead to a higher confined fields, the former from the lightning rod effect and the latter from plasmonic coupling. Given the higher reduction rate in the nonmetal areas of the PO film, finding the right starting parameters, in the interest of optimizing hot spot field strength, could be explored. . Using smaller triangles of silver on the PO film, and reducing the array by ~50, could potentially lead to EF as high as 10^9, given the

estimated size of the final silver triangle array. This could be done cheaply and effectively, and be implemented in cheap SERS and MEF sensors.

4.5 Reduction of wrinkling of substrate

The greatest hurdle of implementing the heat shrink film into other nanofabrication experiments is the wrinkling of the film. As shown in CH 3, significant wrinkling begins to occur after reducing the film in macroscopic length by about 50%, or when heating up to a temperature of about ~ 115°C. This was the case for the bow tie arrays. For the nanopillars, significant wrinkling started after a reduction of about 30%. While the buckling of the PO film itself is predicted to wrinkle to some extent, it has been shown from AFM that additional films, including oxide layers, result in significantly more wrinkling. Therefore, to reduce wrinkling of the film and to allow for greater reductions, finding ways to minimize what is on top of the PO film should reduce wrinkling. Transferring the reduced pattern from the PO is one way to circumvent wrinkling. One potential medium is a PDMS mold [73]. Ideally, patterns could be reduced on the PO film, transferred to another medium, and then transferred back to an unshrunk film, allowing for further reduction.

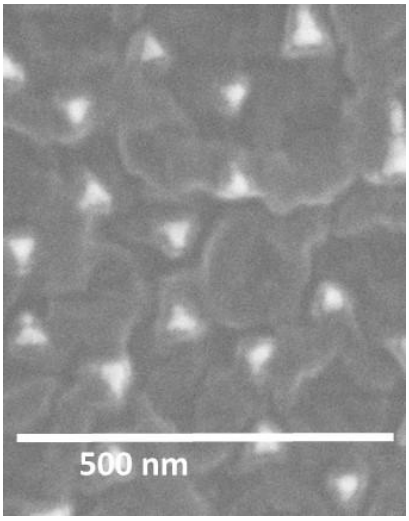

Figure 4.3. SEM of gold nanotriangles on top of a PO film, fabricated from latex spheres of 250 nm.

4.6 Using EBL with the polyolefin film

Circular nano cluster (CNC) arrays have been successfully fabricated onto a polyolefin thin film using EBL, and have been reduced by ~ to achieve ~ nm spacing. The optical of these properties can next be measured, either using a fiber optic or using magnetic force microscopy. In the latter case, a magnetic dye may be deposited onto the surface. It is expected that the magnetic force will increase when scanned over the loops.

Beyond measuring the structures is the actual ability to use EBL to attain other previously unattainable structures with closer spacings. Another potential avenue of exploration is to use experiments with plasmon coupling at small scale spacings, as mentioned in section 4.2 since the quantum regime is larger for larger structures, larger dimeric structures can be made, with spacings ranging from below 10 nm. By introducing heat slowly, many different gap spacings can be generated. While the PO film would not be compatible with EELS, UV-vis spectroscopy has also been shown to measure the effects of quantum interference in plasmonic coupling []. Such a system could be used here as well, considering the transparency of the film in that range.

Bibliography

1. P. Ginzburg and M. Orenstein, "Plasmonic transmission lines: from micro to nano scale with impedance matching," Opt. Express 15, 6762-6767 (2007).

2. R. K. Vinnakota and D. A. Genov, “Terahertz Optoelectronics with Surface Plasmon Polariton Diode,” Sci Rep, vol. 4, May 2014.

3. H. J. Queisser, Photovoltaic conversion at reduced dimensions, Physica E: Low

4. G. P. Agrawal, Fiber-optic communication systems, Wiley, New York, 2002.

5. D. A. B. Miller, Device requirements for optical interconnects to silicon chips, Proc. IEEE 97, 1166 (2009).

6. E. Ozbay, Plasmonics: Merging photonics and electronics at nanoscale dimensions, Science 311, 189 (2006).

7. K. A. Willets and R. P. Van Duyne, Localized surface plasmon resonance spectroscopy and sensing, Annu. Rev. Phys. Chem. 58, 267 (2007).

8. F. T. Chang, R., Surface enhanced Raman scattering, Plenum, New York, 1981

9. K. Aslan, I. Gryczynski, J. Malicka, E. Matveeva, J. R. Lakowicz, and C. D. Geddes, "Metal-enhanced fluorescence: an emerging tool in biotechnology," Curr. Opin. Biotechnol., vol. 16, no. 1, pp. 55–62, Feb. 2005.

10. S. Nie and S. R. Emory, "Probing Single Molecules and Single Nanoparticles by Surface-Enhanced Raman Scattering," Science, vol. 275, no. 5303, pp. 1102–1106, Feb. 1997.

11. Allhoff, Fritz; Lin, Patrick; Moore, Daniel (2010). "What is nanotechnology and why does it matter?": from science to ethics. John Wiley and Sons. pp. 3–5. ISBN 1-4051-7545-1.

12. T. Konishi, M. Kiguchi, M. Takase, F. Nagasawa, H. Nabika, K. Ikeda, K. Uosaki, K. Ueno, H. Misawa, and K. Murakoshi, "Single Molecule Dynamics at a Mechanically Controllable Break Junction in Solution at Room Temperature," J. Am. Chem. Soc., vol. 135, no. 3, pp. 1009–1014, Jan. 2013.

13. R. Esteban, A. G. Borisov, P. Nordlander, and J. Aizpurua, "Bridging quantum and classical plasmonics with a quantum-corrected model," Nat. Commun., vol. 3, p. 825, May 2012.

14. D. R. Smith, J. B. Pendry, and M. C. K. Wiltshire, "Metamaterials and Negative Refractive Index," Science, vol. 305, no. 5685, pp. 788–792, Aug. 2004.

15. A. Boltasseva, H. Atwater. "Low-Loss Plasmonic Metamaterials" Science 21 January 2011: 331 (6015), 290-29[1]1. [DOI:10.1126/science.1198258]

16. W. L. Barnes, A. Dereux, and T. W. Ebbesen, Surface plasmon subwavelength optics, Nature 424, 824 (2003).

17. S. Kawata, Y. Inouye, and P. Verma, "Plasmonics for near-field nano-imaging and superlensing," Nat Photon, vol. 3, no. 7, pp. 388–394, Jul. 2009.

18. Smolyaninov, I. I., Davis, C. C., Elliott, J. & Zayats, A. V. Resolution enhancement of a surface immersion microscope near the plasmon resonance. Opt. Lett. 30,382–384 (2005)

19. Bozhevolnyi, S. I., Vohnsen, B., Smolyaninov, I. I. & Zayats, A. V. Direct observation of surface polariton localization caused by surface roughness. Opt. Commun. 117,417–423 (1995)

20. J. Barthes, A. Bouhelier, A. Dereux, and G. C. des Francs, "Coupling of a dipolar emitter into one-dimensional surface plasmon," Sci Rep, vol. 3, Sep. 2013.

21. H. Raether, Surface plasmons on smooth and rough surfaces and on gratings, SpringerVerlag, Berlin Heidelberg, 1988.

22. M. Li, S. K. Cushing, and N. Wu, "Plasmon-enhanced optical sensors: a review," Analyst, vol. 140, no. 2, pp. 386–406, 2015.

23. Y. Li, K. Zhao, H. Sobhani, K. Bao and P. Nordlander,J. Phys. Chem. Lett., 2013, 4, 1352–1357.

24. J. R. Lackowicz,Plasmonics, 2006, 1,5–33.

25. 14 J. Dostalek and W. Knoll,Biointerphases, 2008, 3,12–22.

26. K. A. Willets and R. P. Van Duyne,Annu. Rev. Phys. Chem., 2007,58, 267–297

27. M. Li, S. K. Cushing, J. Zhang, J. Lankford, Z. P. Aguilar, D. Ma and N. Wu,Nanotechnology, 2012, 23, 115501.

28. K. A. Willets and R. P. Van Duyne,Annu. Rev. Phys. Chem.,2007,58, 267–297.

29. 21 K. S. Lee and M. A. El-Sayed,J. Phys. Chem. B, 2005, 109, 20331–20338.

30. H. Wang, C. S. Levin and N. J. Halas,J. Am. Chem. Soc., 2005, 127, 14992–14993

31. P. D. Nallathamby, T. Huang and X. H. N. Xu,Nanoscale, 2010,2, 1715–1722.

32. 23 L. Tong, Q. Wei, A. Wei and J. X. Cheng, Photochem. Photobiol., 2009, 85,21–32

33. J. M. Slocik, J. S. Zabinski, D. M. Phillips and R. R. Naik, Small, 2008, 4, 548–551.

34. 62 J. Zhang, L. Wang, D. Pan, S. Song, F. Y. Boey, H. Zhang an C. Fan,Small, 2008, 4, 1196–1200

35. A. Kinkhabwala, Z. Yu, S. Fan, Y. Avlasevich, K. M¨ ullen and W. E. Moerner,Nat. Photonics, 2009, 3, 654–657.

36. E. Papadopoulou and S. E. Bell,Angew. Chem., Int. Ed., 2011,50, 9058–9061.

37. C. Otto, T. J. J. Van den Tweel, F. F. M. De Mul and J. Greve, J. Raman Spectrosc., 1986, 17, 289–298.

38. I. Al-Ogaidi, H. Gou, A. K. Al-kazaz, Z. Aguilar, A. K. Melconian, P. Zheng and N. Q. Wu,Anal. Chim. Acta, 2014, 811,76–80.

39. L. Qin, S. Park and C. A. Mirkin,Science, 2005,309, 113–115

40. A. B. Zrimsek, A.-I. Henry, and R. P. Van Duyne, "Single Molecule Surface-Enhanced Raman Spectroscopy without Nanogaps," J. Phys. Chem. Lett., vol. 4, no. 19, pp. 3206–3210, Oct. 2013

41. M. Li, S. K. Cushing, H. Liang, S. Suri, D. Ma and N. Wu, Anal. Chem., 2013, 85, 2072–2078

42. E. C. Le Ru, E. Blackie, M. Meyer and P. G. Etchegoin,J. Phys. Chem. C, 2007, 111, 13794–13803.

43. J. Chen, B. Shen, G. Qin, X. Hu, L. Qian, Z. Wang, S. Li, Y. Ren and L. Zuo,J. Phys. Chem. C, 2012, 116, 3320–3328.

44. S. Y. Lee, L. Hung, G. S. Lang, J. E. Cornett, I. D. Mayergoyz and O. Rabin,ACS Nano, 2010, 4, 5763–5772.

45. F. S. Ameer, W. Hu, S. M. Ansa, K. Siriwardana, W. E. Collier, S. Zou and D. Zhang,J. Phys. Chem. C, 2013, 117, 3483–3488

46. Smith, David R. (2006-06-10). "What are Electromagnetic Metamaterials?". Novel Electromagnetic Materials. The research group of D.R. Smith. Retrieved 2009-08-19.

47. Shelby, R. A.; Smith, D. R.; Schultz, S. (2001). "Experimental Verification of a Negative Index of Refraction". Science 292 (5514): 77–79.

48. A. Vora, J. Gwamuri, N. Pala, A. Kulkarni, J.M. Pearce, and D. Ö. Güney, "Exchanging ohmic losses in metamaterial absorbers with useful optical absorption for photovoltaics," Sci. Rep. 4, 4901 (2014). doi:10.1038/srep04901 arxiv preprint

49. "First Demonstration of a Working Invisibility Cloak". Office of News & Communications Duke University. Retrieved 2009-05-05.

50. Engheta, Nader; Richard W. Ziolkowski (June 2006). Metamaterials: Physics and Engineering Explorations. Wiley & Sons. pp. xv, 3-30, 37, 143-150, 215-234, 240-256. ISBN 978-0-471-76102-0.

51. C. Vieu, F. Carcenac, A. Pépin, Y. Chen, M. Mejias, A. Lebib, L. Manin-Ferlazzo, L. Couraud, and H. Launois, “Electron beam lithography: resolution limits and applications,” Appl. Surf. Sci., vol. 164, no. 1–4, pp. 111–117, Sep. 2000.

52. V. R. Manfrinato, L. Zhang, D. Su, H. Duan, R. G. Hobbs, E. A. Stach, and K. K. Berggren, “Resolution Limits of Electron-Beam Lithography toward the Atomic Scale,” Nano Lett., vol. 13, no. 4, pp. 1555–1558, Apr. 2013.

53. S. Y. Chou, “Nanoimprint lithography,” J. Vac. Sci. Technol. B Microelectron. Nanometer Struct., vol. 14, no. 6, p. 4129, Nov. 1996.

54. C. L. Haynes and R. P. Van Duyne, “Nanosphere Lithography: A Versatile Nanofabrication Tool for Studies of Size-Dependent Nanoparticle Optics,” J. Phys. Chem. B, vol. 105, no. 24, pp. 5599–5611, Jun. 2001.

55. A. N. Marchi, I. Saaem, B. N. Vogen, S. Brown, and T. H. LaBean, “Toward Larger DNA Origami,” Nano Lett., vol. 14, no. 10, pp. 5740–5747, Oct. 2014.

56. J. Zuloaga, E. Prodan, and P. Nordlander, “Quantum Description of the Plasmon Resonances of a Nanoparticle Dimer,” Nano Lett., vol. 9, no. 2, pp. 887–891, Feb. 2009.

57. Zsigmondy, R.Justus Liebigs Ann. Chem.1898, 301,29–54.

58. Faraday, M.Philos. Trans. R. Soc. London1857, 147, 145–181

59. Reinhard, B. M.; Siu, M.; Agarwal, H.; Alivisatos, A. P.Liphardt, J.Nano Lett.2005, 5, 2246–2252

60. J. M. Hoffmann, H. Janssen, D. N. Chigrin, and T. Taubner, “Enhanced infrared spectroscopy using small-gap antennas prepared with two-step evaporation nanosphere lithography,” Opt. Express, vol. 22, no. 12, p. 14425, Jun. 2014.

61. Palomba, S.; Danckwerts, M.; Novotny, L.J. Opt. A-Pure Appl. Opt.2009, 11, 114030

62. Christensen, K.; Molonev, N. R. Complexity and criticality; Imperial College Press: London, 2005.

63. Yang, L. L.; Wang, H. Y.; Yan, B.; Reinhard, B. M.J. Phys. Chem. C2010, 114, 4901–4908

64. B. Yan, S. V. Boriskina, and B. M. Reinhard, “Design and Implementation of Noble Metal Nanoparticle Cluster Arrays for Plasmon Enhanced Biosensing,” J. Phys. Chem. C, vol. 115, no. 50, pp. 24437–24453, Dec. 2011.

65. S. M. Adams, S. Campione, J. D. Caldwell, F. J. Bezares, J. C. Culbertson, F. Capolino, and R. Ragan, "Non-lithographic SERS Substrates: Tailoring Surface Chemistry for Au Nanoparticle Cluster Assembly," Small, vol. 8, no. 14, pp. 2239–2249, 2012.

66. S. M. Adams, S. Campione, F. Capolino, and R. Ragan, "Directing Cluster Formation of Au Nanoparticles from Colloidal Solution," Langmuir, vol. 29, no. 13, pp. 4242–4251, Apr. 2013.

67. D.-K. Lim, K.-S. Jeon, H. M. Kim, J.-M. Nam, and Y. D. Suh, "Nanogap-engineerable Raman-active nanodumbbells for single-molecule detection," Nat Mater, vol. 9, no. 1, pp. 60–67, 2010.

68. Hayazawa, N., Inouye, Y., Sekkat, Z. & Kawata, S. Metallized tip amplification of near-field Raman scattering. Opt. Commun. 183,333–336 (2000).

69. E. Prodan, C. Radloff, N. J. Halas, and P. Nordlander, "A Hybridization Model for the Plasmon Response of Complex Nanostructures," Science, vol. 302, no. 5644, pp. 419–422, Oct. 2003.

70. L. Polavarapu, J. Perez-Juste, Q.-H. Xu, and L. M. Liz-Marzan, "Optical sensing of biological, chemical and ionic species through aggregation of plasmonic nanoparticles," J. Mater. Chem. C, vol. 2, no. 36, pp. 7460–7476, 2014.

71. D. C. Marinica, A. K. Kazansky, P. Nordlander, J. Aizpurua, and A. G. Borisov, "Quantum Plasmonics: Nonlinear Effects in the Field Enhancement of a Plasmonic Nanoparticle Dimer," Nano Lett., vol. 12, no. 3, pp. 1333–1339, Mar. 2012.

72. H.-Y. Wu and B. T. Cunningham, "Point-of-care detection and real-time monitoring of intravenously delivered drugs via tubing with an integrated SERS sensor," Nanoscale, vol. 6, no. 10, pp. 5162–5171, 2014.

73. M. H. Lee, M. D. Huntington, W. Zhou, J.-C. Yang, and T. W. Odom, “Programmable Soft Lithography: Solvent-Assisted Nanoscale Embossing,” Nano Lett., vol. 11, no. 2, pp. 311–315, Feb. 2011.

74. D. Nguyen, D. Taylor, K. Qian, N. Norouzi, J. Rasmussen, S. Botzet, M. Lehmann, K. Halverson, and M. Khine, “Better shrinkage than Shrinky-Dinks,” Lab. Chip, vol. 10, no. 12, pp. 1623–1626, Jun. 2010.

75. H. Sharma, M. A. Digman, N. Felsinger, E. Gratton, and M. Khine, “Enhanced emission of fluorophores on shrink-induced wrinkled composite structures,” Opt. Mater. Express, vol. 4, no. 4, pp. 753–763, Apr. 2014

76. L. Zhang, X. Lang, A. Hirata, and M. Chen, “Wrinkled Nanoporous Gold Films with Ultrahigh Surface-Enhanced Raman Scattering Enhancement,” ACS Nano, vol. 5, no. 6, pp. 4407–4413, Jun. 2011

77. J. D. Caldwell, O. Glembocki, F. J. Bezares, N. D. Bassim, R. W. Rendell, M. Feygelson, M. Ukaegbu, R. Kasica, L. Shirey, and C. Hosten, “Plasmonic Nanopillar Arrays for Large-Area, High-Enhancement Surface-Enhanced Raman Scattering Sensors,” ACS Nano, vol. 5, no. 5, pp. 4046–4055, May 2011.

78. S. Ji, J. Park, and H. Lim, “Improved antireflection properties of moth eye mimicking nanopillars on transparent glass: flat antireflection and color tuning,” Nanoscale, vol. 4, no. 15, pp. 4603–4610, Jul. 2012

79. N. Sharac, H. Sharma, M. Khine, and R. Ragan, “Tunable nano bead arrays on film for controlling propogation of light,” in Plasmonics: Metallic Nanostructures and Their Optical Properties XI, San Diego, CA, 2013, vol. 8809, p. 88091O–88091O–8

80. K. Asakawa and T. Hiraoka, “Nanopatterning with Microdomains of Block Copolymers using Reactive-Ion Etching Selectivity,” Japanese Journal of Applied Physics, vol. 41, no.10, pp. 6112–6118, 2002.

81. J. S. Mijovic and J. A. Koutsky, “Etching of Polymeric Surfaces: A Review,” Polymer-Plastics Technology and Engineering, vol. 9, no. 2, pp. 139–179, 1977.

82. B. Päivänranta, H. Merbold, R. Giannini, L. Büchi, S. Gorelick, C. David, J. F. Löffler, T. Feurer, and Y. Ekinci, “High Aspect Ratio Plasmonic Nanostructures for Sensing Applications,” ACS Nano, vol. 5, no. 8, pp. 6374–6382, 2011.

83. R.H. Ritchie, “Plasma Losses by Fast Electrons,” Phys. Rev. Lett., 106, pp. 874–881,1957.

84. S. Shen, A. Narayanaswamy, and G. Chen, “Surface Phonon Polaritons Mediated Energy Transfer between Nanoscale Gaps,”Nano Letters, vol. 9, no.8, pp. 2909-2913, 2009.

85. S.S. Ng, Z. Hassan, A. Hassan, “Experimental and theoretical studies of surface phonon polariton of AlN thin film,” Appl. Phys. Lett. vol. 90, no.8, 2007.

86. S.A Holmstrom, T.H Stievater, M. W. Pruessner, D. Park D, W. S. Rabinovich, J. B. Khurgin, C. J. K. Richardson, S. Kanakaraju, L. C. Calhoun, R. Ghodssi, “Guided-mode phonon-polaritons in suspended waveguides,” Phys. Rev. B, 86, pp. 165120, 2012.

87. N. Dahan, A. Niv, G. Biener, V. Kleiner, E. Hasman, “Space-variant polarization manipulation of a thermal emission by a SiO2 subwavelength grating supporting surface phonon-polaritons,” Appl.Phys. Lett. 86, pp. 191102, 2005.

88. A. K. Hafeli, E. Rephaeli, S. H. Fan, D. G. Cahill, T. E. J. Tiwald, “Temperature dependence of surface phonon polaritons from a quartz grating,” Appl. Phys. , 110, pp. 043517,2011

89. J.D. Caldwell, O. J. Glembocki, Y. Francescato, N. Sharac, V. Giannini, F. J. Bezares, J. P. Long, J. C. Owrutsky, I. Vurgaftman, J. G. Tischler, Vi. D. Wheeler, N. D. Bassim, L. M. Shirey, R. Kasica, and S.A. Maier, "Low-Loss, Extreme Subdiffraction Photon Confinement via Silicon Carbide Localized Surface Phonon Polariton Resonators," Nano Letters, vol. 13,no.8,pp. 3690-369, 2013.

90. N. Ocelic, R. Hillenbrand, "Subwavelength-scale tailoring of surface phonon polaritons by focused ion-beam implantation," Nat. Mater., 3, pp. 606–609,2004.

91. B. Neuner III, D. Korobkin, C. Fietz, D. Carole, G. Ferro, and G. Shvets, "Critically coupled surface phonon-polariton excitation in silicon carbide," Opt. Lett. 34, pp. 2667-2669, 2009.

92. S. Zhang, K. Bao, N. J. Halas, H. Xu, and P. Nordlander, "Substrate-Induced Fano Resonances of a Plasmonic Nanocube: A Route to Increased-Sensitivity Localized Surface Plasmon Resonance Sensors Revealed," Nano Letters, vol. 11, no. 4, pp. 1657-1663,2011

93. Z. Dai, X. Xiao, L. Liao, J. Zheng, F. Mei, W. Wu, J. Ying, F. Ren, and C. Jiang, "Large-area, well-ordered, uniform-sized bowtie nanoantenna arrays for surface enhanced Raman scattering substrate with ultra-sensitive detection," Appl. Phys. Lett., vol. 103, no. 4, p. 041903, Jul. 2013

94. G. Bi, L. Wang, L. Ling, Y. Yokota, Y. Nishijima, K. Ueno, H. Misawa, and J. Qiu, "Optical properties of gold nano-bowtie structures," Opt. Commun., vol. 294, pp. 213–217, May 2013.

95. J. C. Hulteen, D. A. Treichel, M. T. Smith, M. L. Duval, T. R. Jensen, and R. P. Van Duyne, "Nanosphere Lithography: Size-Tunable Silver Nanoparticle and Surface Cluster Arrays," J. Phys. Chem. B, vol. 103, no. 19, pp. 3854–3863, May 1999

96. Herr, Kuerbanjiang, Benel, Papageorgiou, Goncalves, Boneberg, Leiderer, Ziemann, Marek, and Hahn, "Near-field effects and energy transfer in hybrid metal-oxide nanostructures" Beilstein J. Nanotechnol. 2013, 4, 306–317.

97. N. Sharac, Hi. Sharma, M. Veysi, M. Khine, F. Capolino, and R. Ragan, "Tuning the plasmon resonance of bowtie nanoantennas," Prep.

98. N. Anker, W. P. Hall, O. Lyandres, N. C. Shah, J. Zhao, and R. P. Van Duyne, "Biosensing with plasmonic nanosensors," Nat. Mater., vol. 7, no. 6, pp. 442–453, 2008

99. S. Raza, W. Yan, N. Stenger, M. Wubs, and N. A. Mortensen "Blueshift of the surface plasmon resonance in silver nanoparticles: substrate effects," Optics Express, vol. 21, no. 22, pp. 27344-27355, 2013.

100. S. Campione, C. Guclu, R. Ragan, and F. Capolino, "Enhanced Magnetic and Electric Fields via Fano Resonances in Metasurfaces of Circular Clusters of Plasmonic Nanoparticles," ACS Photonics, vol. 1, no. 3, pp. 254–260, Feb. 2014

101. S. Dai, Z et al,, Science 343, 1125 (2014).

102. C. Ciracì, Y. Urzhumov, and D.R. Smith, JOSA B, 30, 10, 2731-2736 (2013)

103. J. A. Scholl, A. García-Etxarri, A. L. Koh, and J. A. Dionne, "Observation of Quantum Tunneling between Two Plasmonic Nanoparticles," Nano Lett., vol. 13, no. 2, pp. 564–569, Feb. 2013.

104. T. Teperik, P. Nordlander, J. Aizpurua, A. Borisov, Opt. Express 21, 27306-27325 (2013).

105. S.F Tan, L. Wu, J.K.W Yang, P. Bai, M. Bosman, C.A. Nijjuis, Science, 343, 1496 (2014)